

Dust induced non-linear dynamics in C-rich AGB star envelopes

vorgelegt von

Dipl.-Phys. Claudia Dreyer
aus Hennigsdorf

Von der Fakultät II - Mathematik und Naturwissenschaften
der Technischen Universität Berlin
zur Erlangung des akademischen Grades
Doktor der Naturwissenschaften
-Dr. rer. nat.-

genehmigte Dissertation

Promotionsausschuss:

Vorsitzender: Prof. Dr. T. Brandes

Berichter: Prof. Dr. E. Sedlmayr

Berichter: Prof. Dr. H. Rauer

Tag der wissenschaftlichen Aussprache: 24. März 2010

Berlin 2010

D 83

Zusammenfassung

Langperiodische Veränderliche (LPVs) und Miras sind radial pulsierende, weit entwickelte Rote Riesensterne auf dem asymptotischen Riesenast (AGB). Ihre kühlen ausgedehnten Hüllen bieten exzellente Bedingungen für die Bildung komplexer Makromoleküle bis hin zu den ersten Festkörpern (Staub). Durch das Zusammenspiel zwischen Staubbildung und Strahlungsdruck bildet sich ein massiver Materiestrom aus, der zur Entstehung einer zirkumstellaren Staubbülle (ZSH) führt und letztendlich das interstellare Medium (ISM) mit prozessiertem Material anreichert.

Eine solche ZSH kann als nichtlineares multi-oszillierendes System betrachtet werden, dessen Eigenfrequenzen durch intrinsische Zeitskalen der verschiedenen, miteinander gekoppelten physikalischen und chemischen Prozesse kontrolliert werden. Die vorliegende Arbeit untersucht speziell das komplexe Verhalten kohlenstoffreicher ZSHs. Basierend auf der numerischen Lösung des zugrunde liegenden Systems gekoppelter nichtlinearer partieller Differentialgleichungen werden Analyseverfahren wie die Fouriertransformation, Poincaré Schnitte und stroboskopische Karten zur Untersuchung der Hüllendynamik angewendet.

Es wird gezeigt, daß ZSHs um extrem leuchtkräftige AGBs dazu neigen dynamisch instabil zu werden. Ohne jegliche zusätzliche Zufuhr von mechanischem Impuls oder Energie durch einen pulsierenden Zentralstern entwickelt sich eine selbsterhaltende oszillierende Struktur durch den sogenannten äußeren κ -Mechanismus. Solche Hüllen besitzen eine offensichtliche Eigenfrequenz.

Für die ZSHs um leuchtärmere AGBs kann solch eine Eigenfrequenz nicht unmittelbar bestimmt werden, da eine Hülle oder Materieströme mit sich selbsterhaltenden Strukturen nicht ohne zusätzlichen äußeren Energieeintrag ausgebildet werden. Diese Energiezufuhr wird in der vorliegenden Arbeit als irregulär (Weißes Rauschen) angenommen, so wie sie z.B. durch Konvektion in den äußeren Atmosphären roter Riesensterne entstehen kann.

Desweiteren wird gezeigt, daß die Wechselwirkung der Hüllenmoden mit einer äußeren periodischen Anregung wegen des nicht linearen Verhaltens der Hülle zu einem komplexen Verhalten führt, daß periodisch, quasi-periodisch oder chaotisch sein kann.

Abstract

Long-period Variables (LPVs) and Miras are radially pulsating, highly evolved stars on the Asymptotic Giant Branch (AGB). Due to peculiar conditions of these objects, their cool, extended atmospheres are distinguished sites for the formation of complex molecules and dust particles. The interplay between dust formation and stellar radiation results in a circumstellar dust shell (CDS) generating slow mass loss, which finally enriches the interstellar medium (ISM) with processed material.

In view of the theory of dynamical systems, the CDS can be considered as nonlinear multi-oscillatory systems, whose eigenfrequencies and normal modes are controlled by the intrinsic time scales of various coupled physical and chemical processes. The aim of this work is to investigate the complex dynamical behaviour of carbon-rich CDSs in great detail. This is done by established methods of non-linear dynamics such as Fourier Analysis and the study of stroboscopic and Poincaré maps.

Especially CDSs surrounding stars with large stellar luminosities, tend to become dynamically unstable. They develop a self-maintaining oscillatory pattern purely caused by dust formation even without additional input of energy and mechanical momentum from the star (exterior κ -mechanism). Such a system has obviously an eigenmode.

In the case of lower stellar luminosities an eigenperiod of the system cannot be determined immediately, because the system generates neither a CDS nor self-induced shocks and outflows with self-maintained oscillatory pattern. An additional mechanical momentum input is needed, which is adopted to be irregular (white noise). A possible source of this is the convection in a red giant atmosphere.

It will be shown that, the interplay of the dust shell eigenmodes and a sinusoidal stellar pulsation leads to a complex oscillatory pattern. Due to the nonlinear behaviour of the system, the CDS may show periodic, quasi-periodic (multi-periodic) or chaotic oscillations.

Contents

| | |
|--|------------|
| Zusammenfassung | i |
| Abstract | iii |
| List of Figures | vii |
| List of Tables | ix |
| 1 Introduction | 1 |
| 2 Modelling method of CDSs | 7 |
| 2.1 Basic equations | 7 |
| 2.1.1 Hydrodynamics | 8 |
| 2.1.2 Thermodynamics | 9 |
| 2.1.3 Radiative transfer | 11 |
| 2.1.4 Chemistry | 13 |
| 2.1.5 Dust complex | 13 |
| 2.2 Numerical method | 16 |
| 2.2.1 Spatial and temporal discretisation | 16 |
| 2.2.2 Calculation of the CDS's dynamics | 16 |
| 2.2.3 Inner boundary condition | 17 |
| 3 Analysis of dynamics | 21 |
| 3.1 Diagnostic methods | 21 |
| 3.1.1 Fourier Transform | 21 |
| 3.1.2 Mapping | 30 |
| 3.2 Principle procedure of the data analysis | 32 |
| 3.2.1 Methodical details | 32 |
| 3.2.2 Influence of numerics | 34 |
| 3.3 Cooling behind shock waves | 35 |

| | | |
|----------|--|------------|
| 4 | CDSs around high luminous AGB stars | 43 |
| 4.1 | Exterior κ -mechanism | 43 |
| 4.2 | The CDS as oscillatory system | 44 |
| 4.3 | Periodically excited CDS | 47 |
| 4.3.1 | Excitation period | 48 |
| 4.3.2 | Excitation strength | 53 |
| 4.4 | Influence of stellar parameters | 56 |
| 4.4.1 | Stellar luminosity | 57 |
| 4.4.2 | Overabundance of carbon to oxygen | 59 |
| 4.4.3 | Stellar mass | 60 |
| 4.4.4 | Effective stellar temperature | 61 |
| 5 | CDSs around less luminous AGB stars | 67 |
| 5.1 | Eigendynamics of CDSs | 67 |
| 5.2 | Dynamics of perturbed CDSs | 73 |
| 5.2.1 | Perturbation frequency | 73 |
| 5.2.2 | Perturbation strength | 77 |
| 6 | Lightcurves and dynamics | 81 |
| 6.1 | Frequency-dependent radiative transfer | 81 |
| 6.2 | Spectral energy distribution | 82 |
| 6.3 | Synthetic lightcurves | 84 |
| 7 | Special application: IRC +10216 | 89 |
| 7.1 | Eigendynamics | 90 |
| 7.2 | Monoperiodic excitation | 93 |
| 7.3 | Spectra & lightcurves | 94 |
| 8 | Summary & outlook | 97 |
| | Appendix | 99 |
| A | FFT for the case $N = 8$ | 101 |
| | Bibliography | 110 |
| | Danksagung | 111 |

List of Figures

| | | |
|------|---|----|
| 1.1 | Physical representation of a dust-forming stellar wind | 4 |
| 3.1 | Sampling and aliasing | 26 |
| 3.2 | The FFT decomposition | 29 |
| 3.3 | Construction of a stroboscopic map | 31 |
| 3.4 | Behaviour of dynamic systems as seen in Poincaré maps | 31 |
| 3.5 | Snapshot of the fully developed radial shell structure of a CDS model | 32 |
| 3.6 | Overall velocity power spectrum of a CDS model | 33 |
| 3.7 | Stroboscopic and Poincaré map of a CDS model | 34 |
| 3.8 | Snapshot of the radial shell structure, power spectrum of velocity u and stroboscopic map of the (u, ρ, T) -phase space for the reference model in the case of an isothermal gas | 37 |
| 3.9 | Same as Fig. 3.8 but in the case of an adiabatic shock. | 39 |
| 3.10 | Same as Fig. 3.8 but in the case of a non-LTE shock | 40 |
| 4.1 | Self-induced radial structure of a CDS | 45 |
| 4.2 | Power spectrum of the radial gas velocity u purely caused by exterior κ -mechanism. | 46 |
| 4.3 | Temporal behaviour of Lagrangian zones for the case without internal pulsation | 47 |
| 4.4 | Most dominant frequencies of a CDS excited with various pulsation periods P | 49 |
| 4.5 | Power spectra and stroboscopic maps for a CDS excited with different periods P | 52 |
| 4.6 | Shift of CDS frequencies f_{CDS} as a function of excitation strength Δu | 53 |
| 4.7 | Power spectra and stroboscopic maps for a CDS excited with a period $P = 1500$ d, but with different strengths Δu | 56 |
| 4.8 | Temporal behaviour of some Lagrangian zones in the case with internal pulsation | 57 |
| 4.9 | Dependencies on the stellar luminosity L_* | 59 |

| | | |
|------|--|----|
| 4.10 | Dependencies on the carbon to oxygen ratio C/O | 61 |
| 4.11 | Dependencies on the stellar mass M_* | 63 |
| 4.12 | Dependencies on the stellar effective temperature T_* | 65 |
| 5.1 | Stochastic movement of the inner boundary R_{in} and associated velocity u_{in} | 68 |
| 5.2 | Radial structures of stochastic excited CDS | 69 |
| 5.3 | Mean power spectra of the radial gas velocity u caused by different stochastic excitation σ | 71 |
| 5.4 | Selected mean power spectrum profiles of the gas velocity u at different radii for two noise intensities σ | 72 |
| 5.5 | Most dominant frequencies of the CDS, periodically-disturbed with various pulsation periods P | 74 |
| 5.6 | Power spectra of the local expansion velocity u , corresponding maps of the (u, ρ, T) phase space for different periodic excitation periods P | 76 |
| 5.7 | Most dominant frequencies of the CDS excited with a fixed excitation period $P = 376$ d, but different strength Δu | 78 |
| 6.1 | Comparison between the SEDs of the dust shell model A resulting from various stellar excitations | 83 |
| 6.2 | Synthetic lightcurves of model A for various excitations at different wavelengths | 85 |
| 6.3 | Synthetic lightcurves of model B for various excitations at different wavelengths | 87 |
| 7.1 | Mean power spectra of the radial gas velocity u of the stochastic excited IRC +10216 model | 91 |
| 7.2 | Selected mean power spectrum profiles of the gas velocity u at various radii of the stochastic excited IRC +10216 model | 92 |
| 7.3 | Power spectrum of velocity u and maps of the (u, ρ, T) -phase space of the periodically excited IRC +10216 model | 93 |
| 7.4 | Comparison between calculated and observed SED of IRC +10216 | 95 |
| 7.5 | Comparison between calculated and observed lightcurves of IRC +10216 | 96 |

List of Tables

| | | |
|-----|--|----|
| 2.1 | Element abundances for the gas phase | 13 |
| 3.1 | Elementary properties of the Fourier transform | 22 |
| 3.2 | Correspondence between symmetries in the two domains | 23 |
| 3.3 | The FFT bit reversal sorting | 29 |
| 3.4 | Resultant quantities of the reference CDS with different treatment of the radiating shock waves. | 38 |
| 4.1 | Resultant quantities from the periodically disturbed CDS model A | 51 |
| 4.2 | Resultant quantities of the excitation strength Δu study of model A for $P = 388$ d | 54 |
| 4.3 | Resultant quantities of the excitation strength Δu study of model A for $P = 1500$ d | 55 |
| 4.4 | Influence of the stellar luminosity L_* on the CDS dynamics | 58 |
| 4.5 | Influence of the carbon to oxygen ratio C/O on the CDS dynamics | 60 |
| 4.6 | Influence of the stellar mass M_* on the CDS dynamics | 62 |
| 4.7 | Influence of the stellar effective temperature T_* on the CDS dy- namics | 64 |
| 5.1 | List of model calculations and resultant quantities for stochasti- cally excited model B | 70 |
| 5.2 | Resultant quantities from the periodically disturbed CDS model B | 75 |
| 5.3 | Resultant quantities of the excitation strength Δu study of model B for $P = 376$ d | 79 |
| 7.1 | List of model calculations and resultant quantities for the stochas- tic excited IRC +10216 model | 91 |

Chapter 1

Introduction

Long-period variables (LPVs) and Miras are highly evolved stars located on the asymptotic giant branch (AGB) with stellar luminosities up to $10^4 L_{\odot}$ and typical effective temperatures of less than 3000 K. They exhibit slow, massive stellar winds with final outflow velocities u_{∞} in the range of some 10 km s^{-1} and mass loss rates \dot{M} as high as $10^{-4} M_{\odot} \text{ yr}^{-1}$.

A common feature of these late-type stars is the modulated absorption of radiation in the stellar interior, also known as the interior κ -mechanism. The process is named after the Greek letter kappa κ , the symbol for the absorption coefficient of stellar material. It operates as follows: in partially ionised hydrogen regions within the star, small random increases in density produce increased opacity and thus increased absorption of energy from the stellar interior. This causes heating and expansion of the layer, which overshoots its rest position and leads to a drop in pressure, density, temperature and opacity. The effect then reverses, setting up an oscillation and causing the star's outer layers to pulsate radially (Cox (1983)). The pronounced time variations exhibit a more or less well-defined periodicity with periods ranging from approximately (100-1000) days (Whitelock et al. (1991)) with a maximum by number of 350 days (Hoffmeister et al. (1990)).

The internal pulsations lead to the generation of hydrodynamical waves, which travel outwards into a medium with decreasing density and temperature causing the waves to increase in amplitude and finally grow and steepen into shock waves. These shock fronts move outwards through the stellar atmosphere and have a significant bearing on the local thermal and chemical state, producing either favourable or non-favourable conditions for dust formation. This yields the formation of thermodynamic regimes where the gas-solid phase transition is possible and which allow effective dust nucleation and subsequent growth (dust-forming window). Radiation pressure on the newly formed dust accelerates the matter and finally, results in the formation of a spatially extended oscillating circumstellar dust shell (CDS) surrounding the central star.

There has been a long-lasting debate about whether these stars pulsate in the fundamental mode or in the first overtone (Wood (1995)). The problem becomes even more intriguing, if the complex behaviour of the CDS is also taken into account. Since the early work of Eddington & Plakidis (1929) it has been known that the pulsations of Miras are not strictly regular, but show random cycle-to-cycle variations in period and, to a less degree, in amplitude. A more recent study by Percy & Colivas (1999) based on a database of times and magnitudes of maximum and minimum brightness of 391 bright Mira stars over a timeframe of 75 years, revealed that the majority of the observed Mira light curves exhibit irregularities over intervals of about 20 cycles. They concluded that these fluctuations are at least partially due to the phenomenon of dust formation.

This study aims the detailed understanding of the dynamics of a CDS. With regard to the theory of dynamical systems, oscillating circumstellar shells may be conceived as multi-oscillatory systems, whose eigenfrequencies and normal modes are controlled by the intrinsic time scales of the various coupled physical and chemical processes. Due to the inherently non-linear nature of the underlying equations, an element of randomness is added to the stellar pulsation (Icke et al. (1992)).

The interplay between the dust formation and the stellar radiation field strongly influences the stellar wind and can even results in a self-sustained oscillation of the circumstellar shell. This phenomenon is termed as exterior κ -mechanism. High luminosity AGBs, for instance develop such a self-maintaining oscillatory pattern, which is purely caused by dust formation even without additional input of mechanical momentum from the stellar pulsation (Fleischer et al. (1995), Höfner et al. (1996)). A smooth density gradient combined with low temperatures in the so called dust formation window allows nucleation and growth of dust particles. In the case of lower stellar luminosities the system does not develop a CDS by the exterior κ -mechanism. Such objects have to be supported by an additional input of mechanical momentum and energy by e.g. a stellar pulsation to initiate a CDS generating mass loss. The eigenperiod of the system cannot be determined immediately, because the system does not generate self-induced shocks by the exterior κ -mechanism.

To examine their complex dynamical behaviour such systems are excited using stochastic white noise. This allows for a much easier detection of the eigenmodes of the shells due to the broad frequency spectrum of the stochastic force. In the case of CDSs around less luminous AGBs, the circumstellar shell can be described as a multi-oscillatory system which is kicked by the pulsating stellar atmosphere. The resulting dynamical behaviour of the complete system depends on both the frequency and strength of the stellar oscillation as well as on the intrinsic dynamics of the circumstellar shell.

Depending on the physical parameters, an internal harmonic excitation may result in either periodic, quasi-periodic (multi periodic) or chaotic oscillations. This work analyses and discusses such oscillatory patterns in view of the previously determined eigenmodes of the dust shells.

Modelling of CDSs has to take into account the coupling of matter and radiation, which means that the time-dependent equations describing the hydrodynamics, thermodynamics, radiative transfer, equilibrium chemistry, and dust formation and growth have to be solved self-consistently. Figure 1.1 shows the interaction of the various physical processes describing a dust-driven wind. The numerical results of the models are analysed by different standard techniques commonly used for the characterisation of non-linear systems. It will be shown that stroboscopic maps and Poincaré maps are well suited to investigate the internal dynamics of the system. Many results have been obtained by applying the Fourier Transform (FT) approach.

This thesis is organised as follows:

Chapter 2 gives a brief outline of the modelling method. The theoretical model of a CDS is conceived as the complete unique set of solutions of an appropriate system of fundamental equations, comprising the conservation laws, transport equations, and constitutive equations which describe both the local and global physical situation of the CDS and the various inherent processes e.g. dust formation. The basic equations are listed and the solving procedure is described.

Chapter 3 provides a short description of the methods used to investigate the dynamical behaviour of the star-CDS-system. It contains a detailed description of the Fourier Analysis and its numerical realisation via the Fast Fourier Transform (FFT) algorithm and the deterministic approach of mapping. It also presents the principle procedure of the data analysis.

Chapter 4 presents the analysis of CDS dynamics around high luminous AGBs. This includes the phenomenon of CDSs excited solely by the exterior κ -effect and the interplay with an interior pulsation of the star. In a parameter study the dependence of the exterior κ -mechanism on the stellar parameters is investigated.

Chapter 5 deals with the dynamics of CDSs around AGBs ranging from weak up to standard luminosities. Note, that a purely dust-driven wind is not possible for such stars. In order to determine the eigendynamics of the CDS, stochastic excitations are taken into account. In addition, the complex interaction between the interior pulsation of the star and the multi-oscillatory circumstellar shell is dis-

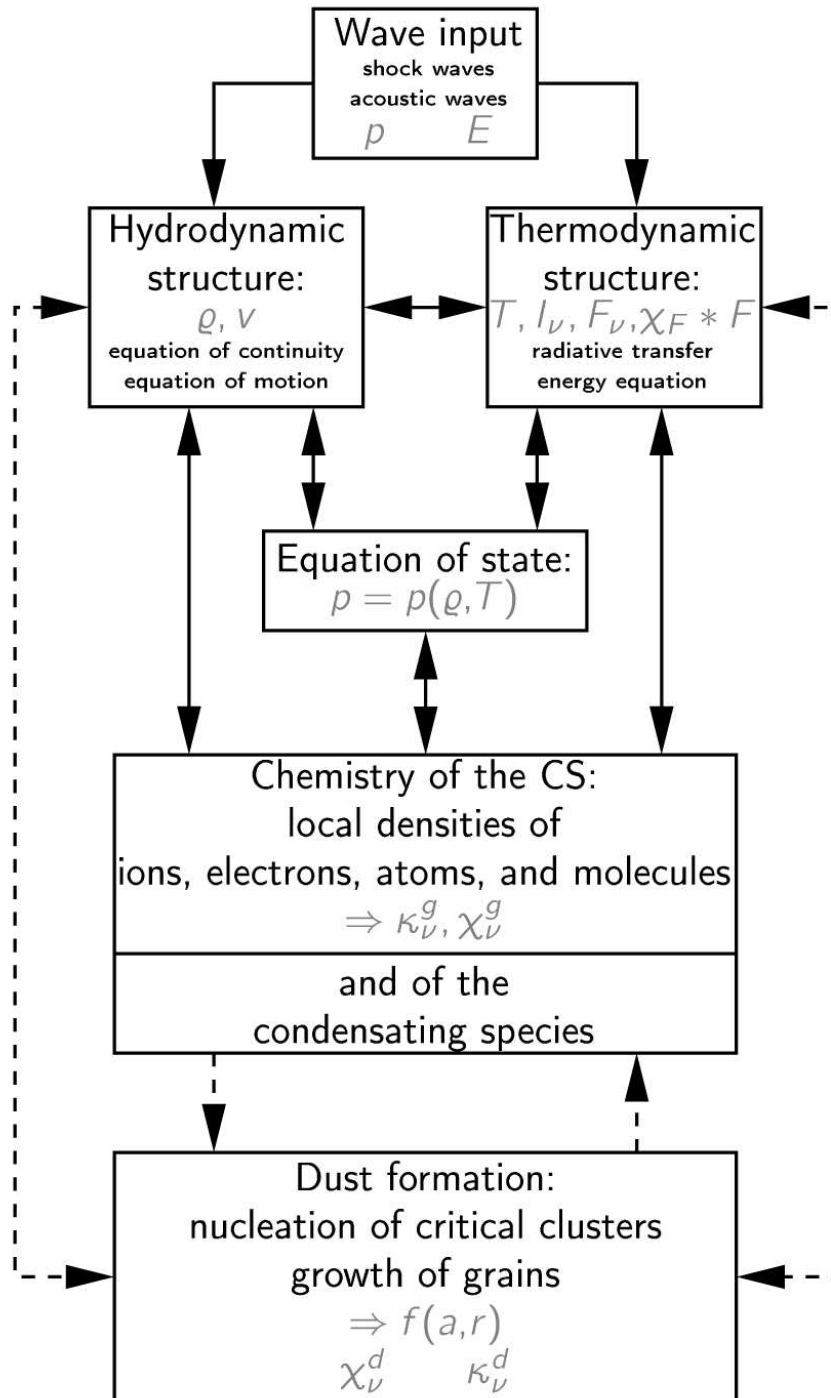


Figure 1.1: Physical representation of a dust-forming stellar wind. Taken from Sedlmayr & Winters (1996)

cussed.

Chapter 6 establishes the connection to the observations. The optical appearance of several, already discussed CDSs is presented in the form of synthetic lightcurves. Also shown are the emergent spectra.

Chapter 7 contains a special application of the developed analysis method to a parameter set found to well reproduce the individual object IRC +10216. It is a prototype of an extreme carbon star and probably one of the best studied stars in the sky. The CDS-dynamics is examined and the synthetic spectra and lightcurves are compared to specific observations.

Chapter 8 summarises the results and discusses the conclusion of this work.

Appendix is related to Chapter 3 and describes in detail the Fast Fourier Transform (FFT) procedure for a convenient number of 8 data samples.

Chapter 2

Modelling method of CDSs

2.1 Basic equations

The approach used in this work to model the circumstellar dust shells (CDSs) around C-rich Miras and LPVs is based on a program code, which was developed in its original form by Fleischer (1994), Gauger et al. (1990), and Gail & Sedlmayr (1988). In the following this code will be referred to by the abbreviation FGSG, which stands for the initials of the authors of the first of the above cited papers. Further developments of this code by Woitke (1997) and Schirrmacher (2003) are also used in this work.

In general, the code includes the explicit solution of time-dependent hydrodynamics, thermodynamics, radiation transfer, equilibrium chemistry, and a detailed treatment of dust nucleation, growth, and evaporation. Starting from a given hydrostatic and dust free initial state the purpose of this code is to yield a self-consistent model of both the temporal evolution and the spatial stratification of all relevant physical and chemical quantities which determine the overall dynamics of the dust shells. The code assumes spherically symmetric CDSs around pulsating red giants with mass M_* , effective temperature T_* , luminosity L_* , and pulsation period P , which reduces 3-dimensional geometry to 1-dimension. The gas and dust are assumed to be co-moving and are treated as a single continuous fluid, i.e. the drift velocity of the grains with respect to the gas is neglected. The movement of the gas and dust are assumed to be correlated. Therefore, position coupling between dust and gas is presumed.

The following chapter gives a short overview of the basic equations underlying this numerical code.

2.1.1 Hydrodynamics

Instead of the field description of an Eulerian approach the FGSG-code uses Lagrangian variables to solve the equations. The Lagrangian expression of the hydrodynamic problem considers the individual path of small fluid mass elements in a co-moving frame. R denotes the radial position of a fluid element, which is described by the Lagrangian variables r and t , i.e. $R = R(r, t)$. Then r is the reference configuration at the time t_0 with $r = R(r_0, t_0)$, wherein r_0 specifies which fluid element is being considered. The velocity u of a fluid element is given by the partial derivative:

$$u = \frac{\partial R}{\partial t} . \quad (2.1)$$

The *equation of motion* in Lagrangian formulation corresponds to:

$$\frac{\partial u}{\partial t} = -V_0 \left(\frac{R}{r} \right)^2 \frac{\partial p}{\partial r} - a_{\text{tot}} , \quad (2.2)$$

wherein V_0 is the specific volume at time t_0 and p is the thermal pressure, and a_{tot} is the total acceleration due to external forces acting on the fluid element.

The most important external forces in the case of AGB-stars are gravitational deceleration a_{grav} and acceleration due to the radiation pressure a_{rad}

$$a_{\text{tot}} = a_{\text{grav}} + a_{\text{rad}} = -\frac{GM(R)}{R^2} + \frac{4\pi \chi_H}{c \rho} H(R) \quad (2.3)$$

with χ_H being the flux weighted mean of the extinction coefficient, G the gravitational constant, and c the speed of light. $M(R)$ is the enclosed mass within the radial distance R and may be written as:

$$M(R) = M_* + M_{\text{CDS}}(R) . \quad (2.4)$$

Since the mass contained in the circumstellar dust shell M_{CDS} is so small compared to the mass of the star M_* , $M(R)$ is approximated by M_* .

The frequency integrated Eddington flux H at position R in the case of radiative equilibrium is:

$$H(R) = H_* \left(\frac{R_*}{R} \right)^2 \quad (2.5)$$

where the Eddington flux H_* at the stellar surface R_* can be declared in terms of the stellar luminosity L_* such that:

$$H_* = \frac{L_*}{16\pi^2 R_*^2} . \quad (2.6)$$

The radiative acceleration a_{rad} expressed in units of the local gravitational deceleration a_{grav} introduces a function α

$$\alpha(R) = \frac{a_{\text{rad}}}{a_{\text{grav}}} = \frac{L_*}{4\pi cGM(R)} \frac{\chi_H}{\rho} . \quad (2.7)$$

Now, Eq. (2.2) can be clearly defined. The final form of the equation of motion reads as follows:

$$\frac{\partial u}{\partial t} = -V_0 \left(\frac{R}{r} \right)^2 \frac{\partial p}{\partial r} - \frac{GM_*}{R^2} (1 - \alpha) . \quad (2.8)$$

2.1.2 Thermodynamics

The gas temperature T_g can be regarded as an implicit result of the solution of the *energy conservation equation*:

$$\frac{\partial e}{\partial t} = -p \frac{\partial V}{\partial t} + \dot{Q} \quad (2.9)$$

wherein e is the specific internal energy, i.e. internal energy per unit mass and V the specific volume. The first term on the left hand side in Eq. (2.9) (also called adiabatic heating/cooling rate \dot{Q}_{ad}) stands for the expansion/compression work performed by the thermal gas pressure p . The second term is the net heating rate $\dot{Q} = \dot{Q}_{\text{rad}} + \dot{Q}_{\text{vis}}$ where \dot{Q}_{rad} denotes the net radiative rate of energy exchange between the gas and the radiation field and \dot{Q}_{vis} the viscous heating rate, which describes the heating of the gas by dissipation of the shock waves energy due to an artificial viscosity pressure. In this work, the calculation of the net heating rate \dot{Q} follows two different approaches of the gas model.

Mono-atomic ideal gas model

Fleischer et al. (1992) model the gas consisting of electrons, ions or atoms as a mono-atomic ideal gas, i.e. the gas has only three translational degrees of freedom. Consequently, the ideal gas law is used as an *equation of state*:

$$p = \frac{\rho}{\mu m_{\text{H}}} k_{\text{B}} T_g \quad (2.10)$$

with T_g being the gas temperature. In this approach, μ the mean molecular weight of the gas particles in units of mass of a hydrogen atom m_{H} is taken to be constant

for an ideal gas. A molecular weight of $\mu = 1.27$ is used, which arises from a H/He ratio by number of 10 : 1 and the assumption that all hydrogen H is present as H-atoms rather than in H₂-molecules. The set of equations (2.2), (2.9) is completed by the caloric equation of state which gives the specific energy e of the gas components:

$$e = \frac{f}{2} \frac{1}{\mu m_{\text{H}}} k_{\text{B}} T_{\text{g}} = \frac{p}{\rho(\gamma - 1)} \quad (2.11)$$

wherein three degrees of freedom $f = 3$ leads to an adiabatic index of $\gamma = 5/3$. The complex heating/cooling rates \dot{Q} in the shock front are treated in the following two limiting cases:

- Isothermal limit

The cooling behind the shock front is assumed to take place instantaneously. Therefore, T_{g} equals the local radiative equilibrium temperature T_{RE} at every instant of time throughout the shell. This means that radiative cooling has to be extremely effective behind the shock front. T_{RE} is given by Eq. (2.21). Since $T_{\text{g}} = T_{\text{RE}}$ Eqs. (2.9) and (2.11) do not have to be solved.

- Adiabatic limit

If the energy exchange between the gas and the radiation field becomes ineffective an adiabatic approximation may be used. In this case $\dot{Q}_{\text{rad}} = 0$ is assumed and the cooling is given by the adiabatic heating/cooling term $\dot{Q}_{\text{ad}} = -p \frac{\partial V}{\partial t}$ only describing the mechanical work performed by the gas.

Multicomponent non-LTE ideal gas model

In the general case of a non-local thermal equilibrium (non-LTE) the calculation of \dot{Q} requires a detailed treatment of the radiative transfer which couples the physical state of the gas and dust component non-linearly and non-locally. Woitke (1997) and Schirrmacher (2003) describe the gas as a multicomponent mixture of various atoms, molecules, ions and electrons. The molecular weight μ is no longer a constant, being a function of density and gas temperature. The thermal *equation of state* reads:

$$\begin{aligned} p &= p_{\text{atoms}} + p_{\text{molecules}} + p_{\text{ions}} + p_{\text{electrons}} \\ &= (n_{\text{atoms}} + n_{\text{molecules}} + n_{\text{ions}} + n_{\text{electrons}}) k_{\text{B}} T_{\text{g}} \end{aligned} \quad (2.12)$$

where p_{species} is the partial pressure of the regarded species, i.e. atoms, molecules, ions, electrons and n_{species} the corresponding particle density. Since all relevant excitation states are considered the internal energy can be written as the sum of all

energies gained from interaction processes between matter-radiation and matter-matter, respectively:

$$e = \frac{1}{\rho}(E_{\text{trans}} + E_{\text{rot}} + E_{\text{vib}} + E_{\text{el}} + E_{\text{ion}} + E_{\text{diss}}). \quad (2.13)$$

The above include in particular the translation energy of the gas particles E_{trans} , the rotational energy of molecules E_{rot} , the vibrational energy of molecules E_{vib} , the excitation energy of electrons E_{el} , the ionisation energy of the ions E_{ion} and the dissociation energy of the molecules E_{diss} . Then, the radiative heating/cooling rate \dot{Q}_{rad} is the result of summing up all microscopic rates.

2.1.3 Radiative transfer

The determination of the dust and gas temperature T_{g} requires knowledge of the radiation temperature T_{rad} , which results from solving the radiative transfer problem. Since the hydrodynamic time scales are much larger than typical photon crossing times in the envelopes of red giants, a time independent (stationary) spherical radiative transfer is considered:

$$\mu \frac{\partial I_{\nu}}{\partial r} + \frac{1 - \mu^2}{r} \frac{\partial I_{\nu}}{\partial \mu} = -\kappa_{\nu}(I_{\nu} - S_{\nu}). \quad (2.14)$$

Appropriate for extended stellar atmospheres the problem is treated using a two stream Eddington approximation in spherical symmetry as developed by Lucy (1971, 1976), and Unno & Kondo (1976). Their approach splits the radiation field I at each point $r > R_*$ into two streams $I^+(r)$ and $I^-(r)$ originating directly from the central star and the surrounding extended shell, respectively. By solving the so-called moment equations of the radiative transfer equation one obtains a temperature structure. In this work the radiative transfer problem is solved assuming firstly radiative equilibrium (RE)^a, secondly local thermodynamical equilibrium (LTE)^b, and thirdly applying a grey approximation^c.

Lucy

According to Lucy (1971, 1976), the radiation field at a distance r from the star comprises the sum of the attenuated radiation originating directly from the star

^aRE: $\int \kappa_{\nu} J_{\nu} d\nu = \int \epsilon_{\nu} d\nu$ with J_{ν} being the angle-averaged intensity I_{ν}
^bLTE with Kirchhoff's law: $\epsilon_{\nu} = \kappa_{\nu} B_{\nu}(T)$ follows RE-LTE: $\int \kappa_{\nu} J_{\nu} d\nu = \int \kappa_{\nu} B_{\nu}(T_{\text{RE}}) d\nu$
and $\int B_{\nu}(T_{\text{RE}}) d\nu = \sigma/\pi T_{\text{RE}}^4$
^c $\kappa_{\nu} = \kappa = \text{const}$

plus the scattered radiation. The separation angle μ_* between the two radiation streams is in this treatment purely determined by geometry such that:

$$\mu_* = \sqrt{1 - \left(\frac{R_*}{r}\right)^2}, \quad (2.15)$$

where R_* denotes the stellar radius. Equation (2.15) yields a modified Eddington approximation:

$$J - 3K + \frac{1}{2}\mu_*F = 0, \quad (2.16)$$

where J, F and K are the first three moments of the specific intensity I. By building the first two moments of the radiative transfer equation (2.14) and applying the above closure condition an expression for the radial temperature structure is obtained:

$$T_{\text{RE}}^4(r) = \frac{T_{\text{eff}}^4}{2} \left(2W + \frac{3}{2}\tilde{\tau}(r) \right) \quad (2.17)$$

with

$$W = \begin{cases} 1 & : r \leq R_* \\ 1 - \sqrt{1 - \left(\frac{R_*}{r}\right)^2} & : r > R_* \end{cases} \quad (2.18)$$

describing the geometrical dilution factor of the radiation field with increasing distance to the star, and

$$\tilde{\tau}(r) = \int_r^\infty \kappa\rho \left(\frac{R_*}{r'}\right) dr' \quad (2.19)$$

corresponding to an optical depth. $\tilde{\tau}(r)$ fulfils the conditions $\tilde{\tau}(R_*) = 2/3$ at the photospheric radius R_* and $\tilde{\tau}(\infty) = 0$ at the outer boundary.

Unno & Kondo

In the case of optically thick shells, the edge of the star can not be clearly seen. Therefore, it is no longer possible to distinguish between the two streams. To overcome this problem Unno & Kondo (1976) replaced the separation angle μ_* by a variable μ_r which is determined according to the following differential equation:

$$\frac{\partial \mu_r^3}{\partial r} = \frac{\chi_H}{4} + \frac{3\mu_r}{r} - \frac{5}{4}\chi_H\mu_r^2 - 3\frac{\mu_r^3}{r} \quad (2.20)$$

with the inner boundary condition $\mu_{R_*} = 0$. Then, the stratification of the radiative equilibrium temperature T_{RE} can be written as:

$$T_{\text{RE}}^4(r) = \frac{T_{\text{eff}}^4}{2} R_*^2 \left[\frac{1}{(1 + \mu_{R_{\text{out}}}) R_{\text{out}}^2} + \frac{\mu_{R_{\text{out}}}}{R_{\text{out}}^2} - \frac{\mu_r}{r^2} + \frac{3}{2} \int_r^{R_{\text{out}}} \left(\frac{\chi_H}{r'^2} + \frac{2\mu_{r'}}{r'^3} \right) dr' \right], \quad (2.21)$$

with R_{out} as the outer boundary.

2.1.4 Chemistry

The gas is assumed to be in chemical equilibrium (CE), hence the chemistry is expected to be independent of time. A fixed photospheric solar abundance ϵ is adopted for all chemical elements according to Allen (1973) (see Table 2.1). Only the carbon abundance ϵ_C is determined by the ratio of the abundance of carbon to oxygen C/O and therefore can be regarded as a free model parameter. Throughout this work a carbon rich element mixture is assumed, i.e. the C/O - ratio is greater than unity. Due to the high binding energy of the CO molecule (about 11 eV), nearly all oxygen is completely consumed by the formation of this molecule. Consequently, only carbon is available for the formation of the high temperature condensates. The C/O-ratio determines the amount of carbon available for the grain formation. Especially considered are the concentrations of number densities of H, H₂, C, C₂, C₂H and C₂H₂.

Table 2.1: Element abundances for the gas phase

| Element | Value |
|------------------------------|---------------------------|
| $\log(\epsilon_{\text{H}})$ | 0.00 |
| $\log(\epsilon_{\text{He}})$ | -1.00 |
| $\log(\epsilon_{\text{O}})$ | -3.18 |
| ϵ_C | C/O ϵ_{O} |

2.1.5 Dust complex

Dust formation can be regarded as a two-step process, consisting of firstly nucleation of small critical clusters from the gas phase and secondly subsequent growth to macroscopic dust grains. The dust nucleation is described by a modified classical nucleation theory for heteromolecular, homogeneous carbon grains according

to Gail et al. (1984) and Gail & Sedlmayr (1988). Dust growth and evaporation can be treated by a moment method developed by Gail & Sedlmayr (1988) and Gauger et al. (1990), where the moments K_i are formed of the local size distribution function of the dust grains $f(N, t)$:

$$K_i(N, t) = \sum_{N=N_\ell}^{\infty} N^{i/d} f(N, t) / n_{\text{H}} \quad i = 0, 1, 2, \dots \quad (2.22)$$

with N being the particle size defined by the number of monomers contained in a dust particle and N_ℓ being the lower limit size of a dust particle contributing to the size distribution^d. n_{H} is the total number density of hydrogen atoms whereas d denotes the spatial dimension of the grains and is set to $d = 3$ for spherical particles. The moments up to $i = 3$ are related to physical dust properties:

1. Number density of particle of size $\geq N_\ell$:

$$n_{\text{d}} = K_0 n_{\text{H}}$$

2. Number density of monomers condensed into grains of size $\geq N_\ell$:

$$n_{\text{c}} = K_3 n_{\text{H}}$$

3. Mean particle radius:

$$a_{\text{m}} = a_0 \frac{K_1}{K_0}$$

with a_0 the hypothetical radius of a monomer.

4. Degree of condensation:

$$f_{\text{cond}} = \frac{K_3}{n_{\text{cond}}} = \frac{n_{\text{c}}}{(\epsilon_{\text{C}} - \epsilon_{\text{O}})}$$

i.e. the amount of material actually condensed into dust grains divided by the number density of condensable material in the pure gas phase $n_{\text{cond}} = (\epsilon_{\text{C}} - \epsilon_{\text{O}}) / n_{\text{H}}$.

The time evolution of the first four dust moments is given by the following non-linear coupled system of equations (Gauger et al. (1990)):

^dUsually N_ℓ can be chosen in the range $10^2 \dots 10^3$.

$$\begin{aligned}\frac{dK_0}{dt} &= J(N_\ell, t) \\ \frac{dK_i}{dt} &= N_\ell^{i/d} J(N_1, t) + \frac{1}{\tau} \frac{i}{3} K_{i-1} \quad i = 1, 2, 3\end{aligned}\quad (2.23)$$

wherein $J(N_\ell, t)$ is the nucleation rate of clusters of size N_ℓ . It is assumed that $J(N_\ell, t)$ corresponds to the stationary nucleation rate J_* . The quantity τ^{-1} corresponds to the net growth rate and includes the growth rate τ_{gr}^{-1} as well as the evaporation rate τ_{ev}^{-1} .

Transport coefficients

The equation of motion (Sect. 2.1.1) as well as the equations of the radiative transfer (Sect. 2.1.3) contain the flux weighted extinction coefficient χ_H . By neglecting scattering by molecules and dust grains, the extinction coefficient can be calculated by the sum of the dust opacity κ_d and of the gas opacity κ_g :

$$\chi = \chi_g + \chi_d = \kappa_g + \kappa_d \quad (2.24)$$

A frequency averaged constant gas opacity $\kappa_g = 2 \cdot 10^{-4} \text{ cm}^2 \text{ g}^{-1}$ has been used such as e.g. Bowen (1988), Fleischer et al. (1992), Feuchtinger et al (1993), Winters et al. (1997). This value is based on the Rosseland-mean opacities taken from Alexander et al. (1983). In this work the small κ_g value is used to stress the interaction between radiation and the dust component (see Helling et al. (2000), Sandin (2008)).

Since the size of the dust grains a is assumed to be small compared to the wavelength λ of the radiation field, the dust opacity κ_d is calculated in the small particle limit of the Mie Theory ($2\pi a \ll \lambda$). Then, the dust opacity can be expressed according to Gail & Sedlmayr (1987) by:

$$\kappa_d = \frac{3}{4} V_0 K_3 Q'(T_d) \quad (2.25)$$

where V_0 is the volume of a monomer in the condensed phase. $Q'(T_d)$ is the extinction efficiency of a dust grain $Q^{\text{abs}}(\nu, a)$ divided by the grain radius a (Lucy (1976)), which is approximated by a power law:

$$Q'(T_d) = Q_0 T_d = 5.9 T_d \quad (2.26)$$

wherein for optically thick dust shells Q_0 was replaced by the Rosseland mean opacity. The dust temperature corresponds to the radiation temperature, i.e. $T_d = T_{\text{rad}}$.

2.2 Numerical method

The numerical solution of the systems of partial differential equations (PDEs) describing the evolution of the CDS requires an adaptive mesh method in space and time.

2.2.1 Spatial and temporal discretisation

The discretisation of the system of partial differential equations (PDEs) (2.8), (2.17), (2.19), and (2.23) in spatial coordinates follows the approach of Richtmyer & Morton (1967). Extensive state variables are defined between two grid points, whereas intensive variables are defined at the position of the respective grid points. To ensure a sufficiently fine spatial resolution of the gridpoints N_{grid} the numerical scheme requires rezoning or remapping, i.e. the insertion of grid points where the width of the Lagrangian element has become too large. Grid points beyond the actual outer boundary R_{out} are removed and new ones are inserted into the inner integration region at R_{remap} . Thereby, the redistribution procedure requires the conservation of the physical quantities. For more details see Fleischer (1994).

The time-dependent equations are solved by an explicit integration in time. Since the physical and chemical processes involved act on different, individual time scales, the temporal resolution for the whole system has to satisfy several criteria to guarantee an accurate resolution of all these time scales. The appropriate time step at a given time is determined by the minimum of the following criteria:

- $\Delta t \leq P/200$ temporal resolution of the pulsation period P
- $\Delta t \leq \delta(\Delta r/c_s)$ known as the Courant-Friedrichs-Levy (CFL) condition with δ in order of 10^{-2} as CFL-factor, c_s the local sound velocity and Δr the width of the Lagrangian element.
- $\Delta t \leq \Delta V/V \leq 0.2$ temporal change of the relative specific volume
- $\Delta t \leq \Delta q/q \leq 0.1$ maximum relative change of a certain dust quantity q

2.2.2 Calculation of the CDS's dynamics

Calculations of the CDS's dynamics require an initial start configuration, corresponding to a hydrostatic and dust free atmosphere. This hydrostatic structure is constructed for a set of initial stellar parameters, which are: luminosity

$L_* = L_*(t = 0)$, mass $M_* = M_*(t = 0)$, and temperature $T_* = T_*(t = 0)$ on an equidistant radial grid with 512 points. The stellar radius R_* is determined by the Stefan-Boltzmann law:

$$L_* = 4\pi R_*^2 \sigma T_*^4, \quad (2.27)$$

where σ is the Stefan-Boltzmann constant. By integrating the time-independent, dust-free equation of motion (2.8) the pressure stratification can be calculated immediately. Assuming $T(R_*) = T_*$ results in the inner boundary condition $\tilde{\tau}(R_*) = 2/3$ at the photospheric radius and $\tilde{\tau}(\infty) = 0$ at the outer boundary. The temperature structure is assuming grey radiative transfer according to Lucy (1971, 1976) (cf. Sect. 2.1.3). Finally, the density stratification can be calculated from the ideal gas law.

To start the dynamical calculation further initial parameters are required: the pulsation period P , the velocity amplitude Δu or the intensity of the noise σ for the stellar pulsation and the carbon-to-oxygen ratio C/O for the calculation of the dust complex. After switching on the pulsation, the velocity amplitude is slowly increased until the desired final value Δu is reached. This is done in order to avoid numerical instabilities caused by the first wave which moves into an exponential density gradient and, therefore, would steepen into an enormous shock wave. To model the shock waves in Lagrangian coordinates, an artificial viscosity term has to be introduced. Thereby, the approximation of Tscharnuter & Winkler (1979) is applied to broaden the shock fronts by considering a viscous pressure tensor.

The calculations, i.e. the explicit forward integration in a co-moving Lagrangian frame with an adaptive grid, are performed at first on a small spatial grid with an outer boundary $R_{\text{out}} = 2 R_*$. With time increasing, the CDS becomes more extended and R_{out} has to be increased until it has reached its final value. Grid points moved across the actual outer position of R_{out} are discarded and new ones are inserted into the inner integration domain at R_{remap} at every time interval t_{remap} . The transient phase of the system after switching on the pulsation is mainly determined by the initial condition and by the increase in Δu . Therefore, only data obtained after a model running time of $t = 160\,000$ d were analysed. At this time the model has relaxed towards a "stable" state (periodic or irregular).

2.2.3 Inner boundary condition

The inner boundary condition to be specified for the calculation of the dynamical structure of a circumstellar dust shell (CDS), can be physically determined by the pulsation of the stellar envelope. The inner boundary, located a few scale heights below the stellar radius (Höfner et al. (1996)) is driven by an internal

κ -mechanism. Since in time-dependent modelling it is not possible to solve simultaneously the creation of pulsation at the interior of the star together with the corresponding reaction of the atmosphere, the pulsation of the star is taken for granted. This leads to the application of the so called ‘‘piston approximation’’ (cf. Wood (1979), Bowen (1988)). In this work three different approaches of this inner boundary approximation are used:

Monoperiodic pulsation

The radius of the inner boundary R_{in} performs a radial, harmonic oscillation around an equilibrium position R_0 . Consequently, the local velocity u_{in} , also oscillates sinusoidally with time:

$$\begin{aligned} R_{\text{in}}(t) &= R_0 + \Delta u \left(\frac{P}{2\pi} \right) \sin \left(\frac{2\pi}{P} t \right) \\ u_{\text{in}}(t) &= \Delta u \cos \left(\frac{2\pi}{P} t \right) \end{aligned} \quad (2.28)$$

At time $t = nP$, $n \in \mathbb{N}_0$ the inner boundary takes its initial position R_0 .

Without pulsation

To handle the CDSs around stars without pulsation, the internal excitation induced by the piston at the inner boundary is switched off by setting the piston amplitude to be zero, i.e. $\Delta u = 0$

$$\begin{aligned} R_{\text{in}}(t) &= R_0 \\ u_{\text{in}}(t) &= 0 \end{aligned} \quad (2.29)$$

Stochastic pulsation

In order to describe the input of convection a stochastic movement of the inner boundary R_{in} around an equilibrium position R_0 , analogous to the piston approximation is introduced. This can be described by the following stochastic integral equation:

$$\begin{aligned} R_{\text{in}}(t) &= R_0 + \int_0^t u_{\text{in}}(t') dt' \\ u_{\text{in}}(t) &= \Gamma(t) \end{aligned} \quad (2.30)$$

The term $\Gamma(t)$ describes the influence of the randomness or noise and is taken to be Gaussian distributed with zero mean:

$$\langle \Gamma \rangle = 0. \quad (2.31)$$

Since white noise is adopted, $\Gamma(t)$ is uncorrelated in time which corresponds to the (auto)correlation function $G(\tau)$ being Dirac's δ -function:

$$G(\tau) = \langle \Gamma(t)\Gamma(t + \tau) \rangle = \sigma^2\delta(\tau), \quad (2.32)$$

where σ^2 scales the intensity of the noise. The integral over the Gaussian white noise, i.e. the solution of Eq. (2.30), gives the so called Wiener process. It is also Gaussian distributed, the mean vanishes, and its variance increases linearly with time t .

For a concrete numerical modelling of the CDS, only realisations of the stochastic process according to Eq. (2.30) are considered where R_{in} stays within predefined finite boundaries.

Describing the stellar pulsation, i.e. the piston movement requires as input parameter the period P and the velocity amplitude Δu or the intensity of the noise σ . The rest position of the piston at the inner boundary R_0 decisively influences the input of mechanical energy. The larger the distance of the piston from the photosphere, the higher is the input of mechanical energy. Waves steepen up to higher amplitude shocks and lead to increase levitation of matter into the wind generating zone. Result is a higher mass loss with lower terminal velocity (Holzer (1987)). The position has to be seen as an additional model input parameter.

Chapter 3

Analysis of dynamics

3.1 Diagnostic methods

The dynamics of (non-)linear systems may be described by means of different characteristics. One of the classical ways to characterise these dynamics is to compute the power spectrum based on the Fourier transform. This provides a profound physical understanding of the real system dynamics by detecting the various frequencies contained in a given signal. Another way is an examination by means of a deterministic approach e.g. to design the specific Poincaré maps to find domains of stability in the phase space.

This section describes the fundamental methods used for the study of CDS dynamics in this work. The basic Fourier transform equations as well as substantial properties in general are summarised. Subsequently the problems in discretising a function for computational analysis are discussed, followed by a short description of the algorithm used to compute the discrete Fourier Transform (DFT). In the last section the construction of Poincaré maps as a standard tool in general dynamical systems theory for the study of systems-properties is presented.

3.1.1 Fourier Transform

The Fourier transform (FT) defines a relationship between a signal e.g. in the time domain and its representation in the frequency domain. No information is created or lost in the process, so the original signal can be recovered by knowing the Fourier transform and vice versa. The Fourier transform of a signal is a continuous complex valued signal. It is capable of representing real valued or complex valued continuous time signals. The continuous Fourier transform of an arbitrary signal and its inverse are defined as follows:

$$\begin{aligned}
 H(f) &= \int_{-\infty}^{+\infty} h(t) e^{-2\pi i f t} dt \\
 h(t) &= \int_{-\infty}^{+\infty} H(f) e^{2\pi i f t} df .
 \end{aligned}
 \tag{3.1}$$

$H(f)$ ^a is the Fourier transform or spectrum, f the oscillatory frequency, and $h(t)$ the signal in time, where t represents the time. Note, the similarity between the transforms. It explains the duality between a signal and its spectrum. In some texts the Fourier transform is defined in another way, differing e.g. by factors 2π and -1 depending on the particular definition employed. These notational differences have some minor benefits and drawbacks, but they are all equivalent. This work writes the transforms in terms of the oscillation frequency f instead of angular frequency $\omega = 2\pi f$, because the factor of 2π can then be omitted e.g. when moving into discretely sampled data.

The Fourier transform has some interesting properties, which are an aid to understanding e.g. the shape of certain signals. Table 3.1 summarises some important properties, but it should not be taken as all-inclusive.

Table 3.1: Elementary properties of the Fourier transform

| | Time Domain | Frequency Domain |
|--------------------|--|---|
| Linearity | $ah(t) + bg(t)$ | $aH(f) + bG(f)$ |
| Time scaling | $h(at)$ | $\frac{1}{ a }H\left(\frac{f}{a}\right)$ |
| Frequency scaling | $\frac{1}{ b }h\left(\frac{t}{b}\right)$ | $H(bf)$ |
| Time shifting | $h(t - t_0)$ | $H(f) \exp(-2\pi i f t_0)$ |
| Frequency shifting | $h(t) \exp(2\pi i f_0 t)$ | $H(f - f_0)$ |
| Differentiation | $\frac{d^n}{dt^n}h(t)$ | $(2\pi i f)^n H(f)$ |
| Integration | $\int_{-\infty}^t h(\tau) d\tau$ | $\frac{1}{2\pi i f} H(f) + H(0)\delta(f)$ |
| Area | $\int_{-\infty}^{+\infty} h(t) dt$ | $H(0)$ |
| Value at Origin | $h(0)$ | $\int_{-\infty}^{+\infty} H(f) df$ |

^aA signal is often denoted with a small letter, and its Fourier transform or spectrum with a capital letter.

Symmetry of $h(t)$ in the time domain leads to relationships between $H(f)$ and $H(-f)$ in the frequency domain. The rules of symmetry are listed in Table 3.2.

Table 3.2: Correspondence between symmetries in the two domains

| | Time Domain | Frequency Domain |
|--------------------|-----------------|-------------------|
| Conjugate Symmetry | $h(t) \in \Re$ | $H(f) = H^*(-f)$ |
| | $h(t) \in \Im$ | $H(f) = -H^*(-f)$ |
| Even Symmetry | $h(t) = h(-t)$ | $H(f) = H(-f)$ |
| Odd Symmetry | $h(t) = -h(-t)$ | $H(f) = -H(-f)$ |

Convolution and correlation

By combining two functions $g(t)$ and $h(t)$ and their corresponding Fourier transforms $G(f)$ and $H(f)$, results in one of the most important relationships in the analysis of signals.

The *convolution*, denoted $g * h$ defined by the integral:

$$g(t) * h(t) \equiv \int_{-\infty}^{+\infty} g(\tau)h(t - \tau)d\tau \quad (3.2)$$

is a symmetric function in time, i.e. commutative $g * h = h * g$. The connection between the convolution of two functions $g(t)$ and $h(t)$ and their corresponding Fourier transforms $G(f)$ and $H(f)$ is called the *convolution theorem*:

$$\begin{aligned} g(t) * h(t) &\Leftrightarrow G(f)H(f) \\ h(t)g(t) &\Leftrightarrow H(f) * G(f) \end{aligned} \quad (3.3)$$

which states that convolving two functions in the time domain corresponds to multiplying their spectra in the Fourier domain, and vica versa. Note that multiplication is a much easier operation than convolution.

The *correlation* function between $g(t)$ and $h(t)$ is also a function of t , i.e. lies in the time domain. The integral:

$$\phi_{g,h}(t) \equiv \int_{+\infty}^{+\infty} g(\tau + t)h(\tau)d\tau \quad (3.4)$$

is called the *cross-correlation*, and $\phi_{g,h}(t)$ is the cross-correlation function of signals $g(t)$ and $h(t)$, which is not a commutative function, i.e. $\phi_{g,h}(t) = \phi_{h,g}(-t)$.

The corresponding Fourier transform is

$$\Phi_{g,h}(f) = G(f)H(-f) \stackrel{g,h \in \mathfrak{R}}{=} G(f)H^*(f) \quad (3.5)$$

Usually $g(t)$ and $h(t)$ are real functions. Then, the application of the conjugate symmetry (cf. with Table 3.2) yields the second relation in Eq. (3.5). A special relation, called the *autocorrelation*, refers to the correlation of a signal with itself, i.e. $g(t) = h(t)$. There exists a somewhat surprising and extremely important relationship between the autocorrelation and its Fourier transform, which is known as the *Wiener-Khinchin theorem*. The Fourier transform of the autocorrelation is related to spectral density:

$$\phi_{g,g}(t) \Leftrightarrow |G(f)|^2. \quad (3.6)$$

Parseval's theorem

The inner product of a continuous function with itself as introduced in the previous section has an important interpretation in many physical situations, namely the total amount of energy in a signal.

Parseval's theorem can be regarded as a formulation of the conservation of energy, stating that a signal contains a given amount of energy regardless of whether that energy is computed in the time domain or in the frequency domain.

The total power P in a signal is determined by:

$$P := \int_{-\infty}^{+\infty} |h(t)|^2 dt = \int_{-\infty}^{+\infty} |H(f)|^2 df. \quad (3.7)$$

If one is interested in the portion of a signal's power (energy per unit time) falling within a given frequency interval f to $f + df$, the power spectrum gives a plot of distribution. Of practical importance is the conjugate symmetry property (see Table 3.2). When $h(t)$ is real-valued, the spectrum at negative frequencies equals the complex conjugate of the spectrum at the corresponding positive frequencies. Consequently, only the positive frequency portion of the spectrum need to be plotted, also called the *one-sided power spectral density (PSD)*:

$$\begin{aligned} P_h(f) &= |H(f)|^2 + |H(-f)|^2 & 0 \leq f < \infty \\ &= 2|H(f)|^2 \end{aligned} \quad (3.8)$$

The total power is then just the integral $P_h(f)$ from $f = 0$ to $f = \infty$.

Discrete Fourier Transform

In computational studies it is not possible to analyse continuous functions $h(t)$, but instead a discrete list of measurements $h_k = h(k\Delta t)$ sampled at intervals in time Δt (sampling interval) with integer $k = 0, \dots, N - 1$ where N is the number of sampled values. This can be done by multiplying a continuous signal with a Dirac comb function $\sum_{k=-\infty}^{+\infty} \delta(t - k\Delta t)$. This multiplication “picks out” values but the result is still continuous-valued. If this signal is then discretised, i.e. converted into a sequence of length $T = k\Delta t$, and quantised along all dimensions it becomes a discrete signal. The result is the following discrete Fourier transform (DFT):

$$H_n := H(f_n) = \frac{1}{N} \sum_{k=0}^{N-1} h_k e^{-2\pi i n k / N} \quad n = -\frac{N}{2}, \dots, \frac{N}{2} - 1 \quad (3.9)$$

with the discrete frequencies:

$$f_n \equiv \frac{n}{N\Delta t} \quad (3.10)$$

A detailed mathematical derivation can be found in e.g. Brigham (1989).

Of course although the functions here are described as a complex series, real valued series can be represented by setting the imaginary part to zero.

Sampling and aliasing

According to the *Sampling Theorem*^b, a continuous signal must be discretely sampled with a value at least twice that of the highest frequency in the signal. More precisely, a continuous function $h(t)$ is completely reconstructed by samples every $\Delta t = 1/f_s$ (f_s is the sampling frequency), if the frequency spectrum $H(f)$ is zero for $f > f_s/2$, i.e. bandpassed. $f_s/2$ is called the *Nyquist critical frequency* f_c ^c and places the limit on the minimum sampling frequency when digitising a continuous signal. It is defined:

$$f_c \leq \frac{1}{2\Delta t} \leq \frac{f_s}{2} \quad (3.11)$$

For a continuous function that is not bandwidth-limited in frequency for less than the Nyquist critical frequency f_c , the power spectral density that lies outside of the frequency range $-f_c < f < f_c$ is then moved into this range. This phenomenon is called *aliasing* (see Fig. 3.1). There is no way to overcome aliasing other than to

^boften called “Shannon Sampling Theorem”, or in recent literature also WKS-Sampling-Theorem (Whittaker-Kotelnikow Shannon)

^cnamed after Harry Nyquist by Claude Elwood Shannon

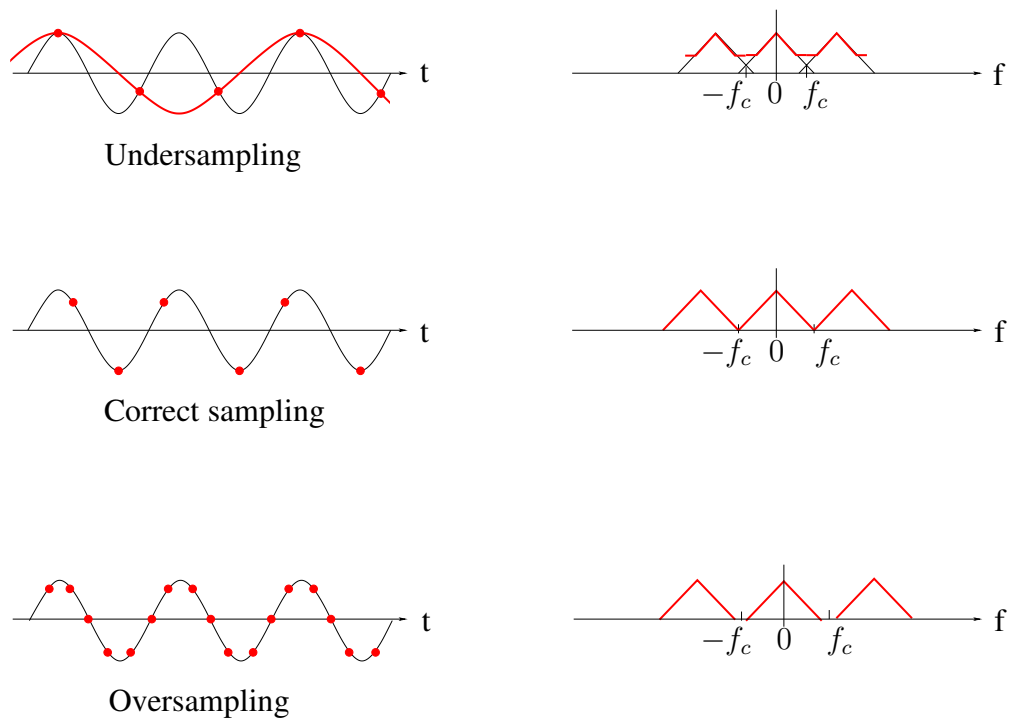


Figure 3.1: Influence of the sampling rate (red circles, left panel) on the frequency spectrum (red line, right panel).

know the bandwidth limit of a signal in advance and then to sample with sufficient density, so that the Nyquist frequency is higher than the bandwidth limit. On the other hand one can check the quality of the sampling rate. The power spectral density should tend towards zero for the Nyquist critical frequencies $\pm f_c$, otherwise one has a bad sampling rate Δt^{-1} (Fig. 3.1).

Spectral resolution

The level of detail or resolution in the frequency spectrum is indicated by the spectral resolution Δf :

$$\Delta f = \frac{1}{N\Delta t} \quad . \quad (3.12)$$

If the spectral resolution is too coarse, fine details in the spectrum may be lost. To resolve small detailed structures in the spectrum of a signal, one needs to ensure that $N\Delta t$ is large, i.e. one must sample the signal over a longer time. This can be achieved by either taking a large number of samples N , or by making the sampling interval Δt longer, or perhaps both. If the sampling interval is too long, however, aliasing of higher-frequency components of the signal may occur. On

the other hand, increasing the number of samples has the disadvantage of increasing the computing time to obtain the DFT and the amount of memory required to store the data during the processing. So one has to reach a reasonable compromise between computational time and the required accuracy of the analysis when choosing Δt .

Periodicity

In order to apply Fourier's theorem, the signal is assumed to be periodic, with a period equal to the sample length $T = N\Delta t$. In other words, the signal existing only during the time while it was being sampled, is assumed to consist of endless repetitions of the captured segment of the signal. So far, n is considered to vary from $-N/2$ to $N/2 - 1$ as k varies from 0 to $N - 1$. However, Eq. (3.9) is periodic in n with period N , that is:

$$\begin{aligned} H_{n+N} &= \frac{1}{N} \sum_{k=-\frac{N}{2}}^{\frac{N}{2}-1} e^{-\frac{2\pi i(n+N)k}{N}} h_k = \frac{1}{N} \sum_{k=-\frac{N}{2}}^{\frac{N}{2}-1} e^{-\frac{2\pi ink}{N}} \underbrace{e^{-\frac{2\pi iNk}{N}}}_{=1 \forall k \in \mathbb{N}_0} h_k \\ &= \frac{1}{N} \sum_{k=-\frac{N}{2}}^{\frac{N}{2}-1} e^{-\frac{2\pi ink}{N}} h_k = H_n \end{aligned} \quad (3.13)$$

Thus, if n is allowed to vary from 0 to $N - 1$ - which is a complete period - all the frequencies will be covered and n will vary in exact correspondence to k . Thus:

- $n = 0$ corresponds to the zero frequency component f_0 and yields the mean value of h_k 's

$$H_0 = \frac{1}{N} \sum_{k=0}^{N-1} e^{-\frac{2\pi ink}{N}} h_k = \frac{1}{N} \sum_{k=0}^{N-1} h_k \quad (3.14)$$

- $1 \leq n \leq \frac{N}{2} - 1$ corresponds to the frequencies $0 < f < f_c$,
- $\frac{N}{2} + 1 \leq n \leq N - 1$ corresponds to the frequencies $-f_c < f < 0$, and
- $n = N/2$ corresponds to both $-f_c$ and f_c .

Fast Fourier Transform

Since the fast Fourier Transform (FFT) algorithms are often applied to compute the DFT, these two abbreviations are used interchangeably, although there is a clear distinction. DFT refers to a mathematical transformation, regardless of how it is computed, while FFT refers to one of several efficient algorithms to compute the DFT and its inverse.

The FFT algorithm reduces the number of operations needed for N points from $\mathcal{O}(N^2)$ to $\mathcal{O}(N \log_2 N)$. The basic idea is to break up a transform of length N into two transforms of length $N/2$ using the identity sometimes called the Danielson-Lanczos lemma.

Danielson-Lanczos lemma

Lemma: The discrete Fourier transform of length N (where N is a power of 2) can be rewritten as the sum of two discrete Fourier transforms, each of length $N/2$. One is formed from the even-numbered points; the other from the odd-numbered points.

Proof:

$$\begin{aligned}
 {}^N H_n &=: \sum_{k=0}^{N-1} e^{-2\pi i n k / N} h_k \\
 &= \sum_{k=0}^{N/2-1} e^{-2\pi i n (2k) / N} h_{2k} + \sum_{k=0}^{N/2-1} e^{-2\pi i n (2k+1) / N} h_{2k+1} \\
 &= \sum_{k=0}^{N/2-1} e^{-2\pi i n k / (N/2)} h_{2k} + e^{-2\pi i n / N} \sum_{k=0}^{N/2-1} e^{-2\pi i n k / (N/2)} h_{2k+1} \\
 &= {}^{N/2} H_n^e + W_N^n \cdot {}^{N/2} H_n^o \quad \blacksquare
 \end{aligned} \tag{3.15}$$

where $e^{-2\pi i / N}$ is substituted by W_N . This procedure can be applied recursively to break up the $N/2$ even and odd points into their $N/4$ even and odd points. If N is a power of 2, this procedure breaks up the original transform into $\log_2 N$ transforms of length 1. Using the FT properties of periodicity and symmetry reduce the number of operations for the phase factor W_N^n , which is the reason for the enhanced efficiency of this algorithm.

Figure 3.2 demonstrates, graphically the above described procedure, for the case of $N = 8$ samples.

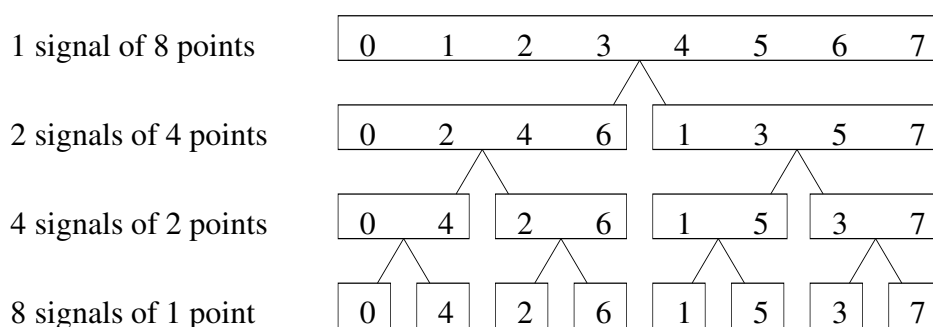


Figure 3.2: The FFT decomposition. An N point signal is decomposed into N signals each containing a signal point. Each stage uses an interlace decomposition separating the even and odd numbered samples.

Bitreversing

As can be seen in Fig. 3.2 the order of samples has changed. Table 3.3 shows how to rearrange the samples to get the right order. First the value of n in binary is produced. By reversing the patterns of 0's and 1's, back to front and reinterpreting as number n the right order is generated. This procedure does not require any additional computational effort.

Table 3.3: The FFT bit reversal sorting. The FFT time domain decomposition can be implemented by sorting the samples according to bit reversed order.

| Sample numbers in normal order | | | Sample numbers after bit reversal | |
|-----------------------------------|---------------|---|--------------------------------------|----------------|
| <i>Decimal</i> | <i>Binary</i> | | <i>Binary</i> | <i>Decimal</i> |
| 0 | 000 | ↔ | 000 | 0 |
| 1 | 001 | | 100 | 4 |
| 2 | 010 | | 010 | 2 |
| 3 | 011 | | 110 | 6 |
| 4 | 100 | | 001 | 1 |
| 5 | 101 | | 101 | 5 |
| 6 | 110 | | 011 | 3 |
| 7 | 111 | | 111 | 7 |

Fast Fourier transform algorithms generally fall into two classes: decimation in time and decimation in frequency. The Cooley-Tukey FFT algorithm (Cooley

and Tukey (1965)), which is used in this work, first rearranges the input elements in bit-reversed order then builds the output transform (decimation in time). The Sande-Tukey algorithm (Stoer and Bulirsch (1980)) first transforms then rearranges the output values (decimation in frequency).

In Appendix A the entire procedure is shown in detail for the case of $N = 8$ discrete samples.

3.1.2 Mapping

For dynamical systems having several degrees of freedom it is not very practical to discuss the orbital motion in a multi-dimensional phase space. A more appropriate way is to study the intersections of the trajectory with a plane in phase space. Systems of the form:

$$\frac{d}{dt}x(t) = F(x, t) \quad x \in \mathbb{R}^n \quad (3.16)$$

give rise to a map. Suppose $n = 3$, that is a 3D flow Γ . Instead of directly studying the flow in 3D, one considers its interaction with a plane (map), which is transverse to the flow in phase space. The intersection of the orbit with the plane reduces the dimension to $n - 1$. A map can be generated in at least two ways: by a *stroboscopic map* and by a *Poincaré map*. Although these maps do not contain the full dynamics of the systems, they are extremely useful for understanding some key properties of chaotic motion, e.g. about the “route to chaos”.

Stroboscopic map

For flows periodic in time it is convenient to create so called stroboscopic maps, which show the time trajectory at equally spaced, discrete times. In other words, the flow is sampled whenever $t = nT$ for $n \in \mathbb{N}_0$ (see Fig. 3.3). This kind of map can be constructed for any temporal interval.

Poincaré map

In autonomous systems i.e. no time-dependent terms in the equations, it may also be possible to define a Poincaré section and again reduce the phase space dimension by one. Here, the Poincaré section is defined not by a fixed time interval T , but by successive times when an orbit crosses a fixed surface in phase space. Surface means here a manifold of dimension one less than the phase space dimension.

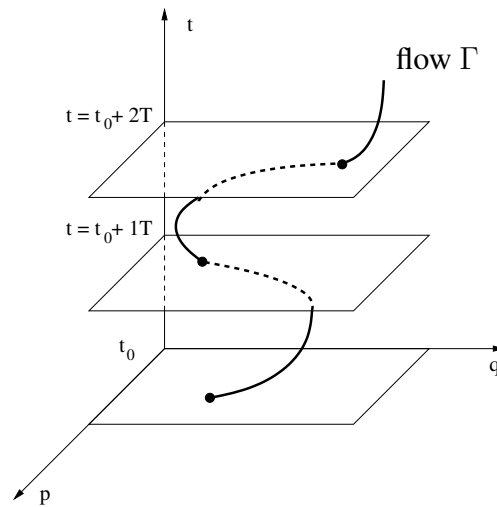


Figure 3.3: Construction of a stroboscopic map

The basic principle is that an n -th order continuous time system is replaced with an $(n - 1)$ -th order map. It is constructed by sampling the phase portrait stroboscopically. Its aim is to simplify the complicated system. Figure 3.4 shows how motions can be distinguished from each other. Periodic behaviour is a fixed point in Poincaré map. A quasi-periodic behaviour is a closed curve or points in Poincaré map, whereas distinct set of points indicate the chaos in Poincaré maps.

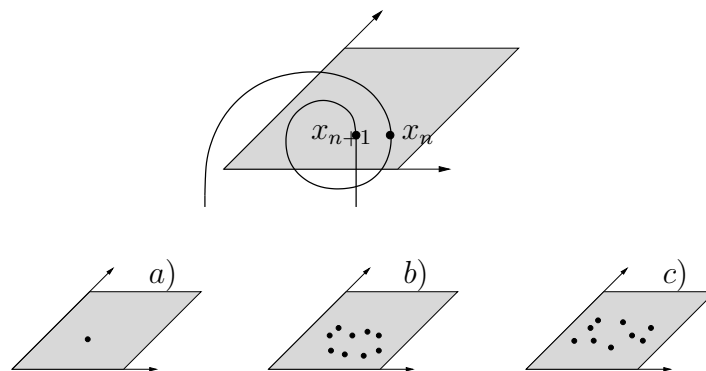


Figure 3.4: Behaviour of dynamic systems as seen in Poincaré maps: a) periodic, b) quasiperiodic and c) chaotic.

For more details of non-linear dynamics the reader is referred to Ott (2002) and Schuster & Just (2005), for example.

3.2 Principle procedure of the data analysis

3.2.1 Methodical details

In order to investigate and discuss the space-time evolution of the physical quantities of a CDS inferred by the numerical solution of the system of fundamental model equations by the FGSG-code, one can plot the radial structure of the shell in the Eulerian framework at one arbitrarily chosen instant time. In this way, one achieves a complete overall picture of the CDS.

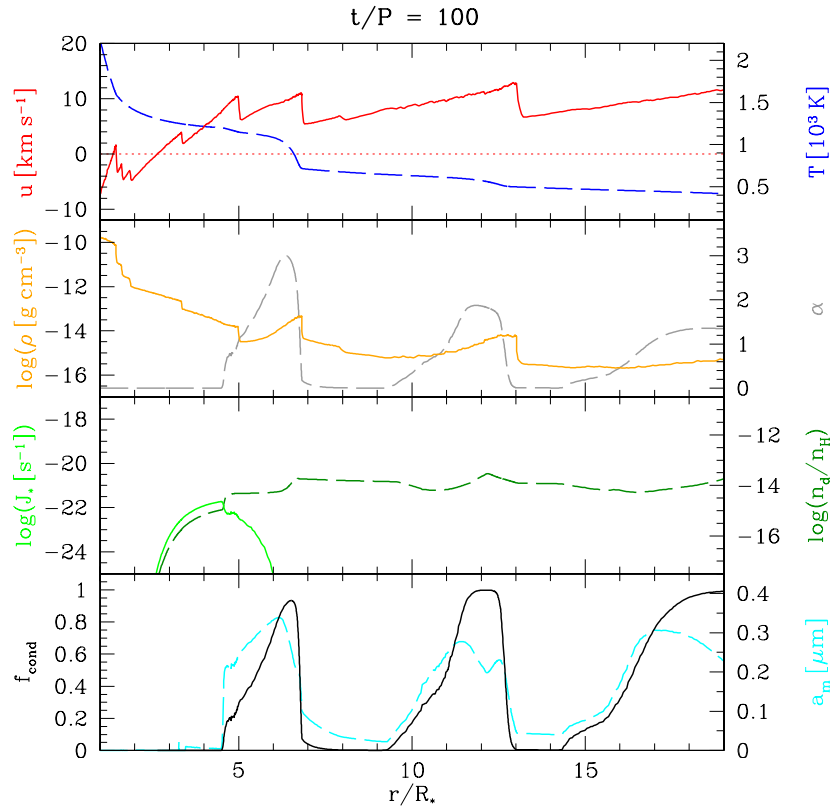


Figure 3.5: Snapshot of the fully developed radial shell structure of a CDS model

Figure 3.5 shows exemplarily the radial structures of some physical and chemical quantities describing a CDS such as:

upper panel: gas velocity u (solid line), and gas temperature T (dashed line),

second panel: the mass density ρ (solid line), and radiative acceleration on dust in units of the local gravitational deceleration α (dashed line),

third panel: stationary nucleation rate J_* (solid line), and the number of dust grains per H-atom n_d/n_H (dashed line),

lower panel: degree of condensation f_{cond} (solid line), and the mean particle radius a_m (dashed line),

The CDS is subjected to a Fourier transform. Since the gas velocity $u(r, t)$ of a CDS outflow is usually taken to be a tracer of (multi-) periodicity, it is presented a detailed analysis of the velocity structure. In order to do this, the time-dependent velocity $u(r, t)$, which was equidistantly sampled with an interval Δt over a time period of $t_{\text{max}} = 160\,000$ d, was transformed at each fixed radial position r for $1 R_* \leq r \leq 20 R_*$. The spatial resolution was chosen to be $\Delta r = 0.25 R_*$. The result is the overall power spectrum of a CDS as presented in Figure 3.6.

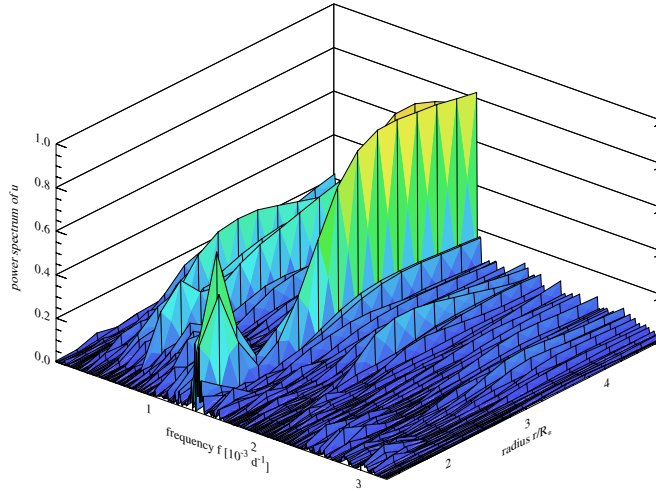


Figure 3.6: Overall velocity power spectrum of a CDS model

This is completed by the construction of maps. Since the dynamics in CDSs are strongly influenced by the presence of dust, the investigation focuses on the physical quantities necessary to provide favourable conditions for dust formation such as gas velocity u , gas density ρ , and temperature T . The stroboscopic maps were obtained by sampling the above-listed quantities with a time interval Δt chosen to be small compared with the excitation period P , i.e. $[u(n0.02P), \rho(n0.02P), T(n0.02P)]$ and the Poincaré maps were sampled at a constant phase angle ϕ of the stellar pulsation, i.e. after each period P : $[u(nP), \rho(nP), T(nP)]$

for $1 \leq n \leq \lfloor t_{max}/P \rfloor$, $n \in \mathbb{N}$ within the dust-forming zone. This is supplemented by the projection of the corresponding maps onto the $[u, \rho]$ -plane (Figure 3.7).

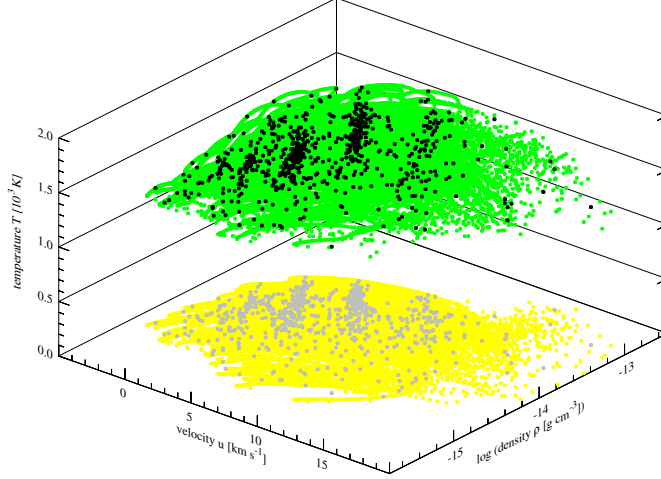


Figure 3.7: Stroboscopic map of the (u, ρ, T) -phase space (green), Poincaré map (black) and their projection onto the (u, ρ) plane (yellow and grey) of a CDS model.

Important parameters characterising stellar winds are the temporally averaged mass-loss rate $\langle \dot{M} \rangle$ and terminal velocity $\langle u_\infty \rangle$ for the gas. Both quantities together give the gas density $\langle \rho \rangle$ according to the *equation of continuity* $\dot{M} = 4\pi r^2 \rho u$. Thereby, the nomenclature $\langle x \rangle$ means averaging at a fixed outer radial position of $r = 25 R_*$ over a time interval T of at least one pulsation period P , i.e. $\langle x \rangle = 1/T \int_t^{t+T} x(t') dt'$. The dust can be typified through different properties like the degree of condensation f_{cond} , the dust-to-gas density ratio $\langle \rho_d / \rho_g \rangle$, and the mean grain radius a_m . Throughout this work, above-mentioned quantities will always be listed to describe specific CDSs.

3.2.2 Influence of numerics

To minimise the influence of the numerical scheme on the obtained results, a minimum grid resolution has to be chosen. The grid resolution is defined by a finite set of grid points N_{grid} distributed over the model domain, starting at an inner boundary R_0 and ending at an outer boundary R_{out} . In order to maintain a given resolution with ongoing dynamical calculations, the grid needs to be remapped, i.e. the insertion of grid points at R_{remap} every time t_{remap} where the width of

the Lagrangian zone has become too large. To study the influence of the resolution chosen upon the obtained results, calculations for adaptive grids with different numbers of grid points in the range of $N_{\text{grid}} = (1000 - 10000)$, outer grid boundary in the range of $R_{\text{out}} = (20 - 70) R_*$, grid redistribution time intervals $t_{\text{remap}} = (0 - 1) P$, and insertion region of the grid points $R_{\text{remap}} = (1.5 - 7.5) R_*$ has been performed.

In general, the numerical setup has only a minor influence on the CDS dynamics. Only some wind properties such as mass loss rate $\langle \dot{M} \rangle$ and outflow velocity $\langle u_\infty \rangle$ show small variations. For this reason in the following studies the setup is fixed to the parameter set: number of gridpoints $N_{\text{grid}} = 4097$, outer boundary $R_{\text{out}} = 40 R_*$, grid redistribution time interval $t_{\text{remap}} = 0.4 P$, and insertion region of the grid points $R_{\text{remap}} = 3.5 R_*$.

As was emphasised in Sect. 3.1.1, the choice of the sampling interval Δt strongly influences the resulting frequency spectra of the CDS. Since the maximum frequency contained in the signal is not known, aliasing cannot be avoided. When performing the FFT analysis, the overall model time determining the lowest frequency and the sampling interval Δt determining via the Nyquistfrequency f_c the highest resolved frequency need to be selected to be adequate for the task in hand.

In order to confirm the obtained frequencies the time interval of about $t_{\text{max}} = 160\,000$ d has been sampled with different sampling numbers in the range of $N = (128 - 1024)$ and sampling rates in the range of $\Delta t = (38 - 400)$ d. Some parameter combinations led to artificial oscillation modes (pseudo-frequencies) because of the interaction of the redistributed grid with the sampling rate (cf. Sandin (2008)). This implies that the optimal sampling parameter combination for any CDS-model needs an individual clarification.

3.3 Cooling behind shock waves

Shock waves pass periodically the CDS, where they dissipate energy and heat up the surrounding gas. The resulting gas temperature structure affects the dynamics of the CDS. The condensation of seed particles from the gas phase (nucleation) is very temperature sensitive and triggers the further evolution of the dust components. Due to the acceleration of the gas-dust mixture by the radiation pressure on dust grains it also influences the mass loss rate as well.

For this reason, this section discusses the influence of different thermal approaches on the dynamical CDS-structure. A reference model with the following fundamental parameters:

$$\begin{aligned}
 L_* &= 7.5 \cdot 10^3 L_\odot & P &= 388 \text{ d} \\
 M_* &= 1 M_\odot & \Delta u &= 1.0 \text{ km s}^{-1} \\
 T_* &= 2450 \text{ K} & R_0 &= 0.91 R_* \\
 C/O &= 1.5
 \end{aligned}$$

has been chosen and calculated with three scenarios, namely assuming isothermal, adiabatic and NLTE conditions as introduced in Sect. 2.1.2).

The models using an isothermal and adiabatic shock approach were calculated using the original FSGS-code, whereas the model with NLTE cooling was computed as described by Woitke (1997) and Schirrmacher (2003). The radiative transfer is treated according to Unno & Kondo (1976).

Figures 3.8 to 3.10 show the radial structures of some physical quantities describing a CDS, the corresponding power spectra of the gas velocity u as well as the stroboscopic maps of the (u, ρ, T) -phase space.

Isothermal approach

If the shock waves are treated in the isothermal limit case, it is assumed that the gas instantaneously relaxes to RE everywhere in the envelope, i.e. the resulting gas temperature T_g is equal to the radiative temperature T_{rad} obtained from the radiation transfer calculation. As seen in the radial structure of the CDS in Fig. 3.8, the temperature (uppermost panel) is cold enough $T \approx 1500 \text{ K}$ at high density (second panel) to provide favourable conditions for dust nucleation of amorphous carbon around $r \approx 2.5 R_*$ (third panel). The spectrum clearly shows the piston frequency $f_p = 2.58 \cdot 10^{-3} \text{ d}^{-1}$ and some of its harmonics at the inner edge of the CDS at $r = (1 - 2) R_*$ as the dominant frequency. As the dust nucleation sets in these frequencies diminish and the frequency $f_{\text{CDS}} = 0.81 \cdot 10^{-3} \text{ d}^{-1}$ dominates the dynamics. The phase space is closed and shows the variation of velocity and density over a broad range.

Adiabatic approach

In the case of an adiabatic treatment of the shock the gas is not able to lose energy by radiation, i.e. $Q_{\text{rad}} = 0$. It can only cool by working during expansion Q_{ad} . The gas needs a large time for cooling to provide favourable conditions for dust nucleation, which is not sufficiently low at less than about $r \approx 10 R_*$ as can be seen in Fig. 3.9 uppermost panel. Once the dust is formed the radiation pressure on it accelerates (second panel) the matter but only up to a lower final velocity than is observed (first panel). Due to the extreme sensitivity of the nucleation rate

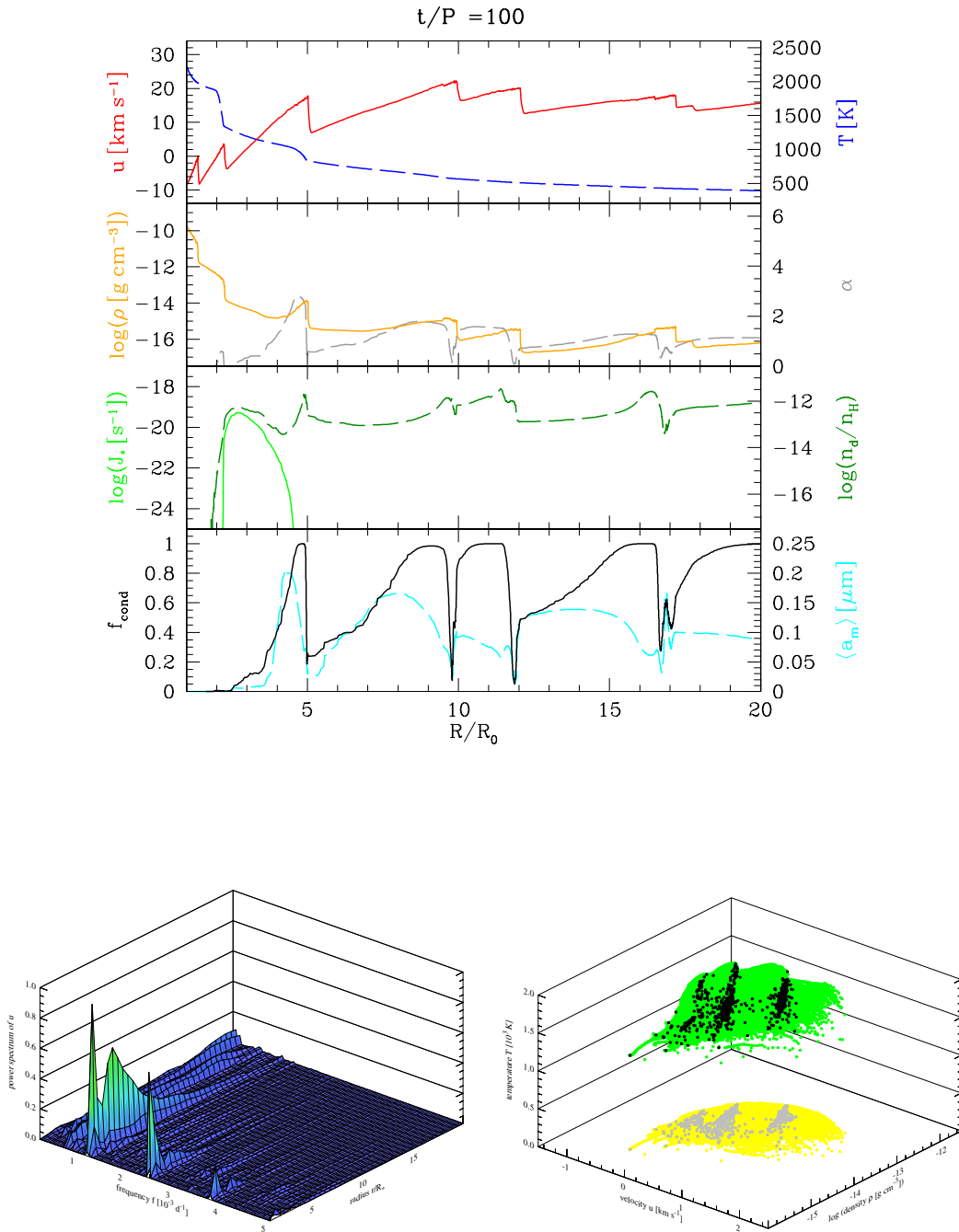


Figure 3.8: Snapshot of the radial shell structure (upper four panels), normalised power spectrum of velocity u (left lower panel) and stroboscopic map of the (u, ρ, T) -phase space (right lower panel) for the reference model in the case of an isothermal shock.

on the temperature fluctuations the nucleation rate appears as a conglomerate of several spikes rather one broad peak as in the models in the limit case of isothermal shocks (third panel). No onion-like shell structure has developed. The shock frequency $f_p = 2.58 \cdot 10^{-3} \text{ d}^{-1}$ is the predominant frequency in the spectrum. The (v, ρ, T) phase space is very restrictive in velocity and density and returns the hydrodynamic situation of the CDS.

Non-LTE approach

The post shock gas is composed of various atoms, molecules, ions and electrons. Such a gas radiates by a variety of processes, which are describable by cooling functions (see Sect. 2.1.2). As can be seen in Fig. 3.10 the temperature structure is very similar to that of the isothermal limit case (uppermost panel). The spectrum is dominated by the shock frequency $f_p = 2.58 \cdot 10^{-3} \text{ d}^{-1}$ at the inner edge, which is replaced by the frequency $f_{\text{CDS}} = 0.81 \cdot 10^{-3} \text{ d}^{-1}$ with onset of the dust nucleation at $r \approx 2.5 R_*$ (third panel). The radial structure as well as the spectrum and the stroboscopic map are very similar to that of the isothermal limit case.

Table 3.4 summarises some global quantities of the fully evolved reference CDS calculated with the three different thermal approaches of the radiating shock waves.

Table 3.4: Resultant quantities of the reference CDS, such as frequencies f_{CDS} and temporally averaged quantities such as mass loss rate $\langle \dot{M} \rangle$, outflow velocity $\langle u_\infty \rangle$ and dust-to-gas mass ratio $\langle \rho_d / \rho_g \rangle$ with different treatment of the radiating shock waves. Values shown in boldface indicate the strongest mode and underlined values represent the frequency of the stellar pulsation.

| Cooling | f_{CDS} | | $\langle \dot{M} \rangle$ | $\langle u_\infty \rangle$ | $\langle \rho_d / \rho_g \rangle$ | |
|------------|----------------------------|------|-----------------------------|----------------------------|-----------------------------------|---------------------|
| | (10^{-3} d^{-1}) | | $(M_\odot \text{ yr}^{-1})$ | (km s^{-1}) | | |
| isothermal | 0.81 | 1.27 | <u>2.58</u> | $1.3 \cdot 10^{-5}$ | 16.4 | $2.4 \cdot 10^{-3}$ |
| adiabatic | - | - | <u>2.58</u> | $7.2 \cdot 10^{-5}$ | 7.5 | $2.7 \cdot 10^{-3}$ |
| non-LTE | 0.81* | - | <u>2.58</u> | $1.2 \cdot 10^{-5}$ | 14.7 | $2.5 \cdot 10^{-3}$ |

*Maximum of a nearly normal distributed power spectrum in the frequency interval $[0.00075 \text{ d}^{-1} \leq f \leq 0.00087 \text{ d}^{-1}]$

Comparing the results one finds: Due to the radial structure of the gas temperature in the adiabatic limit case the dust formation is not so effective compared to the isothermal limit case and thus the outflow is accelerated to a lower velocity for the former. In the case of NLTE the temperature structure is very similar to

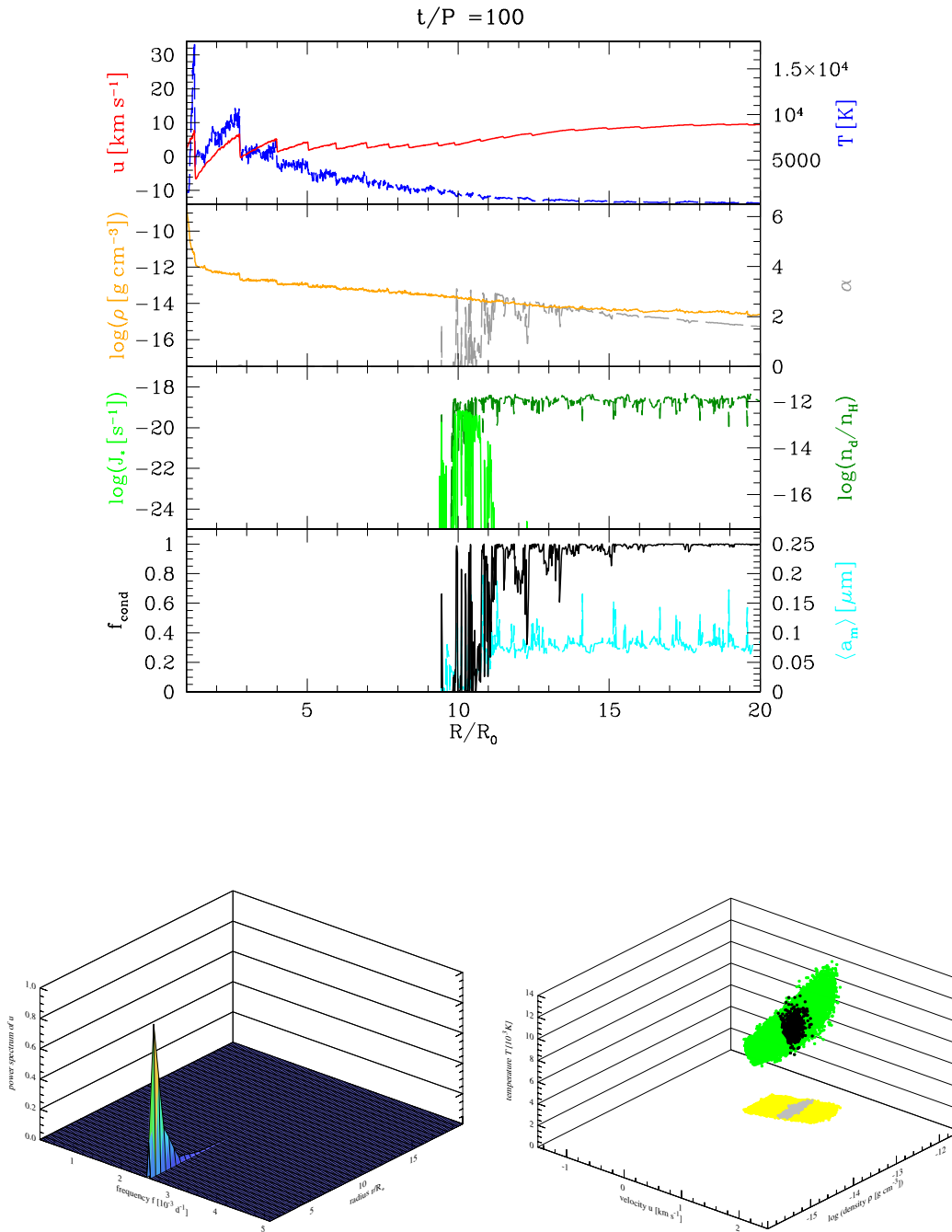


Figure 3.9: Same as Fig. 3.8 but in the case of an adiabatic shock.

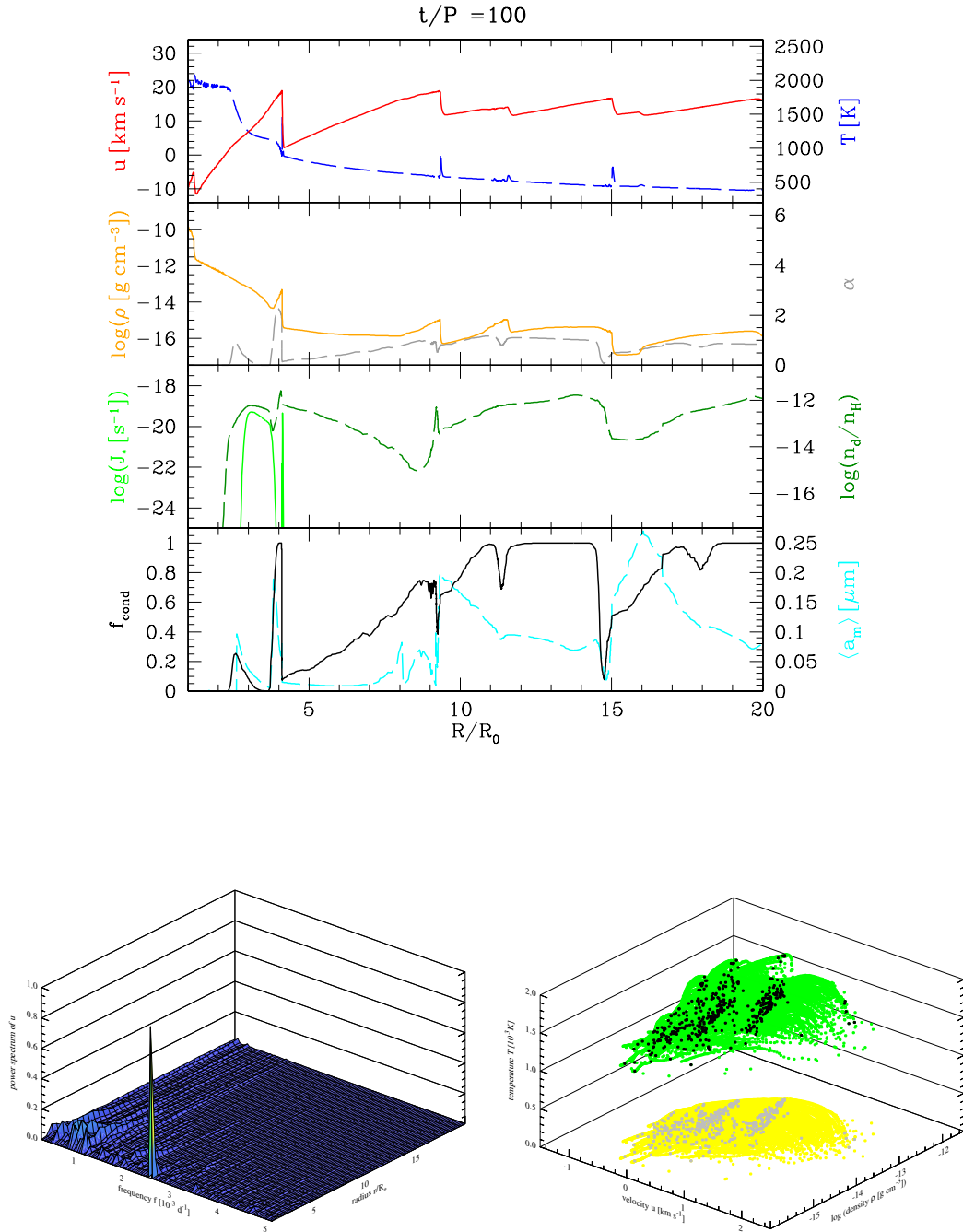


Figure 3.10: Same as Fig. 3.8 but in the case of a non-LTE shock

that of the isothermal limit case. The power spectra as well as the maps show similar structures. The assumption of an isothermal shock does not seem to affect severely the principle dynamical behaviour in the inner part of a CDS. For this reason the adaption of an isothermal shock is considered to be an acceptable simplification with regard to the investigation of the dynamical behaviour of a CDS. Therefore, the isothermal approximation is used throughout this work, unless otherwise stated.

Chapter 4

Dynamics of CDSs around high luminous AGB stars

4.1 Exterior κ -mechanism

Initial work of Fleischer et al. (1995) which was subsequently confirmed by Höfner et al. (1996), demonstrated that an instability caused by the formation of dust called the exterior κ -mechanism can lead to self-induced oscillations of the CDS. This instability is controlled by the strong non-local feedback of newly formed dust that influences the temperature and dynamics of the circumstellar matter via radiative transfer effects. The first dust grains start to form in a specific temperature and density regime (dust forming window) of the circumstellar shell, where their subsequent rapid growth strongly increases the opacity in the dust-forming region. This process affects the dusty shell in two ways. Firstly, on the one hand, radiative momentum is transferred effectively to the dust component and the gas is consequently accelerated in a mass-loss wind via frictional coupling. Secondly, on the other hand, the recently formed grains absorb the stellar radiation very effectively. Isotropically re-emitted mainly in the infrared, it produces a pronounced heating of the material inside the dust layer. The higher temperature due to this “backwarming” not only prevents further nucleation of dust grains inside the dust shell, but also leads to a slight increase in the pressure of the CDS and a subsequent generation of small-amplitude waves in the region above the stellar atmosphere. Because of the density gradient in the shell, these subsonic disturbances steepen into shock fronts, which propagate outward leading to substantial mass-loss. Thereby, the dust density is diluted, producing a far lower opacity. Consequently, the stellar radiation is no longer absorbed effectively. The resulting decrease in temperature initiates a new cycle of dust formation and growth. The process just described, known as the exterior κ -mechanism is a periodical

phenomenon and its timescale τ_κ is the characteristic or eigenperiod P_κ of the atmosphere, which is inherent to the dust-forming system. It depends of course on stellar parameters such as the abundance ratio of carbon to oxygen C/O or the stellar luminosity L_* . Extremely high luminosities and low temperatures are needed to sustain the oscillations of the CDS if they are to be driven purely by the exterior κ -mechanism.

4.2 The CDS as oscillatory system

The exterior κ -mechanism is only able to sustain an oscillation of a CDS for sufficiently high stellar luminosities L_* if one assume no input of energy and momentum from an underlying pulsating stellar atmosphere.

Figure 4.1 shows a snapshot of the radial structure of the fully developed circumstellar dust shell caused solely by the exterior κ -mechanism for a modelled example, subsequently called model A, with the parameters:

$$\begin{aligned} L_* &= 3 \cdot 10^4 L_\odot \\ M_* &= 1 M_\odot \\ T_* &= 2450 \text{ K} \\ C/O &= 1.25 \\ R_0 &= 0.82 R_* \end{aligned}$$

The dust-induced layered shell-structure can be seen for some characteristic hydrodynamical quantities, and quantities describing the dust complex.

The density gradient of the initial, hydrostatic structure of the high-luminosity model is gradual enough, i.e., the density scale height is sufficiently high to allow dust formation in the initial phase. A subsequent effective growth phase and radiation pressure acting on the newly formed dust grains both lead to the development of an outflow even without the additional input of mechanical energy. This is the onset of the instability solely caused by dust formation (exterior κ -mechanism). Due to the backwarming effect of the dust layer, the temperature below the shock front at $r \approx 2.5$ times the stellar radius R_* increases. Consequently, this leads to a slight increase in pressure in the innermost region, and the subsequent generation of small-amplitude waves. The subsonic disturbances steepen because of the density gradient in the innermost region. The newly formed shock front travels outward and finally compresses the grains contained in the dust-forming region, thereby triggering the dust growth. The entire process starts again and results in a periodic outflow as seen in Fig. 4.1.

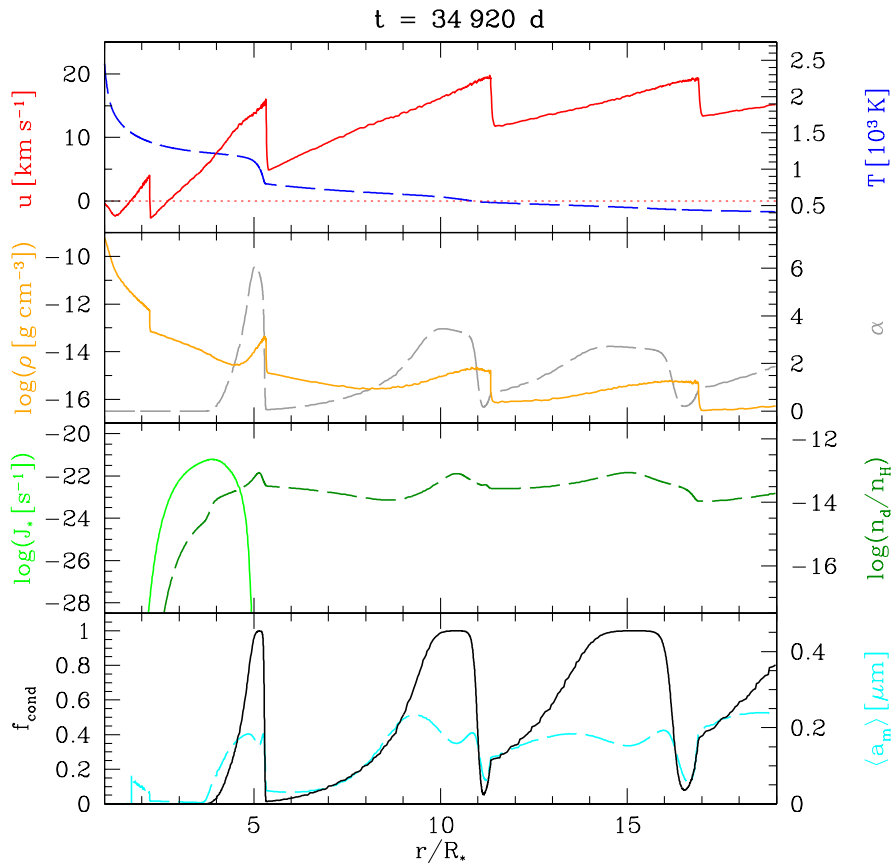


Figure 4.1: Self-induced radial structure of the model A. *Upper panel:* gas velocity u (solid line), gas temperature T (dashed line), *second panel:* mass density ρ (solid line), radiative acceleration on dust in units of the local gravitational deceleration α (dashed line), *third panel:* stationary nucleation rate J_* (solid line), number of dust grains per H-atom n_d/n_H (dashed line), *lower panel:* degree of condensation f_{cond} (solid line) and mean particle radius $\langle a_m \rangle$ (dashed line).

Figure 4.2 depicts the frequency behaviour of the self-sustaining oscillation for the representative CDS as obtain by a Fourier analysis. It should be noted that there is no internal pulsation of the star. The normalised power spectrum of the

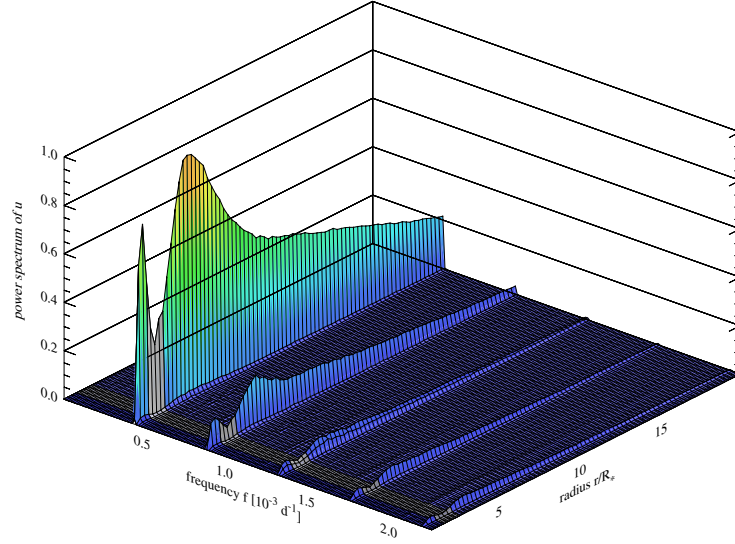


Figure 4.2: Normalised power spectrum of the radial gas velocity u for a range of well-defined frequencies which are exclusively induced by the exterior κ -mechanism. The position of the dust formation zone in the envelope is high lighted.

radial gas velocity u is shown as a function of the radial coordinate r . The eigenfrequency $f_\kappa = 0.41 \cdot 10^{-3} \text{ d}^{-1}$ and three of its overtones characterised by a monotonic decrease in strength with increasing frequency can be clearly identified. The amplitude of the eigenmode shows a strong dependence on the distance from the star. The minima at $r = 2.5 R_*$ clearly evident for each eigenmode are particularly remarkable. A comparison with the radial trajectory in Fig. 4.1 shows that the position of these frequency-minima coincides with the dust nucleation zone located at $(2 - 3) R_*$. This suggests that the dust is responsible for creating these characteristic frequencies of the dust shell. Shortly below and beyond the rather narrow nucleation zone (marked light grey) these frequencies peak, according to the backwards-travelling dilution wave and the forwards-travelling compression wave.

The fundamental eigenperiod P_κ is determined by the characteristic timescale of the coupled system of dust formation, hydrodynamics, and thermodynamics within the dust-forming zone and is simply given by $P_\kappa = 1/f_\kappa \approx 2450 \text{ d}$.

Lagrangian zones

Figure 4.3 exhibits the temporal evolution of the radial position $r(t)$ of some Lagrangian zones originating at various heights in the stellar atmosphere. Since there is no pulsation of the star, the innermost zone is static at $R_0 = 0.82 R_*$. Nevertheless, the atmosphere shows an oscillation pattern. The upper zones move sinusoidally and elements beyond a critical point at $r(t) \approx 2.25 R_*$ leave the atmosphere. At this radius dust formation occurs. The radiation pressure on the newly formed dust drives the material outwards and generates the wind. The backwards-travelling wave induces oscillations in the upper atmosphere. The CDE is clearly divided into two distinct zones: the levitated layers at the bottom and the wind region on top.

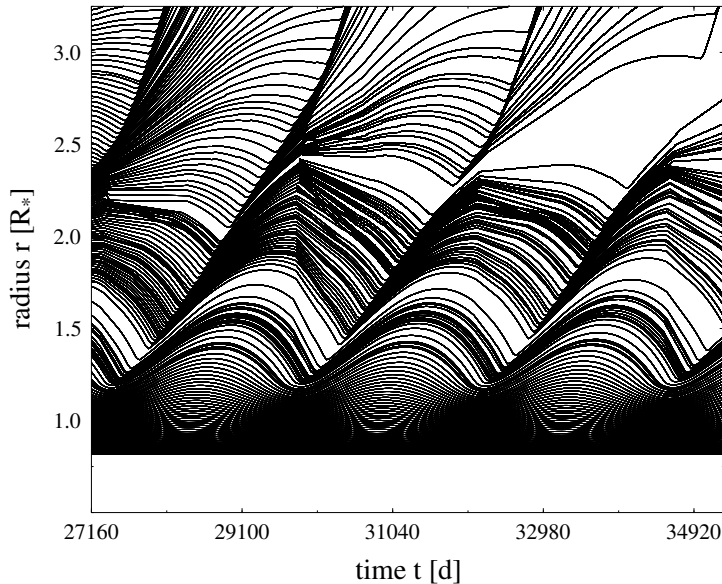


Figure 4.3: Temporal behaviour of Lagrangian zones in the outer atmosphere and wind of an LPV for the case without internal pulsation.

4.3 Periodically excited CDS

The identification of an eigenmode of the dust-forming circumstellar shell raises the question of how its related oscillatory behaviour interacts with an additional excitation caused by the internal κ -mechanism. For this purpose, the response

of the above-defined model was studied for a series of sinusoidal variations with different periods P and velocity amplitudes Δu at the inner boundary describing the stellar pulsation.

Since the dynamics of CDSs are basically controlled by the dust, the investigations are focused in particular on the dust nucleation zone, which is usually located around $r \approx (2 - 4) R_*$. According to the representative model structure (cf. Fig. 4.1, third panel), it is located at $r = 2.5 R_*$.

4.3.1 Excitation period

A linear system driven by an external periodic force will attempt to follow the applied force and hence oscillates with the applied frequency after a short, transient behaviour. This situation differs significantly from that of a nonlinear system such as the CDS. Depending on the strength of its nonlinearity, the system shows a periodic, quasi-periodic, or chaotic behaviour.

The dependence of the oscillation frequency f_{CDS} of the shell in the dust nucleation zone on the excitation period P is depicted in Fig. 4.4, which shows the ratio f_{CDS}/f_κ with f_κ being the CDS-eigenfrequency for various excitation periods of constant velocity amplitude $\Delta u = 1 \text{ km s}^{-1}$. Table 4.1 listed the plotted frequencies in detail. Three different regimes can be identified.

- **Eigenmode dominated regime**

For an excitation period of below approximately $P = 1500 \text{ d}$, the dynamics of the system is determined by the exterior κ -effect. The fundamental mode and its overtones can be clearly seen. As P increases, these are shifted towards lower frequencies, become weaker in strength, and eventually vanish when their frequencies reach the corresponding harmonic of the excitation frequency $f_p = 1/P$.

- **Pulsation dominated regime**

For $P > 2300 \text{ d}$, the CDS is dominated by the period of the stellar pulsation. Exclusively the stellar pulsation frequency and its harmonics are the dominant frequencies.

- **Irregular regime**

In-between the two above-mentioned regimes, i.e. shaded region, the behaviour of the system becomes irregular. However, some dominant frequencies can be identified. The stellar pulsation appears to become more influential with increasing P . For $P = 1500 \text{ d}$, the pulsation frequency

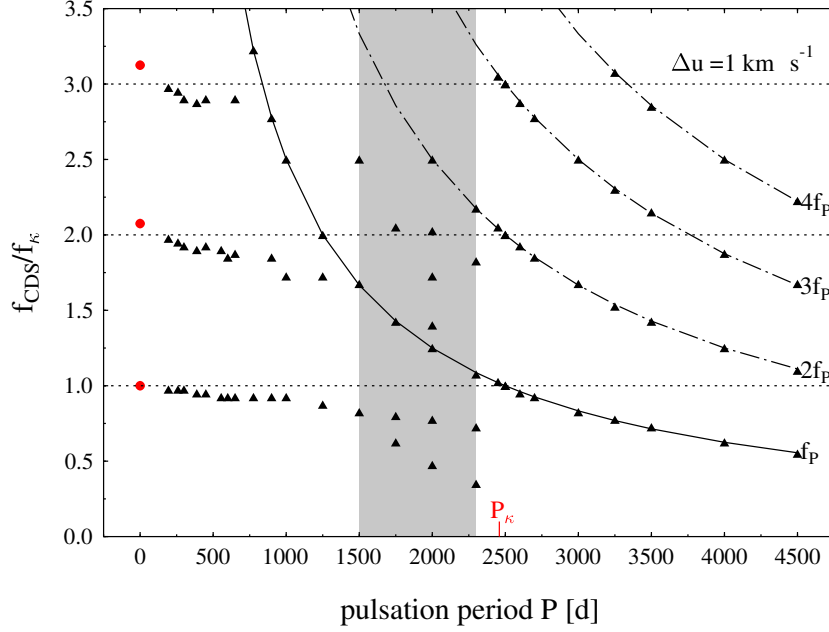


Figure 4.4: Most dominant frequencies of a CDS f_{CDS} related to its fundamental eigenfrequency $f_{\kappa} = 0.41 \cdot 10^{-3} \text{ d}^{-1}$ (triangles) excited with various pulsation periods P near the dust nucleation zone $r = 2.5 R_{*}$. The set of CDS-eigenmodes is depicted by circles, the eigenperiod is labelled with P_{κ} . The excitation frequencies (solid line) and their harmonics (dash-dotted lines), relative to f_{κ} , are also shown. The irregular regime (marked in grey) separates the eigenmode dominated regime (left) from the pulsation dominated regime (right).

coincidences with the first harmonic of the shell-eigenfrequency. Furthermore, it is remarkable that the fundamental mode exhibits a bifurcation at $P = 1750 \text{ d}$. Both branches are clearly distinguishable up to $P \approx 2300 \text{ d}$, above which the system favours stellar pulsation.

When pulsation is switched on at the inner boundary, the resulting input of mechanical energy and momentum introduces a new timescale into the system. In combination with the shocks already generated by the exterior κ -effect, the pulsation causes a further compression of the material to initiate dust growth. The radiation pressure acts on the newly formed dust and by means of the close momentum coupling between dust and gas, the two-component medium is accelerated outwards. With increasing excitation period P , the additional input of energy and momentum becomes more significant. Close to the resonance period P_{κ} , one observes a maximum transfer of energy, i.e., maximum amplitude.

This leads to an enhanced density in the dust forming region. Consequently, the model results implied that the stellar wind becomes far more massive and the mass-loss rate changes from $\langle \dot{M} \rangle = 9.4 \cdot 10^{-5} M_{\odot} \text{ yr}^{-1}$ for the undisturbed CDS, to $\langle \dot{M} \rangle = 3.8 \cdot 10^{-4} M_{\odot} \text{ yr}^{-1}$ for the resonance situation. In contrast, the final outflow velocity remains almost constant at $\langle u_{\infty} \rangle \approx 17 \text{ km s}^{-1}$ compared to $\langle u_{\infty} \rangle \approx 15.6 \text{ km s}^{-1}$ (cf. Table 4.1). As the wind becomes more intense, the periodic depletion in dust-forming material also increases and it takes more time to enrich the nucleation zone again. As a consequence, the eigenperiod becomes longer until the system finally becomes enslaved by the movement of the piston.

Resonance phenomenon

Now the analysis of the CDS is extended by using established diagnostic techniques of nonlinear dynamics. For a fixed position within the dust-forming zone, the orbit in phase space is projected onto the (u, ρ, T) plane by choosing a time interval Δt that is short relative to the excitation period P . For a system at a constant phase angle, i.e., after each period P , one obtains a special kind of stroboscopic map called a Poincaré map.

Figure 4.5 shows power spectra and stroboscopic maps of the CDS for various periods $P = (388 \text{ d}, 555 \text{ d}, 900 \text{ d})$ but with constant excitation-velocity amplitude $\Delta u = 1 \text{ km s}^{-1}$. The different spectra were normalised to their actual strongest mode.

The stroboscopic maps in the lower panels of Fig. 4.5 indicate that the oscillation of the CDS synchronises with the excitation period to some extent. It can be seen that the system for a constant phase angle (black dots) tends to stay inside a finite number of clearly demarcated stripes. In a similar way to the orbital resonance in celestial mechanics, two integers i and j can be found by fulfilling the condition $iP = jP_{\text{CDS}}$. After i periods P , the system approximately recaptures the same physical state, illustrated by one strip in the Poincaré map (marked with arrow). The number of stripes m increases with decreasing period P and is roughly given by rounding $i/j = P_{\text{CDS}}/P$ to the nearest integer.

For $P = 388 \text{ d}$ and $\Delta u = 1 \text{ km s}^{-1}$, for example, one finds that $i = 27$. This means that the system passes through the same state every $27 \times 388 \text{ d}$. Under the assumption $j = 4$, this corresponds to $P_{\text{CDS}} = 2619 \text{ d}$, which is confirmed to be $P_{\text{CDS}}(\text{FT}) = 2632 \text{ d}$ by a Fourier analysis of the temporal variation in the gas velocity u . The eigenmodes of the dust shell still determine the dynamics of the entire system. Due to this synchronisation, the response period P_{CDS} of the shell becomes only slightly longer than the period P_{κ} of the undisturbed system. Table 4.1 summarises the results for a series of excitation periods P by giving the resonance integers i , j , m , and P_{CDS} and the most dominant periods $P_{\text{CDS}}(\text{FT})$

Table 4.1: Resonance integers i, j, m and resulting oscillation period P_{CDS} in comparison to the period $P_{\text{CDS}}(\text{FT})$ from the FT as well as the most dominant frequencies f_{CDS} and temporally averaged quantities such as mass loss $\langle \dot{M} \rangle$, outflow velocity $\langle u_{\infty} \rangle$ and dust-to-gas ratio $\langle \rho_{\text{d}}/\rho_{\text{g}} \rangle$ of a CDS disturbed by different excitation periods P with constant velocity amplitude $\Delta u = 1 \text{ km s}^{-1}$.

| P (d) | i | j | m | P_{CDS} (d) | $P_{\text{CDS}}(\text{FT})$ (d) | f_{CDS} (10^{-3} d^{-1}) | | $\langle \dot{M} \rangle$ ($M_{\odot} \text{ yr}^{-1}$) | $\langle u_{\infty} \rangle$ (km s^{-1}) | $\langle \rho_{\text{d}}/\rho_{\text{g}} \rangle$ | |
|------------|-----|-----|-----|-------------------------|------------------------------------|--|-------------|--|--|---|---------------------|
| 0 | | | | | | 0.41 | 0.83 | 1.24 | $9.6 \cdot 10^{-5}$ | 17.3 | $1.2 \cdot 10^{-3}$ |
| 194 | 13 | 1 | 13 | 2522 | 2564 | 0.39 | 0.79 | 1.19 | $9.8 \cdot 10^{-5}$ | 17.3 | $1.3 \cdot 10^{-3}$ |
| 259 | 10 | 1 | 10 | 2590 | 2564 | 0.39 | 0.78 | 1.18 | $9.8 \cdot 10^{-5}$ | 17.3 | $1.2 \cdot 10^{-3}$ |
| 300 | | | | | | 0.39 | 0.77 | 1.16 | $1.0 \cdot 10^{-4}$ | 17.1 | $1.2 \cdot 10^{-3}$ |
| 388 | 27 | 4 | 7 | 2619 | 2632 | 0.38 | 0.76 | 1.15 | $1.1 \cdot 10^{-4}$ | 17.1 | $1.2 \cdot 10^{-3}$ |
| 450 | 23 | 4 | 6 | 2588 | 2632 | 0.38 | 0.77 | 1.16 | $1.1 \cdot 10^{-4}$ | 16.7 | $1.2 \cdot 10^{-3}$ |
| 555 | 5 | 1 | 5 | 2775 | 2703 | 0.37 | 0.76 | - | $1.4 \cdot 10^{-4}$ | 16.9 | $1.2 \cdot 10^{-3}$ |
| 600 | 9 | 2 | 5 | 2700 | 2703 | 0.37 | 0.74 | - | $1.3 \cdot 10^{-4}$ | 16.4 | $1.1 \cdot 10^{-3}$ |
| 650 | | | | | | 0.37 | 0.75 | 1.16 | $1.4 \cdot 10^{-4}$ | 16.7 | $1.2 \cdot 10^{-3}$ |
| 776 | 7 | 2 | 4 | 2716 | 2703 | 0.37 | - | <u>1.29</u> | $1.2 \cdot 10^{-4}$ | 16.8 | $1.1 \cdot 10^{-3}$ |
| 900 | 3 | 1 | 3 | 2700 | 2703 | 0.37 | 0.74 | <u>1.11</u> | $1.1 \cdot 10^{-4}$ | 17.0 | $1.2 \cdot 10^{-3}$ |
| 1000 | | | | | | 0.37 | 0.69 | <u>1.00</u> | $1.5 \cdot 10^{-4}$ | 16.4 | $1.1 \cdot 10^{-3}$ |
| 1250 | | | | | | 0.35 | 0.69 | 0.80 | $2.0 \cdot 10^{-4}$ | 15.8 | $1.1 \cdot 10^{-3}$ |
| 1500 | 2 | 1 | 2 | 3000 | 3030 | 0.33 | <u>0.67</u> | 1.00 | $3.0 \cdot 10^{-4}$ | 15.7 | $1.3 \cdot 10^{-3}$ |
| 1750 | | | | | | 0.32 | 0.57 | 0.82 | $2.9 \cdot 10^{-4}$ | 15.4 | $1.3 \cdot 10^{-3}$ |
| 2000 | | | | | | 0.19 | 0.81 | 1.00 | $3.8 \cdot 10^{-4}$ | 15.6 | $1.2 \cdot 10^{-3}$ |
| 2300 | | | | | | 0.14 | <u>0.43</u> | 0.87 | $3.6 \cdot 10^{-4}$ | 15.0 | $1.2 \cdot 10^{-3}$ |
| 2450 | | | | | | 0.41 | 0.82 | 1.63 | $3.4 \cdot 10^{-4}$ | 16.8 | $1.3 \cdot 10^{-3}$ |
| 2500 | | | | | | 0.40 | 0.80 | 1.20 | $2.7 \cdot 10^{-4}$ | 16.4 | $1.4 \cdot 10^{-3}$ |
| 2600 | | | | | | <u>0.38</u> | 0.77 | 1.15 | $3.0 \cdot 10^{-4}$ | 16.6 | $1.4 \cdot 10^{-3}$ |
| 2700 | | | | | | 0.37 | 0.74 | 1.11 | $3.1 \cdot 10^{-4}$ | 16.6 | $1.4 \cdot 10^{-3}$ |
| 3000 | | | | | | 0.33 | 0.67 | 1.00 | $3.5 \cdot 10^{-4}$ | 16.9 | $1.3 \cdot 10^{-3}$ |
| 3250 | | | | | | 0.31 | 0.61 | 0.92 | $3.6 \cdot 10^{-4}$ | 16.0 | $1.3 \cdot 10^{-3}$ |
| 3500 | | | | | | <u>0.29</u> | 0.57 | 0.86 | $3.5 \cdot 10^{-4}$ | 15.6 | $1.3 \cdot 10^{-3}$ |
| 4000 | | | | | | 0.25 | 0.50 | 0.75 | $2.1 \cdot 10^{-4}$ | 14.3 | $1.2 \cdot 10^{-3}$ |
| 4500 | | | | | | 0.22 | 0.44 | 0.67 | $2.5 \cdot 10^{-4}$ | 14.7 | $0.9 \cdot 10^{-3}$ |

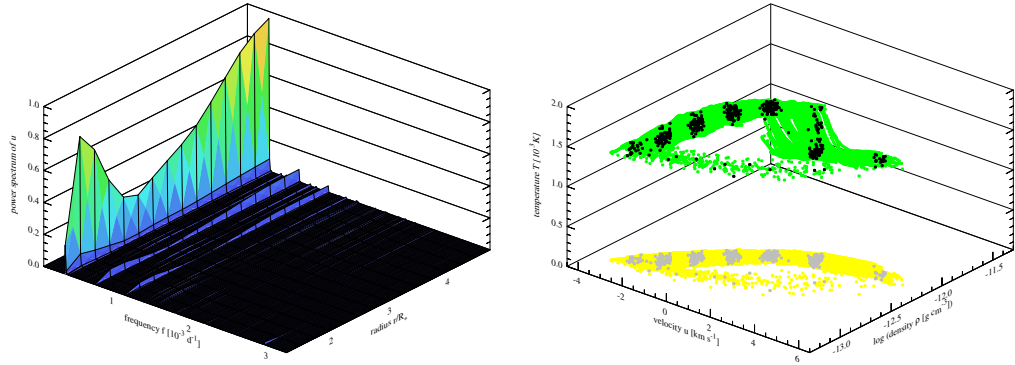
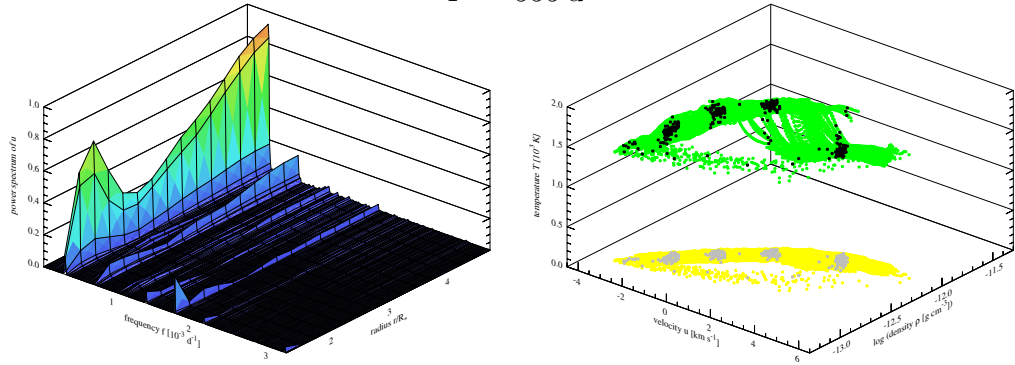
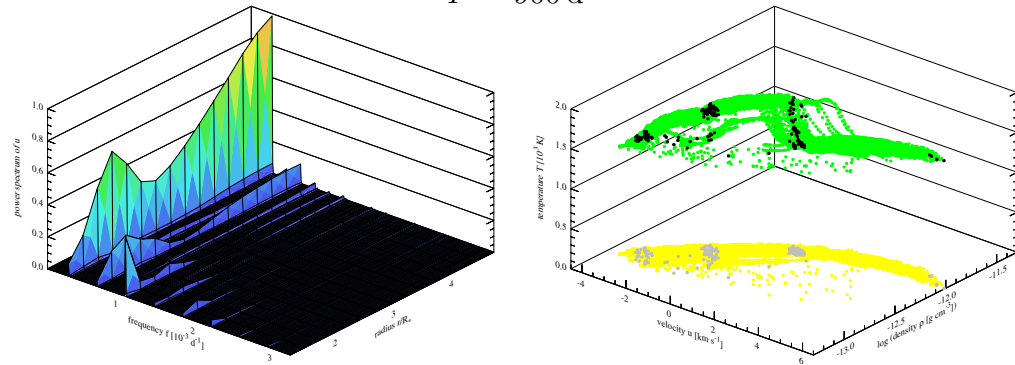
$P = 388$ d $P = 555$ d $P = 900$ d

Figure 4.5: Power spectra (left panels) and stroboscopic maps (right panels) for a CDS excited with various periods P in the dust forming zone at $r = 2.5 R_*$. The maps were obtained by sampling $(u(n0.02P), \rho(n0.02P), T(n0.02P))$ (green) and $(u(nP), \rho(nP), T(nP))$ (black) for $1 \leq n \leq \lfloor t_{\text{max}}/P \rfloor$, $n \in \mathbb{N}$.

determined by FT. For some periods, no integers i and j could be found to satisfy the condition $iP = jP_{\text{CDS}}$. This probably implies that the value of iP is similar or longer than the simulation time of the system for these excitation periods.

Figure 4.5 is consistent with the ideas discussed at the beginning of this section concerning the mass loss rates. With increasing piston period P , the velocity in the dust-nucleation zone is hardly affected, whereas the maximum density is strongly enhanced. Consequently, according to the equation of continuity $\dot{M} = 4\pi r^2 \rho u$, the stellar wind also becomes far more massive.

4.3.2 Excitation strength

To demonstrate the influence of the excitation strength on the shell dynamics, Fig. 4.6 presents the ratio $f_{\text{CDS}}/f_{\kappa}$ and the corresponding overtones as a function of the piston amplitude Δu for $P = 388$ d, which is a typical pulsation period for a Miras type star, and for $P = 1500$ d of the same order of magnitude as P_{CDS} .

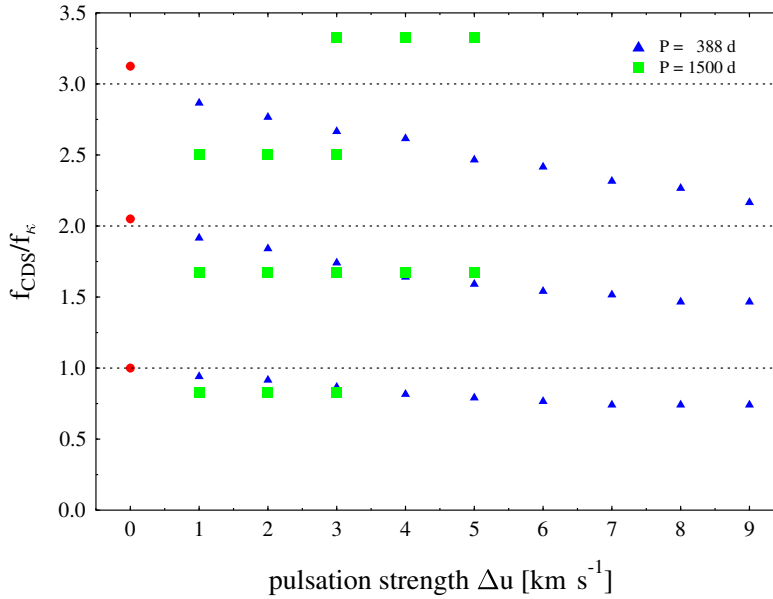


Figure 4.6: Shift of CDS frequencies f_{CDS} related to the eigenmode $f_{\kappa} = 0.41 \cdot 10^{-3} \text{ d}^{-1}$ as a function of excitation strength Δu for excitation period $P = 388$ d (triangles), and $P = 1500$ d (rectangles). The set of CDS-eigenmodes is depicted by circles.

Fig. 4.6 implies that, in the case of short pulsation periods, the oscillation frequencies f_{CDS} decrease with increasing velocity amplitude and approach the value

$f_{\text{CDS}}/f_{\kappa} \approx 0.75$. Although a radial pulsation occurs at the inner boundary, the additional energy input of this external force has almost no influence on the timescale of the circumstellar shell. It barely has an impact on the mass-loss rate $\langle \dot{M} \rangle$, which is enhanced from $9.4 \cdot 10^{-5} \text{ M}_{\odot} \text{ yr}^{-1}$ (no excitation) to $1.5 \cdot 10^{-4} \text{ M}_{\odot} \text{ yr}^{-1}$ (resonance) at an approximately constant final outflow velocity of $\langle u_{\infty} \rangle \approx 17 \text{ km s}^{-1}$ (cf. Table 4.2).

Table 4.2: Resultant quantities of the excitation strength Δu study of model A for $P = 388 \text{ d}$: frequencies f_{CDS} , time averaged mass loss rate $\langle \dot{M} \rangle$, final outflow velocity $\langle u_{\infty} \rangle$, and dust-to-gas mass ratio $\langle \rho_{\text{d}}/\rho_{\text{g}} \rangle$. Values in boldface indicate the strongest mode.

| Δu (km s^{-1}) | f_{CDS} (10^{-3} d^{-1}) | $\langle \dot{M} \rangle$ ($\text{M}_{\odot} \text{ yr}^{-1}$) | $\langle u_{\infty} \rangle$ (km s^{-1}) | $\langle \rho_{\text{d}}/\rho_{\text{g}} \rangle$ | | |
|--------------------------------------|--|---|--|---|------|---------------------|
| 0.0 | 0.41 | 0.83 | 1.25 | $9.6 \cdot 10^{-5}$ | 17.3 | $1.2 \cdot 10^{-3}$ |
| 1.0 | 0.38 | 0.77 | 1.15 | $1.1 \cdot 10^{-4}$ | 17.1 | $1.2 \cdot 10^{-3}$ |
| 2.0 | 0.37 | 0.74 | 1.11 | $1.5 \cdot 10^{-4}$ | 16.6 | $1.2 \cdot 10^{-3}$ |
| 3.0 | 0.35 | 0.70 | 1.07 | $1.7 \cdot 10^{-4}$ | 16.5 | $1.2 \cdot 10^{-3}$ |
| 4.0 | 0.33 | 0.66 | 1.05 | $2.0 \cdot 10^{-4}$ | 16.4 | $1.2 \cdot 10^{-3}$ |
| 5.0 | 0.32 | 0.64 | 0.99 | $2.1 \cdot 10^{-4}$ | 16.2 | $1.2 \cdot 10^{-3}$ |
| 6.0 | 0.31 | 0.62 | 0.97 | $2.4 \cdot 10^{-4}$ | 16.2 | $1.2 \cdot 10^{-3}$ |
| 7.0 | 0.30 | 0.61 | 0.93 | $2.5 \cdot 10^{-4}$ | 16.3 | $1.2 \cdot 10^{-3}$ |
| 8.0 | 0.30 | 0.59 | 0.91 | $2.7 \cdot 10^{-4}$ | 16.1 | $1.2 \cdot 10^{-3}$ |
| 9.0 | 0.30 | 0.59 | 0.87 | $3.0 \cdot 10^{-4}$ | 16.0 | $1.2 \cdot 10^{-3}$ |

While the eigenmodes change by only a small amount for the shorter period $P = 388 \text{ d}$, the influence is more significant for the longer $P = 1500 \text{ d}$. The frequencies are nearly synchronised, i.e., the eigenperiod is detuned to a lower harmonic of the excitation period and remains constant with increasing velocity amplitude. Finally, for a velocity amplitude $\Delta u \gtrsim 3 \text{ km s}^{-1}$, the eigenmode completely vanishes and the excitation period and its harmonics dominate the system (cf. Table 4.3).

In order to examine this more closely, Fig. 4.7 presents spectra and stroboscopic maps for two different strengths of the excitation, i.e. $\Delta u = 1 \text{ km s}^{-1}$ and 5 km s^{-1} , using a fixed excitation period of $P = 1500 \text{ d}$. For the larger velocity amplitude $\Delta u = 5 \text{ km s}^{-1}$, the eigenmodes of the undisturbed CDS are replaced by the excitation period and its harmonics. The shell follows the exterior excitation identified by only one strip in the corresponding map, i.e. $i = j = 1$. Note that the enhanced density for $\Delta u = 5 \text{ km s}^{-1}$ results in a higher mass-loss rate $\langle \dot{M} \rangle = 7.9 \cdot 10^{-4} \text{ M}_{\odot} \text{ yr}^{-1}$ and $\langle u_{\infty} \rangle \approx 16.8 \text{ km s}^{-1}$ compared to

$\langle \dot{M} \rangle = 2.5 \cdot 10^{-4} M_{\odot} \text{ yr}^{-1}$ and $\langle u_{\infty} \rangle \approx 15.6 \text{ km s}^{-1}$ for $\Delta u = 1 \text{ km s}^{-1}$ (cf. Table 4.3).

Table 4.3: Resultant quantities of the excitation strength Δu study of model A for $P = 1500 \text{ d}$: frequencies f_{CDS} , time averaged mass loss rate $\langle \dot{M} \rangle$, final outflow velocity $\langle u_{\infty} \rangle$, and dust-to-gas mass ratio $\langle \rho_{\text{d}}/\rho_{\text{g}} \rangle$. Values in boldface indicate the strongest mode.

| Δu (km s^{-1}) | f_{CDS} (10^{-3} d^{-1}) | $\langle \dot{M} \rangle$ ($M_{\odot} \text{ yr}^{-1}$) | $\langle u_{\infty} \rangle$ (km s^{-1}) | $\langle \rho_{\text{d}}/\rho_{\text{g}} \rangle$ | | | |
|--------------------------------------|--|--|--|---|---------------------|------|---------------------|
| 0.0 | 0.41 | 0.83 | 1.25 | - | $9.6 \cdot 10^{-5}$ | 17.3 | $1.2 \cdot 10^{-3}$ |
| 1.0 | 0.33 | 0.67 | 1.00 | - | $3.0 \cdot 10^{-4}$ | 15.7 | $1.3 \cdot 10^{-3}$ |
| 2.0 | 0.33 | 0.67 | 1.00 | - | $2.9 \cdot 10^{-4}$ | 16.3 | $1.3 \cdot 10^{-3}$ |
| 3.0 | 0.33 | 0.67 | 1.00 | - | $3.2 \cdot 10^{-4}$ | 16.5 | $1.3 \cdot 10^{-3}$ |
| 4.0 | - | 0.67 | - | 1.33 | $4.8 \cdot 10^{-4}$ | 16.3 | $1.2 \cdot 10^{-3}$ |
| 5.0 | - | 0.67 | - | 1.33 | $7.2 \cdot 10^{-4}$ | 17.0 | $1.3 \cdot 10^{-3}$ |

Lagrangian zones

Fig. 4.8 displays the temporal development of the radial position $r(t)$ of Lagrangian zones originating at various heights in the atmosphere for two different excitations of the CDS, i.e. similar to Fig. 4.3 but now with internal stellar pulsation with periods $P = 388 \text{ d}$ (left) and $P = 1500 \text{ d}$ (right). The innermost zones up to $r \approx 1.50 R_{*}$ experience periodically strong shock waves created by the interior pulsation. This leads to a ballistic movement of these zones as can be seen from the course of the radial position $r(t)$ depicted in Fig. 4.8. Around $r \approx 2.25 R_{*}$ the temperature is sufficiently cool to allow dust formation. Then the radiation force acting on the newly formed dust drives the material outwards. The gas-dust mixture leaves the star rather than falling back and creates the star surrounding CDS. The dust formation zone separates the lower atmospheric region from the wind region lying above. While the pulsation period dominates the atmospheric (bounded elements) dynamics, it does not dominate in the upper levels of the wind region. Here the timescale of the dust formation controls the dynamics. The eigenperiod corresponds to about 7 times the pulsation period in case of $P = 388 \text{ d}$ (left panel).

With increasing excitation (Fig. 4.8 right panel), both in period and strength, the superimposed periodic behaviour of the CDS makes way for a monophasic behaviour, i.e. the stellar pulsation period dominates the whole shell dynamics.

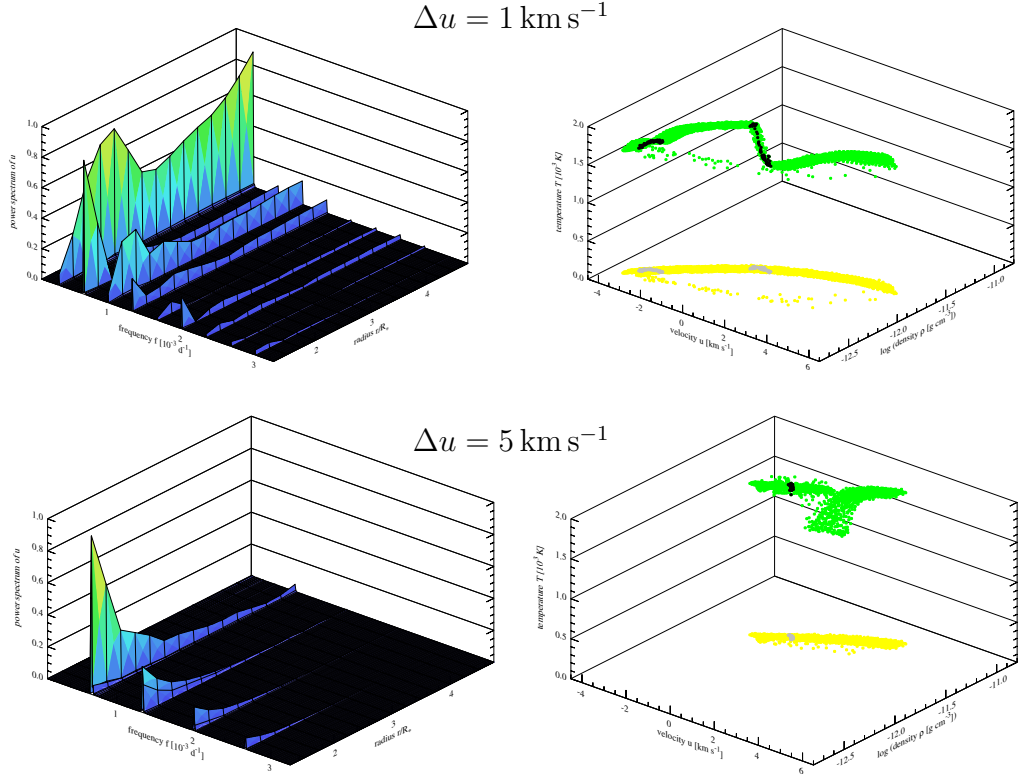


Figure 4.7: Power spectra (left panels) and stroboscopic maps (right panels) for a CDS excited with a period $P = 1500$ d, but with different strengths $\Delta u = 1 \text{ km s}^{-1}$ (upper panel) and 5 km s^{-1} (lower panel), respectively. The plot parameters for the maps are the same as in Fig. 4.5.

4.4 Influence of stellar parameters

To investigate the effects of each individual initial stellar parameter on the dynamical behaviour and the physical structure of a CDS this work has calculated a series of models which differ from each other by only one parameter - mass M_* , luminosity L_* , effective temperature T_* or carbon to oxygen abundance C/O - while keeping all other variables constant. Thereby, the radiative transfer was treated according to Unno & Kondo (1976) and the cooling of the shocked gas follows the isothermal limit case. All models are without pulsation i.e. the piston is locked into its rest position R_0 and the amplitude is held at $\Delta u = 0$. The initial parameter set is the reference model A, already introduced in the previous section. The parameters varied and directly affected quantities such as stellar radius R_* and surface gravity $g(R_*)$, as well as the resultant quantities such as the eigenfrequency f_{κ} , and the temporally averaged mass loss rate $\langle \dot{M} \rangle$, the final outflow

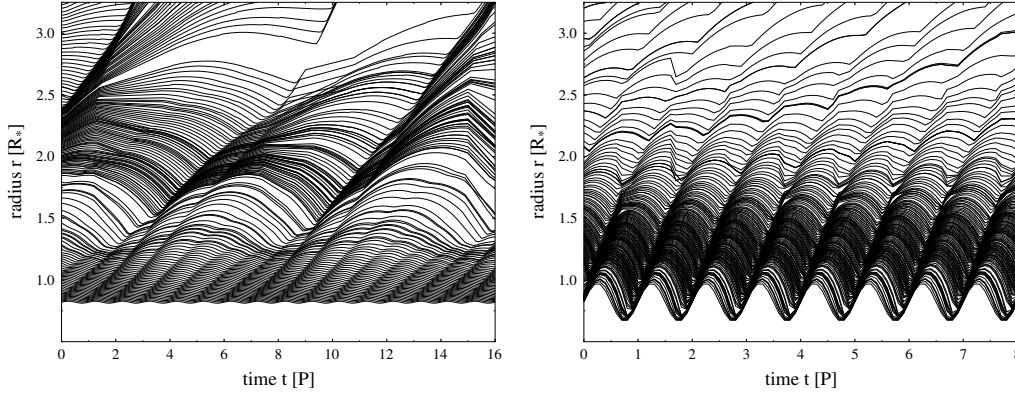


Figure 4.8: Temporal behaviour of some Lagrangian zones in the outer atmosphere and wind of the periodic excited model A. Left: $P = 388$ d, $\Delta u = 1$ km s $^{-1}$ and right $P = 1500$ d, $\Delta u = 5$ km s $^{-1}$.

velocity $\langle u_\infty \rangle$, and the dust-to-gas ratio $\langle \rho_d / \rho_g \rangle$ are listed in Tables 4.4.1 to 4.4.4. The outflow structure is classified in the last column as oscillatory (o), stationary (s) or breeze (b). Additionally a graphical presentation of the dependence of the CDS's eigenfrequency f_κ (green rectangles), the mass loss rate $\langle \dot{M} \rangle$ (red triangles) and the final outflow velocity $\langle u_\infty \rangle$ (blue circles) on the actual varied initial parameter are given in Fig. 4.9 to 4.12.

4.4.1 Stellar luminosity

The stellar luminosity L_* modifies the stellar radius R_* via Eq. (2.27). While keeping all other parameters fixed it then affects the gravity $g(R_*)$ in the outer atmosphere. This results in a changed position of the transition zone to the wind region, i.e. a more or less levitated atmosphere. This clearly implies that the conditions for dust formation are seriously influenced.

For luminosities lower than $L_* \lesssim 7500 L_\odot$, the density at the dust formation zone is extremely small, this implies a very small mass loss rate $\langle \dot{M} \rangle$ i.e. a breeze (see Table 4.4). The velocity u is too small to reach the critical point. It cannot develop a transonic solution, i.e. a supersonic solution and remains subsonic.

On increasing the luminosity the levitated atmosphere provides better dust forming conditions. This is because, the effective radiation force, proportional to the luminosity according to Eq. (2.7), increases and while acting on a given amount of dust the outflow is accelerated to a higher velocity inside the sonic point, where further effective dust condensation and growth take place. For luminosities in the range $10000 L_\odot \lesssim L_* \lesssim 20000 L_\odot$, a stationary, purely dust-driven

wind develops, which is characterised by a slow almost constant outflow velocity $\langle u_\infty \rangle$ and low mass loss $\langle \dot{M} \rangle$ (Fig. 4.9). At a limit luminosity of $L_* \approx 20000 L_\odot$ for the reference model instability of the exterior κ -mechanism leads to an oscillatory wind caused by the feedback of the dust formation process on the radiative transfer. Here, after the formation of an optically-thick dust shell, the temperature inside of this shell increases quickly due to re-emission of radiation by the dust (backwarming), which switches off the nucleation process. The radiation pressure accelerates the dust outwards. If the temperature is cool enough to allow dust formation the cycle starts again. An oscillatory massive wind develops with roughly constant outflow velocities. Longer eigenperiods P_κ are found for models with high luminosities L_* and mass loss rates $\langle \dot{M} \rangle$ (cf. Table 4.4). For large luminosities the system needs more time to enrich the dust forming zone with new condensable material, which was depleted by the previous dust forming cycle. The mass loss rate $\langle \dot{M} \rangle$ beyond $L_* \approx 20000 L_\odot$ seems to be correlated almost linearly with the luminosity L_* as can be seen in Fig. 4.9.

Table 4.4: Influence of the stellar luminosity L_* on the CDS dynamics. Given are the directly influenced stellar radius R_* and surface gravity $g(R_*)$ as well as the CDS-eigenfrequency f_κ and temporally averaged quantities such as mass loss $\langle \dot{M} \rangle$, outflow velocity $\langle u_\infty \rangle$ and dust-to-gas ratio $\langle \rho_d / \rho_g \rangle$. In the last column the wind structure is classified as oscillatory (o), stationary (s) or breeze (b).

| L_* (L_\odot) | R_* (R_\odot) | $g(R_*)$ (cm s^{-2}) | f_κ (10^{-3} d^{-1}) | $\langle \dot{M} \rangle$ ($M_\odot \text{ yr}^{-1}$) | $\langle u_\infty \rangle$ (km s^{-1}) | $\langle \rho_d / \rho_g \rangle$ | Type |
|------------------------|------------------------|------------------------------------|--|--|--|-----------------------------------|------------------|
| 5000 | 392 | $1.8 \cdot 10^{-1}$ | 4.89 | $3.1 \cdot 10^{-17}$ | 0.01 | $5.1 \cdot 10^{-4}$ | b* |
| 7500 | 480 | $1.2 \cdot 10^{-1}$ | - | $8.3 \cdot 10^{-15}$ | 0.02 | $2.1 \cdot 10^{-6}$ | b* |
| 10000 | 554 | $8.9 \cdot 10^{-2}$ | 2.75 | $9.5 \cdot 10^{-12}$ | 0.3 | $3.8 \cdot 10^{-7}$ | s ^{†,‡} |
| 12500 | 620 | $7.1 \cdot 10^{-2}$ | 1.11 | $3.4 \cdot 10^{-08}$ | 1.2 | $4.6 \cdot 10^{-4}$ | s [‡] |
| 15000 | 679 | $6.0 \cdot 10^{-2}$ | 0.88 | $3.4 \cdot 10^{-08}$ | 1.3 | $5.1 \cdot 10^{-4}$ | s [‡] |
| 20000 | 784 | $4.5 \cdot 10^{-2}$ | - | $4.5 \cdot 10^{-07}$ | 1.7 | $4.5 \cdot 10^{-4}$ | s |
| 25000 | 876 | $3.6 \cdot 10^{-2}$ | 3.10 | $6.0 \cdot 10^{-05}$ | 14.8 | $1.1 \cdot 10^{-3}$ | o |
| 30000 | 960 | $3.0 \cdot 10^{-2}$ | 4.00 | $1.1 \cdot 10^{-04}$ | 17.1 | $1.2 \cdot 10^{-3}$ | o |
| 35000 | 1037 | $2.6 \cdot 10^{-2}$ | 3.60 | $1.4 \cdot 10^{-04}$ | 17.1 | $1.3 \cdot 10^{-3}$ | o |
| 40000 | 1109 | $2.2 \cdot 10^{-2}$ | 3.10 | $2.2 \cdot 10^{-04}$ | 17.3 | $1.2 \cdot 10^{-3}$ | o |
| 45000 | 1176 | $2.0 \cdot 10^{-2}$ | 2.80 | $2.7 \cdot 10^{-04}$ | 17.1 | $1.3 \cdot 10^{-3}$ | o |
| 50000 | 1239 | $1.8 \cdot 10^{-2}$ | 2.70 | $3.4 \cdot 10^{-04}$ | 18.2 | $1.2 \cdot 10^{-3}$ | o |

time average $\langle x \rangle$ at $r = 3 R_$

† time average $\langle x \rangle$ at $r = 10 R_*$

‡ stationary wind with small disturbances

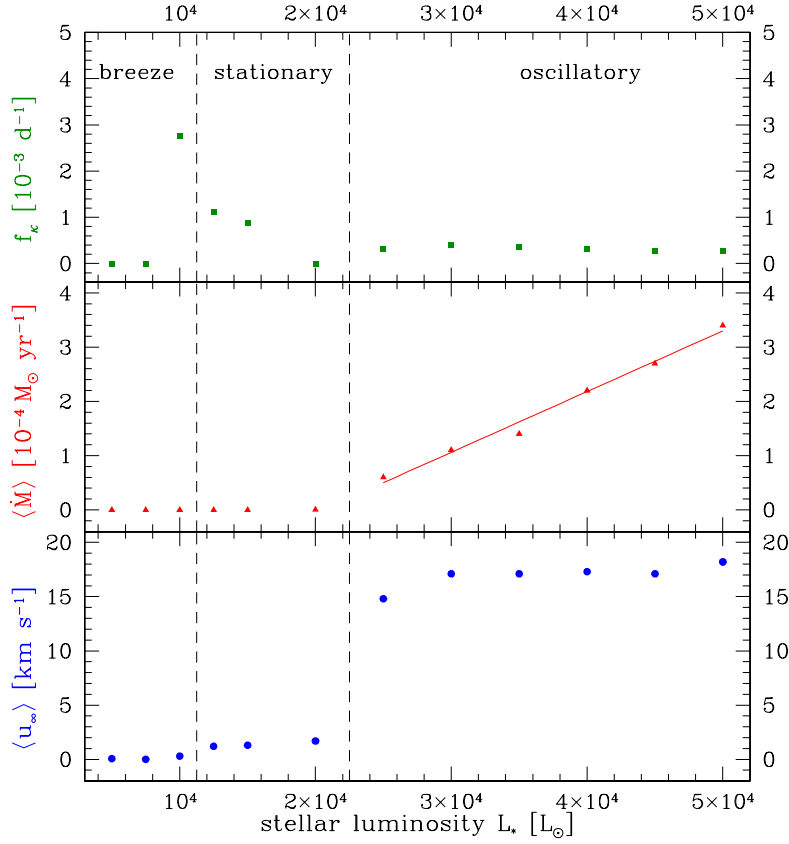


Figure 4.9: Dependence of the eigenfrequency f_κ , the mass loss rate $\langle \dot{M} \rangle$, and the final outflow velocity $\langle u_\infty \rangle$ on the stellar luminosity L_*

4.4.2 Overabundance of carbon to oxygen

The C/O - abundance affects the amount of condensable material $n_{\text{cond}} = (\epsilon_C - \epsilon_O) / n_H$ available for the dust nucleation after the oxygen is stored as CO - molecules. This means, that because of higher collision rates more clusters are formed. A larger number of dust grains causes a higher degree of condensation Eq. (2.23) and finally an increasing effective acceleration due to radiation pressure on dust according to Eq. (2.7).

For the set of parameters under investigation, there exists a stationary wind solution at C/O = 1.1. The available amount of dust is too low to initiate the feedback between the dust complex and the radiation (exterior κ -mechanism).

The modelled results (cf. Table 4.5) suggest that, the exterior κ -mechanism instability sets in at slightly higher values of the carbon overabundance of C/O \approx 1.2. An increase of the C/O-ratio results in an increasing terminal velocity $\langle u_\infty \rangle$ at almost constant mass loss rate $\langle \dot{M} \rangle$ as can be seen in Fig. 4.10. Similar results

were found by Winters et al. (2000) for excited CDSs, Dominik et al. (1990) and Habing et al. (1994) for stationary dust driven wind models. The final velocity of the outflow seems to be linearly correlated to the abundance ratio of C/O.

To sum up the results, the dust formation process in the CDS has its own timescale, which is decisively determined by the abundances of the dust forming elements, i.e. by the carbon overabundances ϵ_C . The higher the carbon overabundance the less time is needed to sweep up sufficient material for producing a shock wave. Hence the CDS's eigenperiod P_κ decreases with C/O-ratio (Table 4.10).

Table 4.5: Influence of the carbon to oxygen ratio C/O on the CDS dynamics. The listed quantities are the same as in Table 4.4

| C/O | R_* (R_\odot) | $g(R_*)$ (cm s^{-2}) | f_κ (10^{-3}d^{-1}) | $\langle \dot{M} \rangle$ ($M_\odot \text{yr}^{-1}$) | $\langle u_\infty \rangle$ (km s^{-1}) | $\langle \rho_d / \rho_g \rangle$ | Type |
|-----|------------------------|------------------------------------|---|---|--|-----------------------------------|------|
| 1.1 | 960 | $3.0 \cdot 10^{-2}$ | - | $1.6 \cdot 10^{-7}$ | 0.7 | $2.1 \cdot 10^{-4}$ | s* |
| 1.2 | 960 | $3.0 \cdot 10^{-2}$ | 0.22 | $8.5 \cdot 10^{-5}$ | 11.9 | $8.3 \cdot 10^{-4}$ | o |
| 1.3 | 960 | $3.0 \cdot 10^{-2}$ | 0.41 | $1.1 \cdot 10^{-4}$ | 18.7 | $1.5 \cdot 10^{-3}$ | o |
| 1.4 | 960 | $3.0 \cdot 10^{-2}$ | 0.64 | $7.1 \cdot 10^{-5}$ | 25.9 | $1.8 \cdot 10^{-3}$ | o |
| 1.5 | 960 | $3.0 \cdot 10^{-2}$ | 0.72 | $7.3 \cdot 10^{-5}$ | 29.4 | $2.5 \cdot 10^{-3}$ | o |
| 1.6 | 960 | $3.0 \cdot 10^{-2}$ | 0.78 | $5.7 \cdot 10^{-5}$ | 31.4 | $2.9 \cdot 10^{-3}$ | o |
| 1.7 | 960 | $3.0 \cdot 10^{-2}$ | 0.99 | $5.7 \cdot 10^{-5}$ | 36.5 | $3.5 \cdot 10^{-3}$ | o |
| 1.8 | 960 | $3.0 \cdot 10^{-2}$ | 1.03 | $6.6 \cdot 10^{-5}$ | 38.1 | $3.8 \cdot 10^{-3}$ | o |
| 1.9 | 960 | $3.0 \cdot 10^{-2}$ | 1.13 | $6.9 \cdot 10^{-5}$ | 41.6 | $4.5 \cdot 10^{-3}$ | o |
| 2.0 | 960 | $3.0 \cdot 10^{-2}$ | 1.26 | $7.2 \cdot 10^{-5}$ | 44.2 | $4.9 \cdot 10^{-3}$ | o |
| 2.2 | 960 | $3.0 \cdot 10^{-2}$ | 1.43 | $6.8 \cdot 10^{-5}$ | 49.0 | $6.1 \cdot 10^{-3}$ | o |
| 2.5 | 960 | $3.0 \cdot 10^{-2}$ | 1.68 | $6.2 \cdot 10^{-5}$ | 54.6 | $7.7 \cdot 10^{-3}$ | o |

time average $\langle x \rangle$ at $r = 15 R_$

4.4.3 Stellar mass

Increasing the stellar mass M_* results in a higher gravity g for a given stellar radius R_* (cf. Eq. (2.3)). With L_* fixed, i.e. at constant radiation force, the radiative acceleration in units of the gravitational deceleration Γ decreases according to Eq. (2.7), which finally leads to a lower final outflow velocity and smaller mass loss (Fig. 4.11).

For masses lower than $1.2 M_\odot$, the exterior κ -mechanism dominates the wind dynamics. Since this mechanism amplifies the rate of dust formation, massive winds with mass loss rates of $\approx 10^{-4} M_\odot \text{yr}^{-1}$ and velocities of $\approx 16 \text{km s}^{-1}$ are obtained.

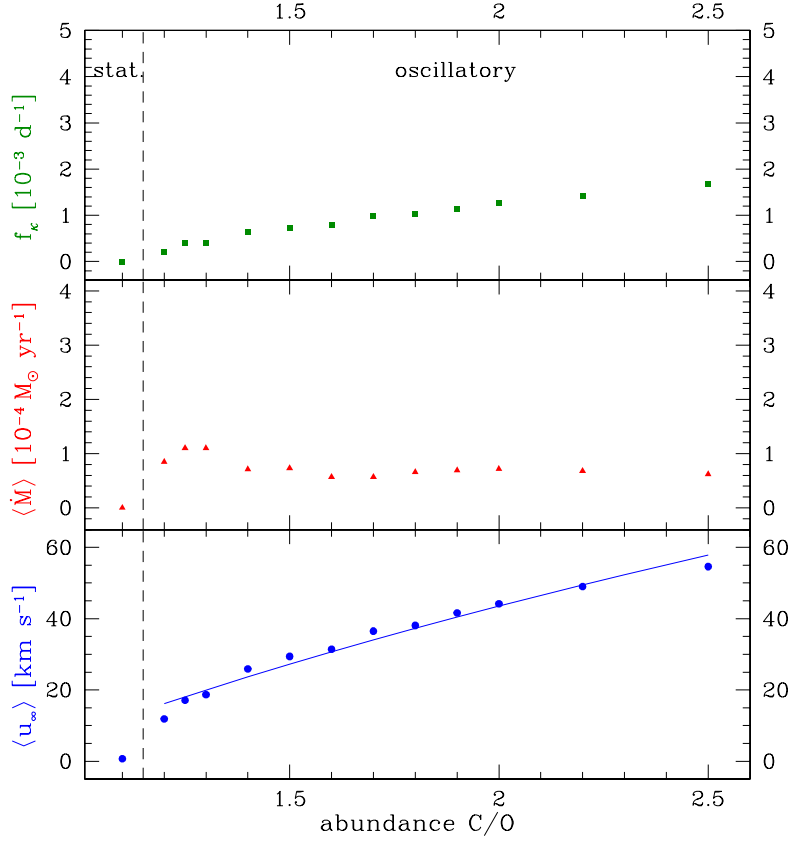


Figure 4.10: Dependence of the eigenfrequency f_κ , the mass loss rate $\langle \dot{M} \rangle$, and the final outflow velocity $\langle u_\infty \rangle$ on the carbon to oxygen ratio C/O

For masses larger than $1.2 M_\odot$ the feedback between dust and radiation breaks up, because the higher gravity does not allow the levitation of enough material into the dust forming region. Hence, a stationary wind develops. An increase of the C/O -ratio moves this limit mass towards higher masses.

4.4.4 Effective stellar temperature

Increasing the stellar temperature T_* directly affects the stellar radius R_* according to Eq. (2.27) hence the gravity $g(R_*)$. In such cases, not only a higher temperature but also a higher gravity hamper the dust nucleation. High temperature condensates of amorphous carbon are already obtained at temperatures of $T_c \approx 1500$ K. On increasing the stellar temperature the dust-forming window moves outward and becomes thinner in the range, which does not allow effective dust formation.

Table 4.6: Influence of the stellar mass M_* on the CDS dynamics. The listed quantities are the same as in Table 4.4

| M_* (M_\odot) | R_* (R_\odot) | $g(R_*)$ (cm s^{-2}) | f_κ (10^{-3} d^{-3}) | $\langle \dot{M} \rangle$ ($M_\odot \text{ yr}^{-1}$) | $\langle u_\infty \rangle$ (km s^{-1}) | $\langle \rho_d / \rho_g \rangle$ | Type |
|------------------------|------------------------|------------------------------------|--|--|--|-----------------------------------|------|
| 0.9 | 960 | $2.7 \cdot 10^{-2}$ | 0.36 | $1.6 \cdot 10^{-04}$ | 16.3 | $1.3 \cdot 10^{-3}$ | o |
| 1.0 | 960 | $3.0 \cdot 10^{-2}$ | 0.40 | $1.0 \cdot 10^{-04}$ | 17.0 | $1.2 \cdot 10^{-3}$ | o |
| 1.1 | 960 | $3.3 \cdot 10^{-2}$ | 0.30 | $6.5 \cdot 10^{-05}$ | 15.6 | $1.1 \cdot 10^{-3}$ | o |
| 1.2 | 960 | $3.6 \cdot 10^{-2}$ | - | $7.2 \cdot 10^{-07}$ | 1.9 | $3.8 \cdot 10^{-4}$ | s |
| 1.3 | 960 | $3.9 \cdot 10^{-2}$ | - | $2.1 \cdot 10^{-07}$ | 1.7 | $3.8 \cdot 10^{-4}$ | s |
| 1.4 | 960 | $4.2 \cdot 10^{-2}$ | 0.60 | $5.0 \cdot 10^{-08}$ | 1.5 | $3.6 \cdot 10^{-4}$ | s* |
| 1.5 | 960 | $4.5 \cdot 10^{-2}$ | 0.70 | $8.2 \cdot 10^{-09}$ | 1.6 | $3.0 \cdot 10^{-4}$ | s* |
| 1.6 | 960 | $4.8 \cdot 10^{-2}$ | 0.72 | $2.4 \cdot 10^{-10}$ | 1.8 | $2.5 \cdot 10^{-6}$ | s* |

*stationary wind with small oscillatory disturbances

For temperatures $2050 \text{ K} \lesssim T_* \lesssim 2500 \text{ K}$ the conditions for dust formation are optimal. The temperature as well as the gravity are low enough to allow dust nucleation and subsequent growth. The coupling between dust and radiation yields an oscillatory, massive wind with almost constant outflow velocities. Also, the CDS's eigenperiod P_κ decreases.

The results (cf. Table 4.7) suggest that the temperature limit for developing an exterior κ -mechanism seems to lie about $T_* \approx 2500 \text{ K}$ for the investigated parameter set.

At $T_* \gtrsim 2500 \text{ K}$ the dust forming zone is already moved too far into thinner regions to allow effective dust nucleation. A stationary wind and finally a breeze are obtained.

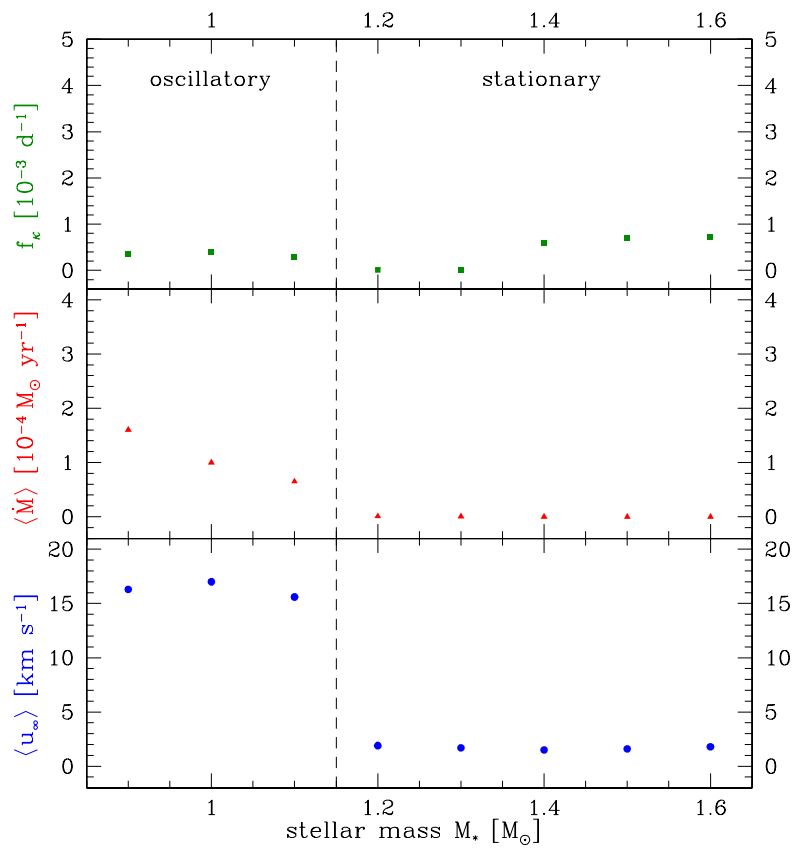


Figure 4.11: Dependence of the eigenfrequency f_κ , the mass loss rate $\langle \dot{M} \rangle$, and the final outflow velocity $\langle u_\infty \rangle$ on the stellar mass M_* .

Table 4.7: Influence of the stellar effective temperature T_* on the CDS dynamics. The listed quantities are the same as in Table 4.4

| T_* (K) | R_* (R_\odot) | $g(R_*)$ (cm s^{-2}) | f_κ (10^{-3} d^{-1}) | $\langle \dot{M} \rangle$ ($M_\odot \text{ yr}^{-1}$) | $\langle u_\infty \rangle$ (km s^{-1}) | $\langle \rho_d / \rho_g \rangle$ | Type |
|--------------|------------------------|------------------------------------|--|--|--|-----------------------------------|----------------|
| 2050 | 1371 | $1.5 \cdot 10^{-2}$ | 0.30 | $2.3 \cdot 10^{-04}$ | 16.2 | $1.3 \cdot 10^{-3}$ | o |
| 2200 | 1190 | $1.9 \cdot 10^{-2}$ | 0.33 | $2.6 \cdot 10^{-04}$ | 17.0 | $1.2 \cdot 10^{-3}$ | o |
| 2300 | 1089 | $2.3 \cdot 10^{-2}$ | 0.35 | $2.4 \cdot 10^{-04}$ | 16.2 | $1.2 \cdot 10^{-3}$ | o |
| 2400 | 1000 | $2.7 \cdot 10^{-2}$ | 0.39 | $1.4 \cdot 10^{-04}$ | 16.8 | $1.3 \cdot 10^{-3}$ | o |
| 2450 | 960 | $3.0 \cdot 10^{-2}$ | 0.40 | $1.0 \cdot 10^{-04}$ | 17.0 | $1.2 \cdot 10^{-3}$ | o |
| 2500 | 922 | $3.2 \cdot 10^{-2}$ | 0.43 | $8.0 \cdot 10^{-05}$ | 17.3 | $1.2 \cdot 10^{-3}$ | o |
| 2600 | 852 | $3.8 \cdot 10^{-2}$ | - | $8.8 \cdot 10^{-07}$ | 2.2 | $2.8 \cdot 10^{-4}$ | s |
| 2700 | 791 | $4.4 \cdot 10^{-2}$ | - | $1.5 \cdot 10^{-07}$ | 1.8 | $2.5 \cdot 10^{-4}$ | s |
| 2800 | 735 | $5.1 \cdot 10^{-2}$ | 2.10 | $1.7 \cdot 10^{-08}$ | 0.6 | $1.8 \cdot 10^{-4}$ | s* |
| 2900 | 685 | $5.8 \cdot 10^{-2}$ | 2.33 | $1.1 \cdot 10^{-09}$ | 0.06 | $9.7 \cdot 10^{-5}$ | b [†] |
| 3000 | 640 | $6.7 \cdot 10^{-2}$ | 3.26 | $3.6 \cdot 10^{-11}$ | 0.004 | $2.0 \cdot 10^{-5}$ | b [‡] |

* stationary wind with small oscillatory disturbances

[†] time average $\langle x \rangle$ at $r = 10 R_*$

[‡] time average $\langle x \rangle$ at $r = 5 R_*$

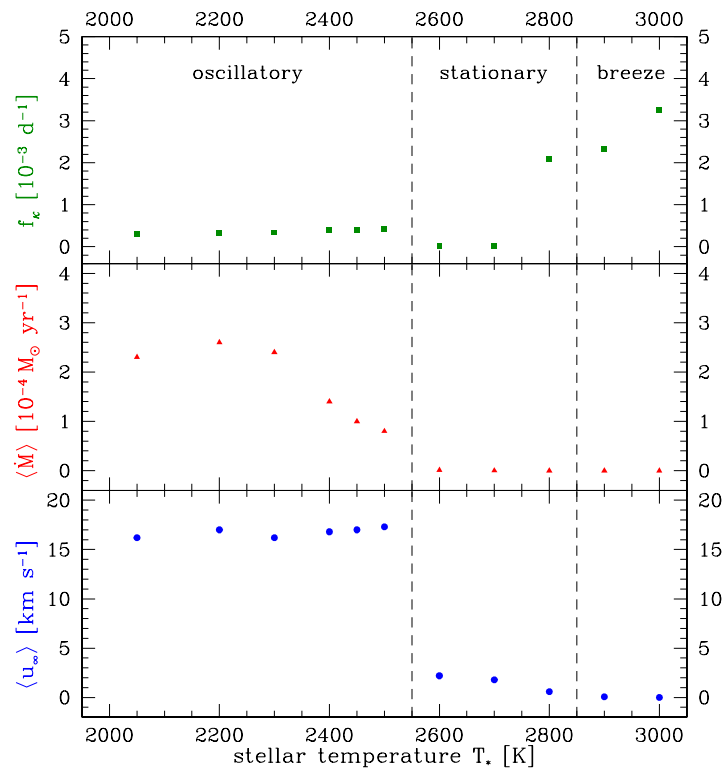


Figure 4.12: Dependence of the eigenfrequency f_κ , the mass loss rate $\langle \dot{M} \rangle$, and the final outflow velocity $\langle u_\infty \rangle$ on the stellar effective temperature T_*

Chapter 5

Dynamics of CDSs around less luminous AGB stars

The condition for a purely dust-driven wind by the exterior κ -mechanism is only properly fulfilled at the very end of the AGB evolution. If the stellar luminosity decreases, the dominance of the dust with respect to the CDS dynamics at first diminishes. Then, further reduction eventually leads to a vanishing outflow, if no additional energy input is provided (cf. Sect. 4.4.1). AGBs with low and standard luminosities ($L_* \leq 12000 L_\odot$) do not generate neither a CDS nor self-induced shocks and outflows with self-maintained oscillatory patterns solely caused by the dust formation (exterior κ -mechanism). Generating a CDS requires input of momentum and energy via an additional mechanism in order to levitate material into the outer atmosphere, i.e. into the dust forming window. An example of such a mechanism can be the pulsation of the outer layers of a red giant as generated by an internal κ -mechanism (Cox (1983)). The pulsation provides the star with mechanical momentum for levitating the material in their atmosphere.

5.1 Eigendynamics of CDSs

To examine the eigendynamics of a CDS around a standard or low luminous AGB star e.g. with the reference stellar parameters (hereafter referred to as model B):

$$\begin{aligned}L_* &= 9 \cdot 10^3 L_\odot \\M_* &= 1 M_\odot \\T_* &= 2500 \text{ K} \\C/O &= 1.75 \\R_0 &= 0.87 R_*\end{aligned}$$

the additional mechanism of pulsation is adopted to be irregular (stochastically determined), such as generated e.g. by convection in a red giant atmosphere. The reason for this assumption is to avoid the dominance of the stellar pulsation on the CDS dynamics. The shell has been excited with different noise intensities $\sigma = (0.1, 0.5, 1.0, 2.0) \text{ km s}^{-1}$ and sequences up to 24 models have been calculated (see Table 5.1) each with the same set of fundamental stellar parameters, but for different realisations of the stochastic process as described in Sect. 2.2.3. The stochastic movement of the inner boundary R_{in} and the corresponding velocity u_{in} for an arbitrary stochastic realisation with intensity $\sigma = 0.1 \text{ km s}^{-1}$ are displayed in Fig. 5.1.

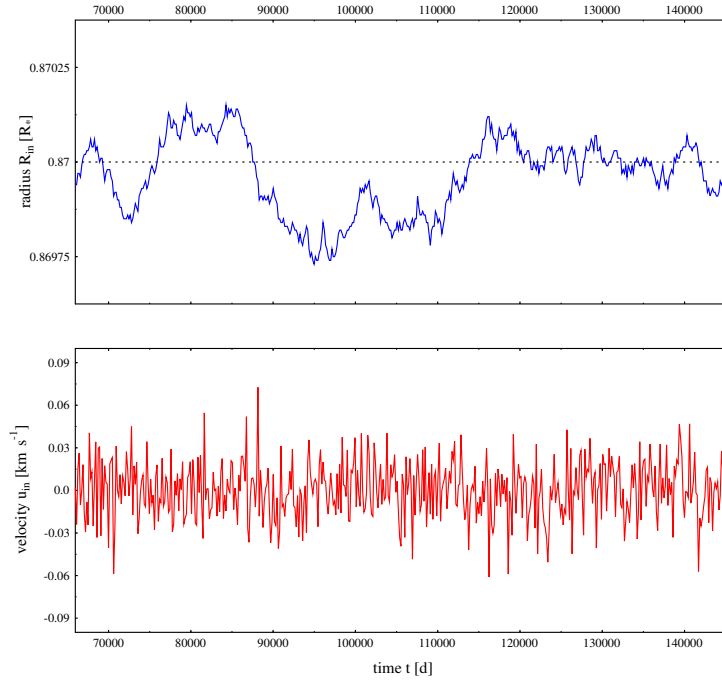


Figure 5.1: Stochastic movement of the inner boundary R_{in} about an equilibrium position $R_0 = 0.87 R_*$ (upper panel) and associated velocity u_{in} (lower panel) for the reference model B with stochastic excitation strength $\sigma = 0.1 \text{ km s}^{-1}$.

Figure 5.2 shows the resulting radial shell structure of some physical quantities describing a CDS at an instant of time for the calculated intensity strengths $\sigma = 0.1 \text{ km s}^{-1}$ (left) and $\sigma = 1.0 \text{ km s}^{-1}$ (right).

The higher input of mechanical energy in the model with $\sigma = 1.0 \text{ km s}^{-1}$ can be immediately seen from the higher amplitude of the innermost shock compared to the model with $\sigma = 0.1 \text{ km s}^{-1}$ (uppermost panels). Since the density scale

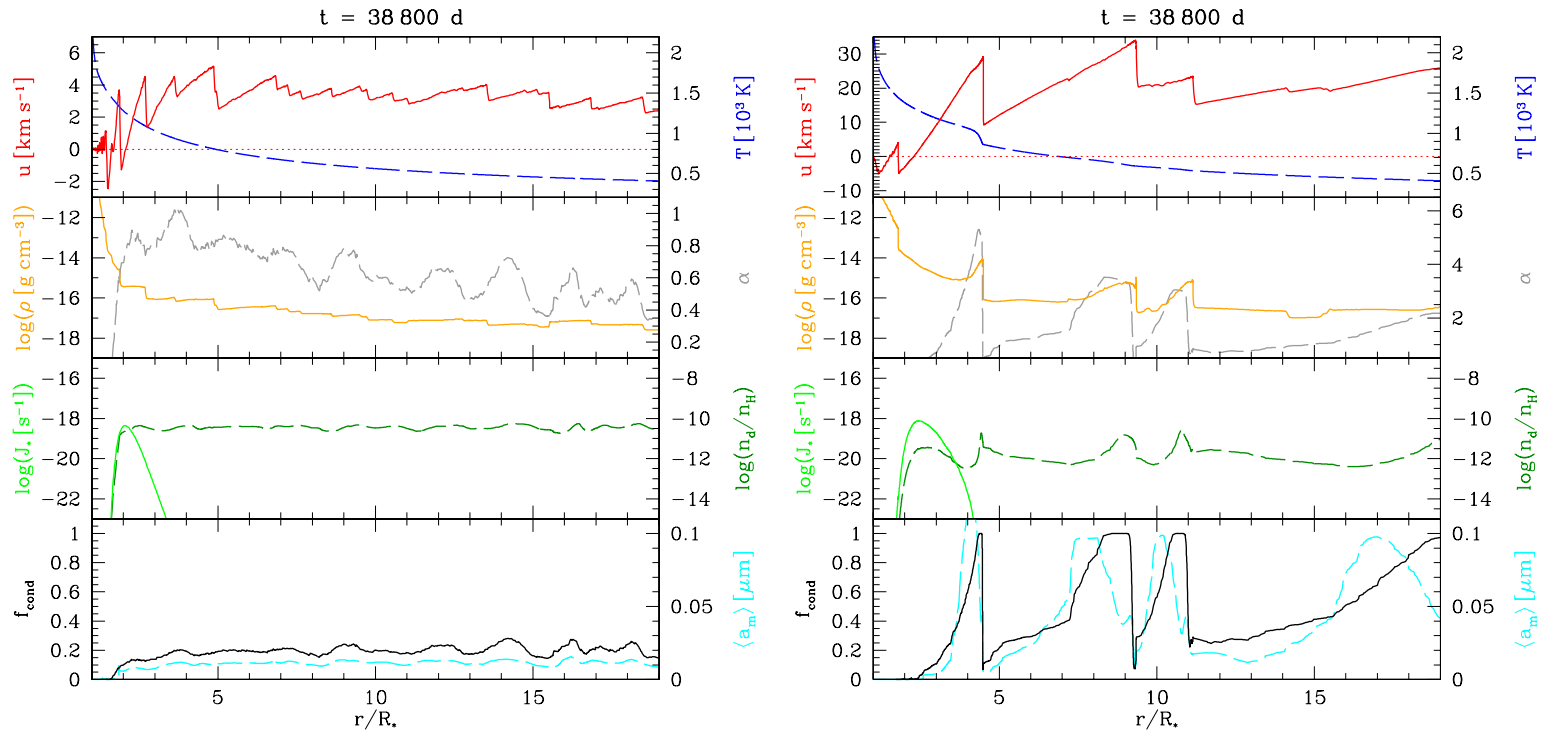


Figure 5.2: Radial structure of stochastic excited CDSs with excitation strength $\sigma = 0.1 \text{ km s}^{-1}$ (left) and $\sigma = 1.0 \text{ km s}^{-1}$ (right). *Upper panel*: gas velocity u (solid line), gas temperature T (dashed line), *second panel*: mass density ρ (solid line), radiative acceleration on dust in units of the local gravitational deceleration α (dashed line), *third panel*: stationary nucleation rate J_* (solid line), number of dust grains per H-atom n_d/n_H (dashed line), *lower panel*: degree of condensation of carbon f_{cond} (solid line), mean particle radius $\langle a_m \rangle$ (dashed line).

height is the same for both models in the inner region, the higher energy input yields a smoother transition to the wind region, i.e. a more levitated atmosphere and thus favourable conditions for dust formation (second panels). The outflow is initiated by the pulsation but is accelerated by the dust. The stellar radiation is blocked by the opacity of the instantly formed shell, thereby heating the material behind it, which is located at smaller radii. This backwarming effect prevents new dust from forming and demonstrates that formation and growth of grains also has a significant influence on the thermodynamical shell structure. As depicted in the lowermost left panel for $\sigma = 0.1 \text{ km s}^{-1}$, the radial structure is rather smooth with an almost constant degree of condensation $f_{\text{cond}} \approx 0.2$, i.e. only 20% of the condensable carbon has actually condensed into solid particles. This results in an optically thin $\langle \dot{M} \rangle \approx 9.5 \cdot 10^{-8} M_{\odot} \text{ yr}^{-1}$, low-velocity $\langle u_{\infty} \rangle \approx 3.6 \text{ km s}^{-1}$ dust-driven wind. For $\sigma = 1.0 \text{ km s}^{-1}$ in the (lowermost right panel), the wind becomes rather irregular but shows the well-known onion-like shell structure. The terminal velocity shows a typical value of several tens of kilometres per second for an AGB star, namely $\langle u_{\infty} \rangle \approx 25.4 \text{ km s}^{-1}$. The calculated time-averaged mass loss rate is $\langle \dot{M} \rangle = 4.5 \cdot 10^{-6} M_{\odot} \text{ yr}^{-1}$. For both excitation strengths the nucleation zone can be localised around $(2 - 3) R_*$ (third panels).

Each of these stochastically excited CDSs was subjected to a Fourier transform. Averaging all stochastic realisations provides an overall mean power spectrum of the local expansion gas velocity u , which is presented in Fig. 5.3 for the same excitation strengths as already discussed in Fig. 5.2. See also Table 5.1.

Table 5.1: List of model calculations and resultant quantities for stochastically excited model B. Given are the excitation strength σ , the number of ensemble members, ensemble averaged CDS-eigenfrequencies f_{κ} at dust forming zone at $r = 2.5 R_*$, time averaged mass loss rate $\langle \dot{M} \rangle$, outflow velocity $\langle u_{\infty} \rangle$, and dust-to-gas mass ratio $\langle \rho_d / \rho_g \rangle$

| σ (km s^{-1}) | No. | f_{κ} (10^{-3} d^{-1}) | | | | $\langle \dot{M} \rangle$ ($M_{\odot} \text{ yr}^{-1}$) | $\langle u_{\infty} \rangle$ (km s^{-1}) | $\langle \rho_d / \rho_g \rangle$ | |
|------------------------------------|-----|--|-------------|-------------|------|--|--|-----------------------------------|---------------------|
| 0.1 | 23 | 0.06 | 0.51 | - | 1.58 | - | $6.6 \cdot 10^{-7}$ | 6.0 | $1.4 \cdot 10^{-3}$ |
| 0.5 | 13 | 0.05 | - | 1.04 | 1.54 | 2.13 | $5.0 \cdot 10^{-6}$ | 23.4 | $2.8 \cdot 10^{-3}$ |
| 1.0 | 9 | 0.06 | - | 1.13 | 1.50 | 2.13 | $4.8 \cdot 10^{-6}$ | 25.1 | $3.0 \cdot 10^{-3}$ |
| 2.0 | 21 | 0.06 | - | 1.19 | 1.51 | 2.22 | $5.4 \cdot 10^{-6}$ | 25.2 | $3.0 \cdot 10^{-3}$ |

To gain more insight, Fig. 5.4 illustrates the power spectra for some selected radial positions within the circumstellar shell. For the case of small excitation strength $\sigma = 0.1 \text{ km s}^{-1}$ the response spectra are dominated by three distinct peaks

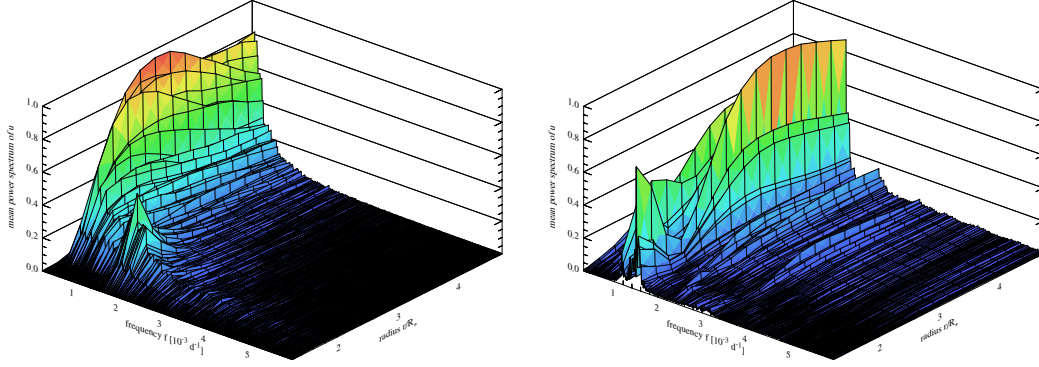


Figure 5.3: Normalised mean power spectra of the radial gas velocity u caused by stochastic excitation of strength $\sigma = 0.1 \text{ km s}^{-1}$ (left) and $\sigma = 1.0 \text{ km s}^{-1}$ (right).

firstly at $f_\kappa = 0.06 \cdot 10^{-3} \text{ d}^{-1} \approx (17000 \text{ d})^{-1}$, secondly at $f_\kappa = 0.51 \cdot 10^{-3} \text{ d}^{-1} \approx (1960 \text{ d})^{-1}$ and thirdly at $f_\kappa = 1.58 \cdot 10^{-3} \text{ d}^{-1} \approx (630 \text{ d})^{-1}$. The amplitude of the third frequency becomes maximal near the inner edge of the dust nucleation zone at $r/R_* = 1.75$ and diminishes rapidly with further increasing distance from the star. Beyond $r/R_* = 1.75$, dust formation sets in and the first and second maxima at $f_\kappa = 0.06 \cdot 10^{-3} \text{ d}^{-1} \approx (17000 \text{ d})^{-1}$ and at $f_\kappa = 0.51 \cdot 10^{-3} \text{ d}^{-1} \approx (1960 \text{ d})^{-1}$ become clearly visible. They eventually dominate the spectrum for $r/R_* > 1.75$.

For the larger excitation strength $\sigma = 1.0 \text{ km s}^{-1}$, the power spectrum looks much richer in detail than for $\sigma = 0.1 \text{ km s}^{-1}$ with at least five distinct maxima. Even closer to the star where the medium is too hot to allow for effective dust formation, two strong peaks at $f_\kappa = 1.50 \cdot 10^{-3} \text{ d}^{-1} \approx (670 \text{ d})^{-1}$ and $f_\kappa = 1.13 \cdot 10^{-3} \text{ d}^{-1} \approx (885 \text{ d})^{-1}$ can be seen. Here, the dynamics of the gas are influenced by the backwarming of the dust and the dilution wave originating in the dust nucleation zone (cf. Sect. 4.2). With increasing distance from the star, additional maxima appear at $f_\kappa = 0.06 \cdot 10^{-3} \text{ d}^{-1} \approx (17000 \text{ d})^{-1}$, $f_\kappa = 2.13 \cdot 10^{-3} \text{ d}^{-1} \approx (470 \text{ d})^{-1}$ and $f_\kappa = 3.2 \cdot 10^{-3} \text{ d}^{-1} \approx (310 \text{ d})^{-1}$. The latter seems to be harmonics of the $f_\kappa = 0.51 \cdot 10^{-3} \text{ d}^{-1} \approx (1960 \text{ d})^{-1}$ feature determined for low excitation strength $\sigma = 0.1 \text{ km s}^{-1}$.

Similar to the case of a self-excited CDS (see Sect. 4.2), which can be characterised by an eigenmode P_κ , the observed frequency maxima are characteristic of the dynamics of the circumstellar shell. These results show that a CDS does not simply mimic an external excitation but has its own eigenmodes which are determined by the complex interplay between dust formation and growth, radiative transfer and hydrodynamics. It has also become apparent that the response of the CDS strongly depends on the excitation strength. It is assumed that the maxima at $f_\kappa = 1.58 \cdot 10^{-3} \text{ d}^{-1} \approx (630 \text{ d})^{-1}$ for $\sigma = 0.1 \text{ km s}^{-1}$ and at

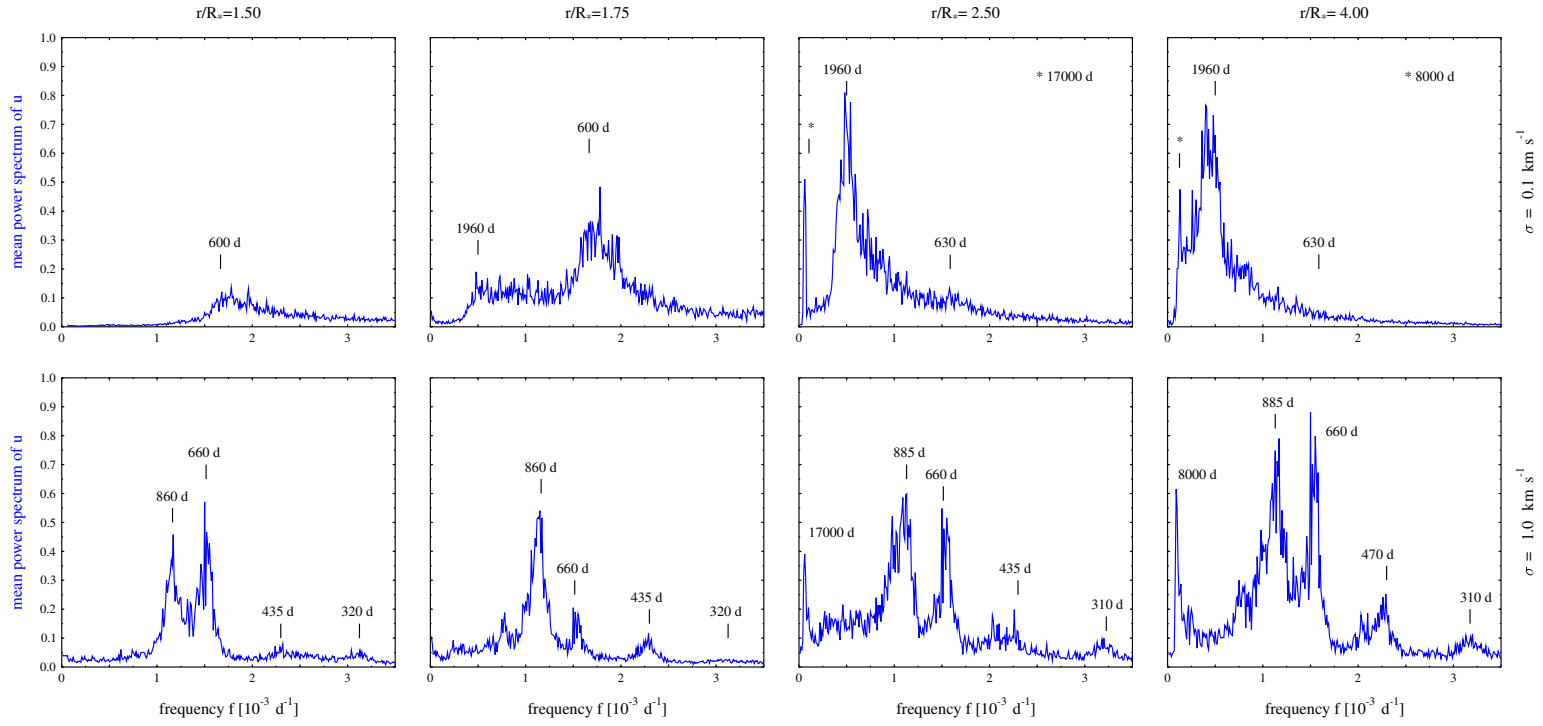


Figure 5.4: Selected mean power spectrum profiles of the gas velocity u at different radii r for the noise intensities $\sigma = 0.1 \text{ km s}^{-1}$ (upper panels), and $\sigma = 1.0 \text{ km s}^{-1}$ (lower panels), respectively.

$f_\kappa = 1.50 \cdot 10^{-3} \text{d}^{-1} \approx (670 \text{d})^{-1}$ for $\sigma = 1.0 \text{ km s}^{-1}$ belong to the same eigenmode, whose frequency is detuned towards smaller values as the strength of the excitation increases. This is consistent with the results for a sinusoidal excitation as will be shown in the next section.

5.2 Dynamics of perturbed CDSs

This section examines the response of the CDS to an external excitation by a sinusoidally oscillating stellar atmosphere. Due to the inherent non-linearities of a dust-forming system, the CDS does not generally oscillate with the applied frequency but usually exhibits a much more complex behaviour. Depending on the excitation frequency it may exhibit irregular or periodic behaviour. Since the dynamics in CDSs are strongly influenced by the presence of dust, the investigation focuses on the dust-formation zone.

5.2.1 Perturbation frequency

Figure 5.5 shows the most dominant shell modes related to the eigenfrequency f_{CDS}/f_κ in the dust nucleation zone at $r = 2.5 R_*$ as a function of the excitation period P in the case of model B. The perturbation force was taken as the sine of period P according to Eq. (2.28), whereas the amplitude was held at $\Delta u = 1.0 \text{ km s}^{-1}$.

The excitation frequency $f_p = 1/P$ itself and some of its harmonics are clearly recognisable for all periods P , whereas the determined eigenmodes f_κ are visible only for small excitation periods $P \lesssim 1250 \text{ d}$.

- **Irregular regime**

For small and intermediate excitation periods $P \lesssim 1250 \text{ d}$, the power spectra show a rather extended continuum with a number of distinct maxima. Some of these could be identified as eigenmodes of the CDS or as their harmonics. Also, the subharmonics $f_p/2$ and $f_p/3$ of the excitation frequency $f_p = 1/P$ show up. With increasing length of the excitation period P , the piston period and its harmonics become clearly recognisable. In contrast, the amplitude of the dust shell's eigenmode mostly decreases as P becomes larger.

- **Pulsation dominated regime**

For $P \gtrsim 1250 \text{ d}$, the CDS becomes finally enslaved by the excitation force, and the maximum at f_p becomes the predominant feature of the response spectra supplemented with an entire set of harmonics.

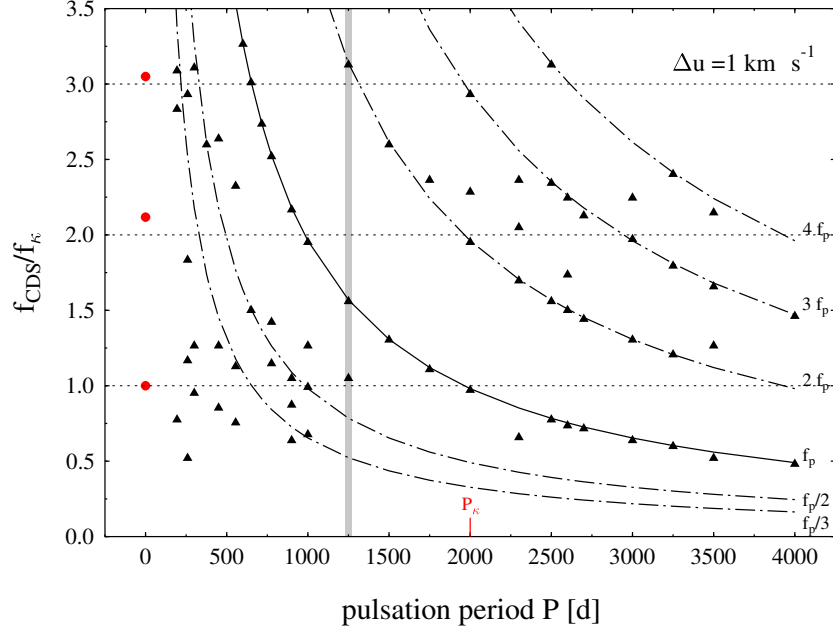


Figure 5.5: Most dominant frequencies of the CDS f_{CDS} related to the eigenmode $f_{\kappa} = 0.51 \cdot 10^{-3} \text{ d}^{-1}$ (triangles), periodically-disturbed with various stellar pulsation periods P but fixed amplitude $\Delta u = 1.0 \text{ km s}^{-1}$, near the dust nucleation zone $r = 2.50 R_*$. The set of eigenfrequencies are indicated by circles. The eigenperiod is labelled with P_{κ} . The excitation frequencies lie on the solid line and their harmonics on the dash-dotted lines. The grey line separates the irregular regime (left) from the pulsation dominated regime (right).

In general, the final velocity $\langle u_{\infty} \rangle$ has a rather high value with its maximum at $\langle u_{\infty} \rangle = 32 \text{ km s}^{-1}$ for $P = 600 \text{ d}$. With increasing period P , the velocity is continuously sloping downward to $\langle u_{\infty} \rangle = 19 \text{ km s}^{-1}$ at period $P = 4500 \text{ d}$. The corresponding mass loss rates show the same trend but with a steeper decline at $P = 1000 \text{ d}$ to $P = 1250 \text{ d}$. The maximum mass loss rate is $\langle \dot{M} \rangle = 1.8 \cdot 10^{-5} M_{\odot} \text{ yr}^{-1}$ for $P = 600 \text{ d}$. minimum $\langle \dot{M} \rangle = 2.6 \cdot 10^{-6} M_{\odot} \text{ yr}^{-1}$ for $P = 4500 \text{ d}$ (cf. Table 5.2).

Selected examples

Figure 5.6 demonstrates the basic behaviour of the shell in the nucleation zone at $r = 2.5 R_*$ for some selected monoprotic excitation periods $P = 376 \text{ d}$, 450 d and 716 d chosen from the irregular shell dynamics regime, respectively. The left panels display the power spectra of the local expansion velocity u by scaling to

Table 5.2: Resultant quantities from a CDS periodically disturbed with various stellar pulsation periods P but fixed strength $\Delta u = 1 \text{ km s}^{-1}$ such as frequency f_{CDS} , time averaged mass loss rate $\langle \dot{M} \rangle$, outflow velocity $\langle u_{\infty} \rangle$, and dust-to-gas mass ratio $\langle \rho_{\text{d}}/\rho_{\text{g}} \rangle$. Values in boldface indicate the strongest mode and underlined values the excitation frequency.

| P (d) | f_{CDS} (10^{-3} d^{-1}) | | | $\langle \dot{M} \rangle$ ($M_{\odot} \text{ yr}^{-1}$) | $\langle u_{\infty} \rangle$ (km s^{-1}) | $\langle \rho_{\text{d}}/\rho_{\text{g}} \rangle$ |
|------------|--|-------------|-------------|--|--|---|
| 0 | 0.51 | 1.13 | 1.50 | | | |
| 194 | 0.40 | 1.45 | 1.58 | $9.5 \cdot 10^{-6}$ | 27.5 | $3.1 \cdot 10^{-3}$ |
| 259 | 0.27 | 0.60 | 0.94 | $1.1 \cdot 10^{-5}$ | 26.4 | $3.8 \cdot 10^{-3}$ |
| 300 | 0.49 | 0.65 | 1.59 | $9.4 \cdot 10^{-6}$ | 25.6 | $3.5 \cdot 10^{-3}$ |
| 376 | 1.33 | <u>2.66</u> | 3.99 | $1.0 \cdot 10^{-5}$ | 26.4 | $4.1 \cdot 10^{-3}$ |
| 450 | 0.44 | 0.65 | 1.35 | $1.1 \cdot 10^{-5}$ | 25.8 | $3.9 \cdot 10^{-3}$ |
| 555 | 0.39 | 0.58 | 1.19 | $1.6 \cdot 10^{-5}$ | 26.2 | $4.1 \cdot 10^{-3}$ |
| 600 | <u>1.67</u> | 3.33 | 5.00 | $1.8 \cdot 10^{-5}$ | 31.8 | $4.2 \cdot 10^{-3}$ |
| 650 | 0.77 | <u>1.54</u> | 3.08 | $7.9 \cdot 10^{-6}$ | 28.9 | $4.2 \cdot 10^{-3}$ |
| 716 | <u>1.40</u> | 2.79 | 4.19 | $7.5 \cdot 10^{-6}$ | 26.8 | $4.2 \cdot 10^{-3}$ |
| 776 | 0.73 | <u>1.29</u> | 2.58 | $1.3 \cdot 10^{-5}$ | 27.5 | $3.5 \cdot 10^{-3}$ |
| 900 | 0.45 | 0.54 | <u>1.11</u> | $9.7 \cdot 10^{-6}$ | 25.2 | $3.2 \cdot 10^{-3}$ |
| 1000 | 0.35 | 0.51 | <u>1.00</u> | $1.7 \cdot 10^{-5}$ | 24.4 | $2.7 \cdot 10^{-3}$ |
| 1250 | 0.54 | 0.80 | 1.60 | $1.3 \cdot 10^{-5}$ | 26.3 | $4.2 \cdot 10^{-3}$ |
| 1500 | <u>0.67</u> | 1.33 | 2.00 | $5.0 \cdot 10^{-6}$ | 26.8 | $3.7 \cdot 10^{-3}$ |
| 1750 | <u>0.57</u> | 1.21 | - | $4.3 \cdot 10^{-6}$ | 25.7 | $4.1 \cdot 10^{-3}$ |
| 2000 | <u>0.50</u> | 1.00 | 1.17 | $3.8 \cdot 10^{-6}$ | 23.5 | $2.3 \cdot 10^{-3}$ |
| 2300 | 0.34 | 0.87 | 1.05 | $2.1 \cdot 10^{-6}$ | 23.1 | $2.6 \cdot 10^{-3}$ |
| 2500 | <u>0.40</u> | 0.80 | 1.20 | $1.8 \cdot 10^{-6}$ | 18.8 | $1.4 \cdot 10^{-3}$ |
| 2600 | <u>0.38</u> | 0.77 | 0.89 | $2.2 \cdot 10^{-6}$ | 18.4 | $1.9 \cdot 10^{-3}$ |
| 2700 | <u>0.37</u> | 0.74 | 1.09 | $3.1 \cdot 10^{-6}$ | 20.4 | $2.9 \cdot 10^{-3}$ |
| 3000 | 0.33 | 0.67 | 1.01 | $4.5 \cdot 10^{-6}$ | 20.4 | $2.7 \cdot 10^{-3}$ |
| 3250 | <u>0.31</u> | 0.62 | 0.92 | $3.6 \cdot 10^{-6}$ | 16.8 | $2.3 \cdot 10^{-3}$ |
| 3500 | <u>0.27</u> | 0.65 | 0.85 | $4.8 \cdot 10^{-6}$ | 18.1 | $1.9 \cdot 10^{-3}$ |
| 4000 | <u>0.25</u> | - | 0.75 | $2.6 \cdot 10^{-6}$ | 18.8 | $2.9 \cdot 10^{-3}$ |

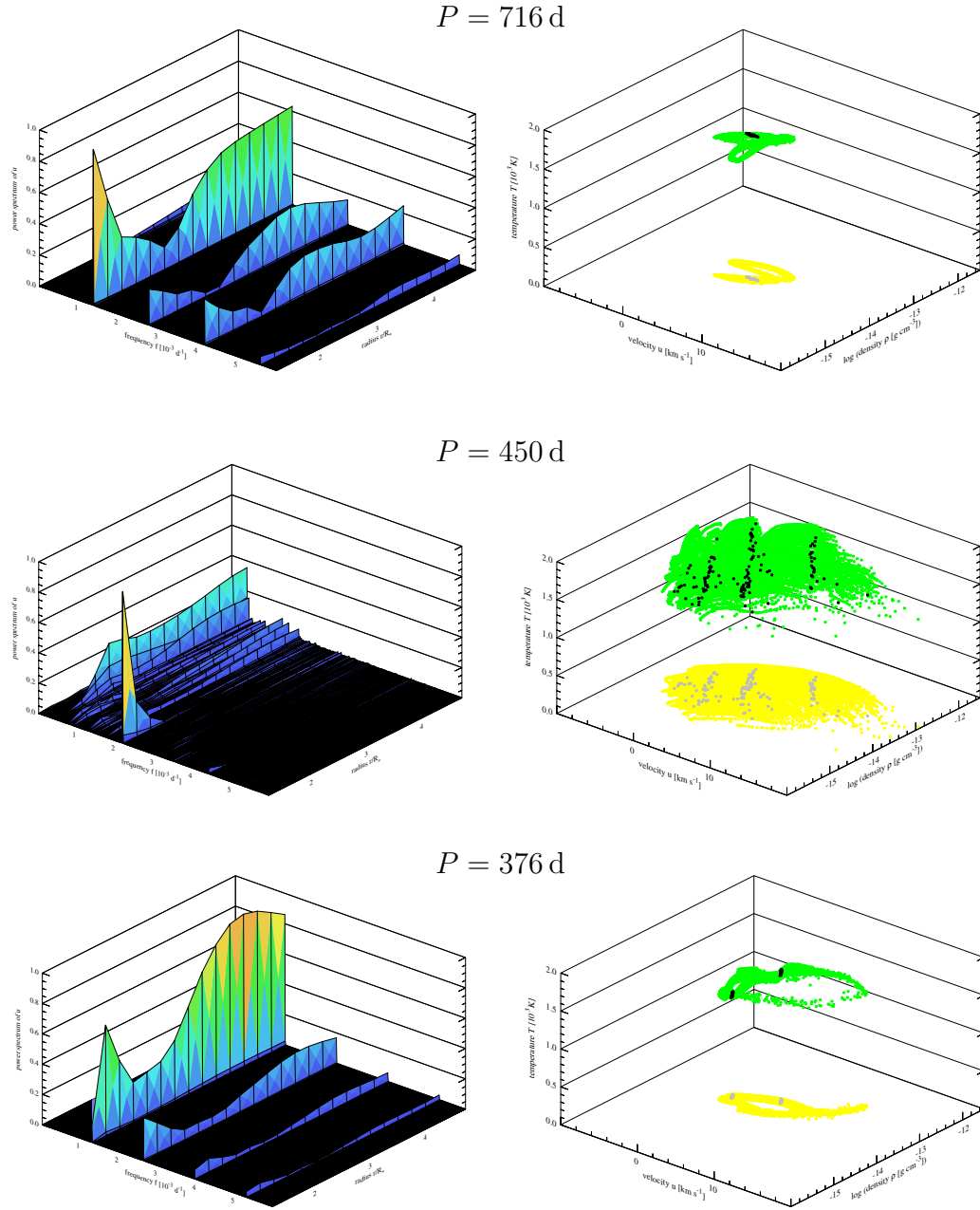


Figure 5.6: Power spectra of the local expansion velocity u (left panels) and corresponding maps of the (u, ρ, T) phase space (right panels) in the dust nucleation zone for different monoperoic excitation periods $P = 716$ d (upper), 450 d (middle), and 376 d (lower), respectively. The stroboscopic maps were obtained by sampling $[u(n0.02P), \rho(n0.02P), T(n0.02P)]$ (green) and the Poincaré maps by $[u(nP), \rho(nP), T(nP)]$ (black) for $1 \leq n \leq \lfloor t_{max}/P \rfloor$, $n \in \mathbb{N}$.

the actual strongest mode.

As can be seen in the uppermost and lowermost spectra, the CDS excited with the different periods $P = 716$ d and $P = 376$ d, reacts with the same dominant mode $f = 1.34 \cdot 10^{-3} \text{ d}^{-1} = (716 \text{ d})^{-1}$. The period of the CDS $P_{\text{CDS}} = nP$ appears as an integer multiple of the excitation period P . In the context of circumstellar shells this phenomenon is referred to as multiperiodicity. As indicated by the number of the black clusters in the stroboscopic maps, the system reacts monoperiodically (single black cluster, upper right panel, i.e. $n = 1$) for an excitation with $P = 716$ d, whereas the system's response is double-periodic (two black features in the lowermost plot on right, i.e. $n = 2$) for an excitation with $P = 376$ d. In other words, the system returns to the same state after a time interval $\Delta t = nP$. The corresponding curves in the (u, ρ, T) -hyper plane are restricted and closed. Nevertheless, some parts of the trajectory are passed through extremely rapidly, so that these parts are depicted by only a few points on the corresponding stroboscopic map.

For $P = 450$ d, as can be seen from the power spectra in the middle, left panel, the excitation period does not dominate the shell at the nucleation zone at $r \approx 2.5 R_*$. The amplitude of the piston frequency $f_p = 2.22 \cdot 10^{-3} \text{ d}^{-1}$ is weak and the frequency spectrum shows up with distinct maxima at $f = 0.44 \cdot 10^{-3} \text{ d}^{-1} \approx (2300 \text{ d})^{-1}$, which is characteristic of dynamical timescales of the CDS and $f = 1.35 \cdot 10^{-3} \text{ d}^{-1} \approx (740 \text{ d})^{-1}$ which seems to correspond to the somewhat-shifted feature $P = 716$ d providing the resonance case for this model. This is also consistent with the stroboscopic map given in the middle, right panel. In contrast to $P = 716$ d and 376 d, the system is not limited to a close trajectory in the (u, ρ, T) -space but rather completely fills out a continuous part of the phase space. However, again the dynamics of the shell seem to synchronise with the excitation period to some extent. For a constant phase angle ϕ of the stellar pulsation, i.e. $\Delta t = P$ (black dots), the system stays inside three, well-defined stripes which cut through the entire phase space area filled out by the system.

5.2.2 Perturbation strength

In this section, the above-mentioned model B is studied with regard to the response of the CDS for a sinusoidally moving piston with period $P = 376$ d, i.e. a typical oscillation period of Miras and LPVs, over sequence of varying amplitudes Δu . The amplitude starts with a value of $\Delta u = 1.0 \text{ km s}^{-1}$, so the disturbance is subsonic, and is then increased up to $\Delta u = 9.0 \text{ km s}^{-1}$ i.e. into the supersonic regime. Figure 5.7 depicts the most dominant CDS-frequencies related to the eigenfrequency f_{CDS}/f_κ at the nucleation zone at $r = 2.5 R_*$. The eigenmodes f_κ are depicted as filled circles.

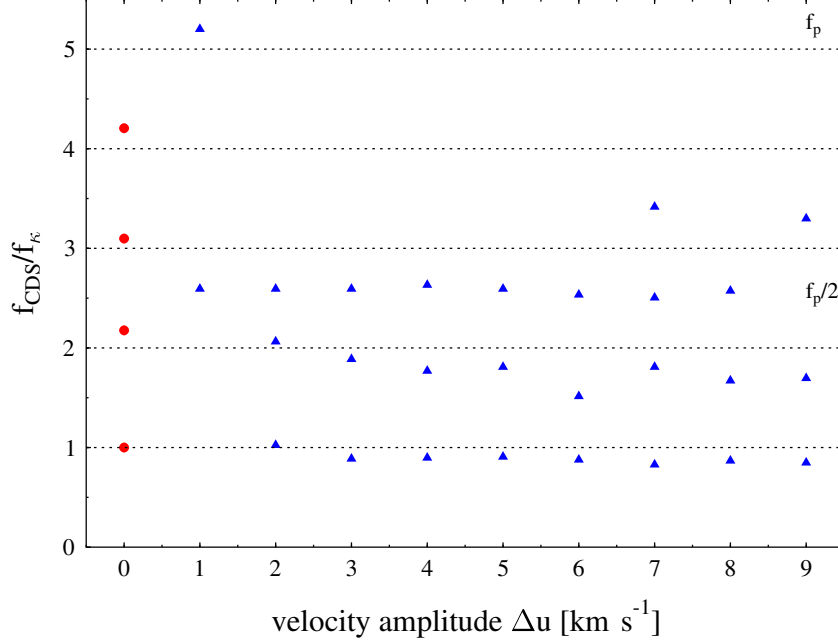


Figure 5.7: Most dominant frequencies of the CDS f_{CDS} related to the eigenmode $f_{\kappa} = 0.51 \cdot 10^{-3} \text{ d}^{-1}$ (triangles) excited with a fixed excitation period $P = 376 \text{ d}$, but different strengths Δu near the dust nucleation zone $r = 2.25 R_*$. The set of CDS eigenmodes is depicted by circles. The excitation frequency f_p and its first subharmonic $f_p/2$ are also marked.

The excitation frequency $f_p = (376 \text{ d})^{-1}$ itself is only noticeable for a small perturbation strength of $\Delta u = 1.0 \text{ km s}^{-1}$. Being weak in power it vanishes with increasing excitation strengths. The inertial envelope is not able to follow the short perturbation period. In fact, this mode does not at any time dominate the CDS dynamics. Actually, the first subharmonic of the excitation frequency $f_{p,-1} \approx (752 \text{ d})^{-1}$ dominates the dynamics. It can be regarded as the detuned second CDS-eigenmode. Subsequently the eigenmode at $f_{\kappa} \approx (2000 \text{ d})^{-1}$ takes over the dominance of the shell dynamics. In general, the CDS-eigenmodes are detuned towards lower frequencies (cf. Table 5.3) as already shown in the case of a CDS around a high luminous LPV (cf. Sect. 4.3.2). So, the first subharmonic of the perturbation frequency $f_p/2$ becomes to the second harmonic of the detuned CDS-eigenmode $2f_{\kappa}$.

The stellar pulsation leads to a levitation of the atmosphere, i.e. it lifts the material out of the gravitational field into the dust forming zone. With increasing strength of the pulsation amplitude Δu , the additional input of energy and momentum

leads to an enhanced density in the dust forming region and supports the dust formation than into accelerating the wind. Consequently, the stellar wind becomes far more massive and the mass-loss rate increases from $\langle \dot{M} \rangle = 1.0 \cdot 10^{-5} M_{\odot} \text{ yr}^{-1}$ for $\Delta u = 1 \text{ km s}^{-1}$ to $\langle \dot{M} \rangle = 7.4 \cdot 10^{-5} M_{\odot} \text{ yr}^{-1}$ for $\Delta u = 9 \text{ km s}^{-1}$ at nearly constant velocity (cf. Table 5.3). As the wind becomes more intense, the periodic depletion in dust-forming material also increases and it takes more time to re-enrich the nucleation zone. The result is a longer shell period as shown in Fig. 5.7.

Table 5.3: Resultant quantities of the excitation strength Δu study of model B for $P = 376 \text{ d}$: frequencies f_{CDS} , time averaged mass loss rate $\langle \dot{M} \rangle$, final outflow velocity $\langle u_{\infty} \rangle$, and dust-to-gas mass ratio $\langle \rho_{\text{d}} / \rho_{\text{g}} \rangle$. Values in boldface indicate the strongest mode, and underlined values refer to the excitation frequency.

| Δu (km s^{-1}) | f_{CDS} (10^{-3} d^{-1}) | | $\langle \dot{M} \rangle$ ($M_{\odot} \text{ yr}^{-1}$) | $\langle u_{\infty} \rangle$ (km s^{-1}) | $\langle \rho_{\text{d}} / \rho_{\text{g}} \rangle$ | |
|--------------------------------------|--|-------------|--|--|---|---------------------|
| 0.0 | 0.51 | 1.13 | 1.50 | | | |
| 1.0 | 1.33 | <u>2.66</u> | 3.99 | $1.0 \cdot 10^{-5}$ | 26.4 | $4.1 \cdot 10^{-3}$ |
| 2.0 | 0.53 | 1.06 | 1.33 | $3.8 \cdot 10^{-5}$ | 29.9 | $4.3 \cdot 10^{-3}$ |
| 3.0 | 0.46 | 0.88 | 1.33 | $2.5 \cdot 10^{-5}$ | 25.9 | $3.3 \cdot 10^{-3}$ |
| 4.0 | 0.47 | 0.90 | 1.35 | $8.5 \cdot 10^{-6}$ | 25.6 | $3.2 \cdot 10^{-3}$ |
| 5.0 | 0.47 | 0.93 | 1.33 | $2.1 \cdot 10^{-5}$ | 28.2 | $3.7 \cdot 10^{-3}$ |
| 6.0 | 0.46 | 0.79 | 1.30 | $4.1 \cdot 10^{-5}$ | 30.0 | $4.0 \cdot 10^{-3}$ |
| 7.0 | 0.43 | 0.93 | 1.29 | $1.9 \cdot 10^{-5}$ | 28.4 | $3.7 \cdot 10^{-3}$ |
| 8.0 | 0.45 | 0.86 | 1.33 | $1.2 \cdot 10^{-5}$ | 28.4 | $3.5 \cdot 10^{-3}$ |
| 9.0 | 0.44 | 0.87 | 1.69 | $7.4 \cdot 10^{-5}$ | 30.6 | $3.5 \cdot 10^{-3}$ |

Chapter 6

Lightcurves and dynamics

As already discussed, the cool, extended atmospheres of highly evolved stars on the Asymptotic Giant Branch favour the formation of dust particles. Due to radiation pressure on dust the matter is accelerated outwards. This high mass loss results in the formation of circumstellar envelopes. The dust in the inner shell absorbs the optical light of the central star and re-emits it at longer wavelengths in the infrared (IR)- and (sub)millimetre regime. That means, the energy emitted by the star is redistributed. For this reason circumstellar shells are principally observed by infrared and (sub)millimetre astronomy.

In this chapter calculated spectral energy distributions (SED) as well as synthetic lightcurves resulting from the shell models examined in the previous chapters are presented in order to provide the link with observations.

6.1 Frequency-dependent radiative transfer

In the dynamical calculations presented so far the radiative transfer problem was solved applying a grey, i.e. no frequency-dependence approximation. Clearly, such calculations cannot deliver information regarding the spectral energy distribution (SED) neither can they produce lightcurves of the CDS. Attaining such information requires the solution of the frequency-dependent stationary radiative transfer equation in spherical geometry for a given, radial structure of the CDS. This work has performed such calculations following the method presented by Winters et al. (1994, 1997). Based on the dynamical determined CDS structure, the frequency-dependent stationary radiative transfer equation in spherical geometry:

$$\mu \frac{\partial I_\nu}{\partial r} + \frac{1 - \mu^2}{r} \frac{\partial I_\nu}{\partial \mu} = \chi_\nu (B_\nu - I_\nu) \quad (6.1)$$

is solved. Since scattering by grains is neglected, the radiative transfer processes considered are grey absorption and thermal emission by the gas and frequency dependent absorption and thermal emission by the dust component:

$$\chi_\nu = \chi_\nu^g + \chi_\nu^d = \kappa^g + \kappa_\nu^d \quad . \quad (6.2)$$

The gas opacity is replaced by an averaged Rosseland mean gas opacity of $\kappa^g/\rho = 2 \cdot 10^{-4} \text{ cm}^2 \text{ g}^{-1}$. The dust opacity κ_ν^d is calculated in the small particle limit of Mie theory for spherical grains, i.e. the dust particles are assumed to be small compared to the relevant wavelength of the radiation field. According to Gail et al. (1984):

$$\kappa_\nu^d = \frac{8\pi^2 a_0^3}{\lambda} \Im \left(\frac{m(\nu)^2 - 1}{m(\nu)^2 + 2} \right) K_3 \quad (6.3)$$

where $a_0 = 1.28 \cdot 10^{-8} \text{ cm}$ is the hypothetical radius of a carbon monomer and K_3 is the third moment of the size distribution function $f(N, t)$ which is obtained by the degree of condensation f_{cond} via Eq. (2.23). The frequency-dependent complex refractive index $m(\nu)$ was taken from Maron (1990) and Preibisch et al. (1993) and are appropriate for pure amorphous carbon grains. The result of this calculation is the frequency-dependent radiation field at a given instant of time t .

6.2 Spectral energy distribution

Figure 6.1 displays the calculated, theoretical emergent spectra as produced by a CDS excited by a sinusoidally-moving piston which is varying in strength and period for model A, as described in Sect. 4.2. The SEDs are shown at maximum phase of the stellar luminosity for wavelengths in the $1 - 1000 \mu\text{m}$ range. The outer boundary of the CDS is located at a distance of $40 R_* = 2.7 \cdot 10^{15} \text{ cm}$ from the central star.

The basic model of the discussion is CDS model A (solid line) dominated by the exterior κ -mechanism (Sect. 4.2). The energy distribution of the CDS, resembling a Planck function, is characterised by a maximum at $\lambda_{\text{max}} \approx 7 \mu\text{m}$ in the mid-IR region. This emergent radiation arises exclusively from the dust surrounding the central star. The position of the maximum on the lightcurve are related to the dust's temperature. Fitting the curve near its maximum according to the Wien's displacement law: $\lambda_{\text{max}} T = 2898 \mu\text{mK}$, one sees that the spectrum can be rather well-represented by a blackbody emitting at $T_{\text{bb}} = 414 \text{ K}$. However, it has to be noted that this is an approximation only, because the distribution of the dust is a smooth function of temperature T .

Figure 6.1 investigates the influence of the central star's pulsation period P (left panel) and strength Δu (right panel) on the SED. With increasing pulsa-

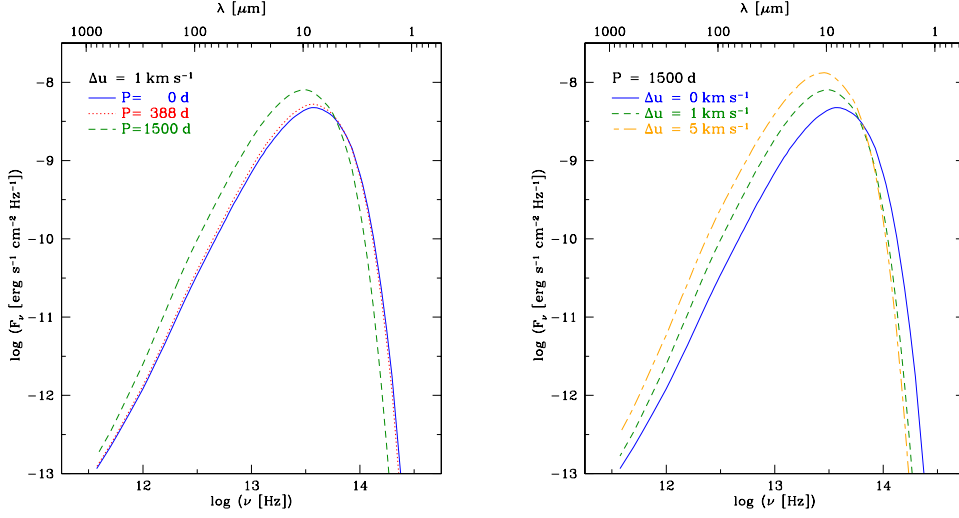


Figure 6.1: Comparison between the SEDs of the dust shell model A excited by different stellar pulsation periods P (left) and strengths Δu (right)

tion period P and excitation strength Δu , one sees that the maximum moves towards larger wavelengths while basically keeping the overall structure (Planck shape). This means that the part of the CDS contributing to the spectrum becomes cooler. This result is interpreted as follows: as can be seen from Table 4.1, a CDS excited with $P = 388 \text{ d}$, $\Delta u = 1 \text{ km s}^{-1}$ (dotted line) produces approximately the same mass loss $\langle \dot{M} \rangle$ and outflow velocity $\langle u_\infty \rangle$ as an undisturbed CDS $P = 0 \text{ d}$, $\Delta u = 0 \text{ km s}^{-1}$ (solid line). The CDS is dominated by its eigenmode as determined by the exterior κ -mechanism, and the spectra for the afore-mentioned two cases are almost identical. With increasing excitation the shell develops a higher mass loss $\langle \dot{M} \rangle$ (cf. Tables 4.1 and 4.3). At approximately the same outflow velocity $\langle u_\infty \rangle$ this results in a higher total mass density according to the mass conservation equation. Since the dominant size of grains formed in these CDSs is found to be constant at $a \approx 0.2 \mu\text{m}$ and the ratio of the dust-to-gas mass density $\langle \rho_d / \rho_g \rangle$ remains nearly constant, the dust particle density has to rise. The envelope becomes more opaque because the radiation is efficiently absorbed by more dust grains. Due to the increased dust opacity the emergent spectra become cooler.

6.3 Synthetic lightcurves

Figure 6.2 presents synthetic lightcurves for model A obtained for various excitation periods P and strengths Δu at several representative wavelengths. From the left to the right the lightcurves are depicted firstly for no external excitation, i.e. $P = 0$ d, $\Delta u = 0$ km s⁻¹, secondly with excitation $P = 388$ d, $\Delta u = 1$ km s⁻¹, thirdly $P = 1500$ d, and fourthly $\Delta u = 1$ km s⁻¹ and $P = 1500$ d, $\Delta u = 5$ km s⁻¹.

From top to bottom the plots display in the uppermost panels the temporally variation of the stellar luminosity and in the second panels the lightcurves for $\lambda = 2.3$ μ m representing the hot, left hand side of the SED. The third and fourth panels depict the lightcurves for $\lambda = 7.0$ μ m and $\lambda = 10.5$ μ m both wavelengths lying around the SED-maxima and finally, the lowermost panels picture the lightcurves for $\lambda = 102$ μ m representing the cool, right hand side of the spectra.

The lightcurves in the first and the last panels show monoperoiodic behaviour but with differing periods. For the undisturbed CDS ($P = 0$ d, $\Delta u = 0$ km s⁻¹) the dominant timescale is the dust formation scale, which is roughly identical with the CDS-eigenperiod $P_\kappa = 2450$ d (left panels). In the case of the highly-excited model ($P = 1500$ d, $\Delta u = 1$ km s⁻¹), it is the hydrodynamical timescale determined by the stellar pulsation period which dominates the CDS dynamics (right panels). The curves in the second panels are obtained by an excitation of the CDS with a stellar pulsation period of $P = 388$ d, $\Delta u = 1$ km s⁻¹. Nevertheless, the dominant time scale still remains the dust formation timescale. The eigenperiod of the CDS $P_\kappa = 2450$ d and the hydrodynamical period $P = 388$ d interfere with each other. Formation of new dust layers take place during approximately every seventh period of the hydrodynamical cycle which corresponds to a slightly shifted eigenperiod $P_\kappa \approx 2700$ d. See also Table 4.2. The lightcurves in the third panels ($P = 1500$ d, $\Delta u = 1$ km s⁻¹) show double-periodic behaviour, i.e. a new dust layer is formed every second pulsation period. The eigenperiod is detuned to the first harmonic of the hydrodynamic period $P_\kappa = 2P = 3000$ d (cf. Table 4.3). In general, the luminosity curves resemble the lightcurve for λ_{\max} of the SED and underlines the contribution of this wavelength to the total emergent energy (cf. Fig. 6.1 and Fig. 6.2).

The stellar luminosities in the uppermost panels show a somewhat surprising temporal variation, visible for the unexcited shell model in the left panel especially. Though there is no internal excitation by stellar pulsation the luminosity develops a nonharmonic time-dependent variation. This is due to the nonlinear processes in the dust shell, which by modelling procedure influence the physical quantities also including the resulting values for the stellar luminosity and the stellar radius.

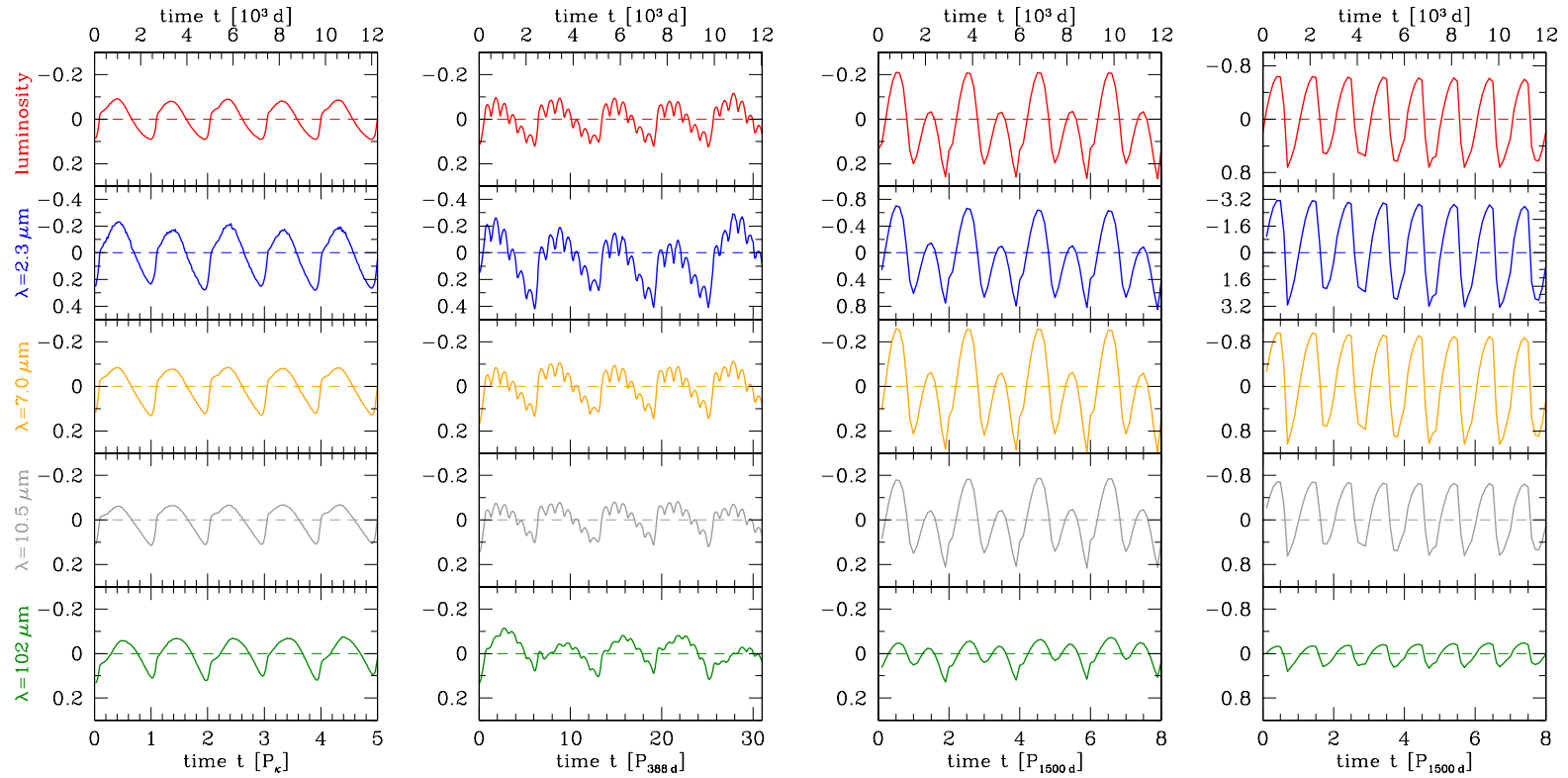


Figure 6.2: Synthetic lightcurves in magnitudes related to the mean magnitude of model A for various excitations at different wavelengths. *Left panels:* without external excitation i.e. $P = 0$ d, $\Delta u = 0$ km s $^{-1}$, and with excitation *second panels* $P = 388$ d, $\Delta u = 1$ km s $^{-1}$, *third panels:* $P = 1500$ d, $\Delta u = 1$ km s $^{-1}$ and *last panels:* $P = 1500$ d, $\Delta u = 5$ km s $^{-1}$. Note the different scaling of the ordinate.

The synthetic lightcurves of the less luminous CDS model B at different wavelength are shown in Fig. 6.3 for two different excitations $P = 376$ d, $\Delta u = 1$ km s⁻¹ (left panels) and $P = 716$ d, $\Delta u = 1$ km s⁻¹ (right panels). In addition, the uppermost panels show the stellar luminosity of the models.

For an excitation with period $P = 716$ d the shell reacts strictly sinusoidally with the stellar perturbation frequency (left panels). In the case of a short perturbation period of $P = 376$ d the shell reaction is highly complex. The stellar luminosity (upper left panel) exhibits a double-periodic variation with period $P = 376$ d and $2P \approx 752$ d initiated by the stellar pulsation. The long-term modulation in the synthetic lightcurves seen at all wavelengths is remarkable, because it is purely caused by dust formation in the envelope. The period can be determined to $P_\kappa \approx 8000$ d and corresponds to the first harmonic of the fundamental CDS-eigenmode (cf. Table 5.1). In fact the model is multi-periodic. Note further, on moving to longer wavelengths there is a phase shift in the behaviour of the synthetic lightcurves. This maybe indicates that the mean temperature of the dust visible in these lightcurves changes with time.

To sum up, the calculated lightcurves reflect the complex CDS dynamics, which can be conceived as superposition of various oscillations with periods of the internal pulsation and periods determined by time scale of the dust formation process. A comparison between the lightcurves of model A excited with $P = 388$ d (Fig. 6.2) and model B excited with $P = 376$ d (Fig. 6.3) yields no clear difference. Both models exhibit a long-term variation determined by the dust formation process and a short hydrodynamic timescale which interfered with each other. However, the only difference is the length of the dust formation timescale, which is in the case of model B ($P_\kappa \approx 8000$ d) almost three times longer than for model A ($P_\kappa \approx 2700$ d). The same reasoning can be applied to the mono-periodically reacting shell models A ($P = 1500$ km s⁻¹, $\Delta u = 5$ km s⁻¹) and B ($P = 716$ d, $\Delta u = 1$ km s⁻¹).

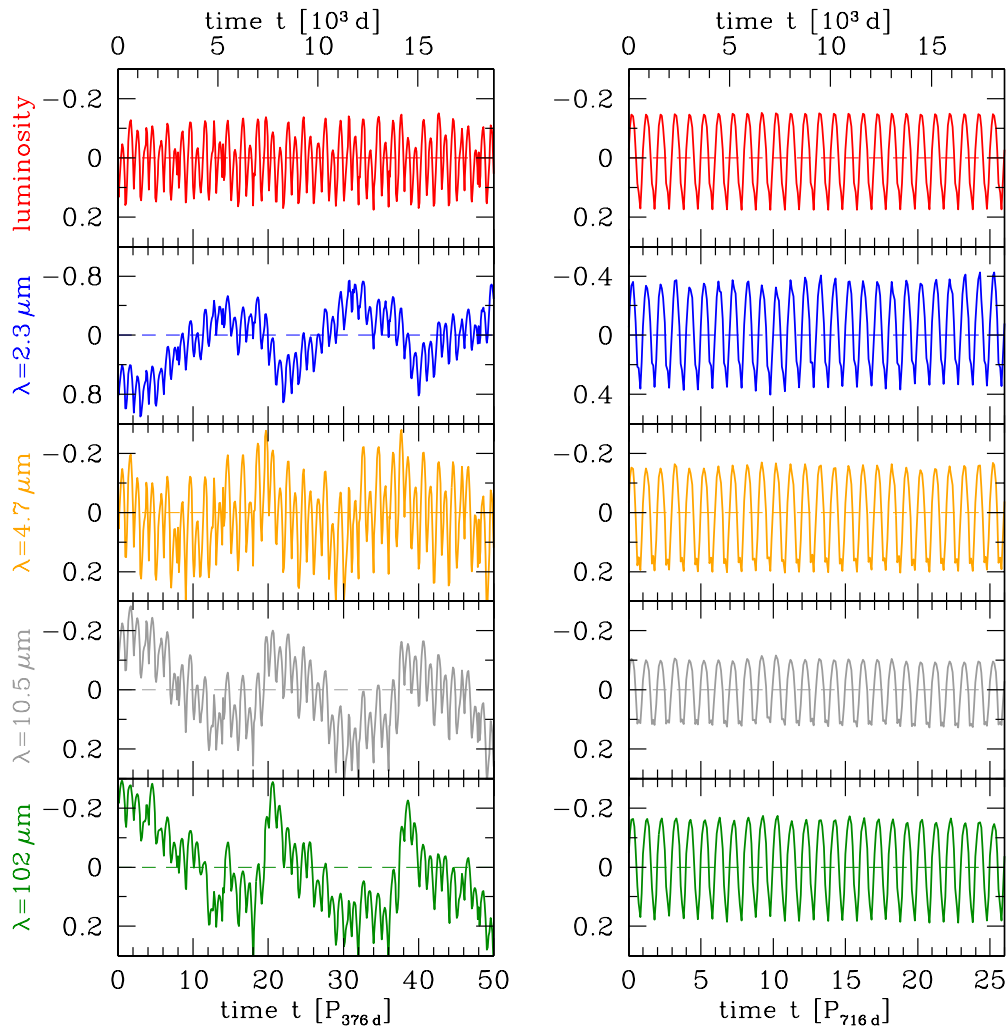


Figure 6.3: Synthetic lightcurves in magnitudes related to the mean magnitude of model B for various excitations at different wavelengths. *Left panels:* $P = 376$ d, $\Delta u = 0$ km s $^{-1}$. *Right panels:* $P = 716$ d, $\Delta u = 1$ km s $^{-1}$. Note the different scaling of the ordinate.

Chapter 7

Special application: IRC +10216

IRC +10216^a probably the best known and most studied carbon star, was first noted by Becklin et al. (1969) to be a bright, unusual source. It is the nearest carbon star known at distance $d \approx 110 - 150$ pc (Crosas & Menten (1997), Groenenwegen et al. (1998)). The central star, being embedded in a thick dust envelope created by a powerful mass loss rate, disappears almost completely in the optical range. The dust in the inner shell absorbs the optical light of the central star and re-emits it mostly at infrared wavelengths. So, the star is one of the brightest near- and mid-infrared sources at wavelengths around $10 \mu\text{m}$ (Le Bertre (1987)). It is regarded as a prototype of an extreme carbon star and classified as spectral type C 9.5 (Olofsson et al. (1982)). The coordinates^b of the infrared source are:

$$\alpha(2000) : 09^{\text{h}} 47^{\text{m}} 57.^{\text{s}}38 \quad \delta(2000) : +13^{\circ} 16' 43.''63$$

in the Leo constellation. It has been the object of several observation programs in the near infrared and radiowave regime. Its period is quoted to 633 – 650 d (e.g. Witteborn et al. (1980); Ridgway & Keady (1988); Dyck et al. (1991); Weigelt et al. (1998)). The mass loss rate has been determined to be $\dot{M}_{\text{obs}} = 9 \cdot 10^{-5} M_{\odot} \text{yr}^{-1}$ (Men'shchikov et al. (2001)), the outflow velocity to be $u_{\text{obs}} = 14 - 15 \text{ km s}^{-1}$ (Loup et al. (1993) and Olofsson et al. (1993)) and the dust-to-gas mass ratio to $(\rho_{\text{d}}/\rho_{\text{g}})_{\text{obs}} = 1.3 \cdot 10^{-4}$ (Knapp (1985)). In order to reproduce specific lightcurves and spectra observed by Le Bertre (1992), dynamical model calculations were performed by Winters et al. (1996). Thereby the following set of fundamental parameters was found:

^aalso known as CW Leo or RAFGL 1381

^bReference: SIMBAD - <http://simbad.u-strasbg.fr>

$$\begin{aligned}
L_* &= 2.4 \cdot 10^4 L_\odot & P &= 650 \text{ d} \\
M_* &= 1 M_\odot & \Delta u &= 6.0 \text{ km s}^{-1} \\
T_* &= 2500 \text{ K} & R_0 &= 0.91 R_* \\
C/O &= 1.2
\end{aligned}$$

is capable of explaining several different observations of the IRC +10216. In this chapter, this parameter set is subjected to an analysis with respect to the dynamical behaviour of the star-surrounding envelope.

7.1 Eigendynamics

As presented in the parameter study in Sect. 4.4, the development of a CDS by the exterior κ -mechanism is linked to limit values of the individual stellar parameters. For instance, the limit luminosity seems to be at approximately $2.5 \cdot 10^4 L_\odot$ in the case of carbon to oxygen abundances $C/O = 1.25$ and temperature $T = 2450 \text{ K}$. So, in the case of the IRC +10216, a model with a luminosity of $2.4 \cdot 10^4 L_\odot$ does not have the ability to develop a CDS driven by the exterior κ -mechanism. Consequently, in order to initiate a CDS-generating mass loss an additional mechanical support is necessary. This mechanical support is chosen to be stochastic (Sect. 2.2.3) to reduce the influence of the newly introduced timescale. To determine the eigenperiod of such a generated CDS, the investigation follows the approach presented in Sect. 5.1 for CDSs around standard and low luminous AGB-stars.

Sequences having up to 24 realisations of various stochastic excitation strengths σ were executed and subjected to a Fourier Analysis. The time-averaged derived quantities describing the wind are listed in Table 7.1 for strengths $\sigma = (0.1 \text{ to } 2.0) \text{ km s}^{-1}$. The eigenmodes f_κ were detected at the dust nucleation zone at $r \approx 2.5 R_*$. Figures 7.1 and 7.2 present the overall power spectra and some selected profiles of the stochastic excited inner parts of the CDS with strength $\sigma = 0.5 \text{ km s}^{-1}$ and $\sigma = 2.0 \text{ km s}^{-1}$. For small excitations $\sigma = (0.1, 0.5) \text{ km s}^{-1}$ the spectra are rich in details. With increasing distance from the star the dominant frequencies move towards smaller frequencies. Finally, the CDS shows its final dynamics with onset of the dust nucleation at $r \approx 2.5 R_*$. The fundamental mode is determined to be $f_\kappa \approx 0.13 \cdot 10^{-3} \text{ d}^{-1} \approx (8000 \text{ d})^{-1}$. That high eigenperiod is in reasonable agreement with the C/O -study in Sect. 4.4.2. This study revealed, that the CDS-eigenfrequency f_κ is mainly determined by the abundances of the dust forming elements, i.e. by the carbon abundances ϵ_C . With decreasing C/O -ratio the eigenfrequency f_κ decreases monotonically.

For high excitation strengths $\sigma = (1.0, 2.0) \text{ km s}^{-1}$ the shells response strictly

Table 7.1: List of model calculations with stochastic excitation for IRC +10216 model. Given are the excitation strength σ , the number of ensemble members No. and resultant quantities such as: ensemble averaged CDS-eigenmodes f_κ of the dust forming zone at $r = 2.5 R_*$, time averaged mass loss rate $\langle \dot{M} \rangle$, outflow velocity $\langle u_\infty \rangle$, and dust-to-gas mass ratio $\langle \rho_d / \rho_g \rangle$

| σ (km s^{-1}) | No. | f_κ (10^{-3} d^{-1}) | $\langle \dot{M} \rangle$ ($M_\odot \text{ yr}^{-1}$) | $\langle u_\infty \rangle$ (km s^{-1}) | $\langle \rho_d / \rho_g \rangle$ | | | |
|------------------------------------|-----|--|--|--|-----------------------------------|---------------------|---------------------|---------------------|
| 0.1 | 24 | 0.13 | 0.33 | 0.60 | $4.8 \cdot 10^{-7}$ | 0.7 | $5.1 \cdot 10^{-4}$ | |
| 0.5 | 23 | 0.12 | 0.23 | 0.31 | 0.58 | $7.3 \cdot 10^{-7}$ | 1.1 | $4.0 \cdot 10^{-4}$ |
| 1.0 | 21 | 0.24 | 0.49 | 0.73 | $9.9 \cdot 10^{-6}$ | 4.3 | $3.9 \cdot 10^{-4}$ | |
| 2.0 | 23 | 0.29 | 0.59 | 0.87 | $4.6 \cdot 10^{-6}$ | 4.5 | $4.5 \cdot 10^{-4}$ | |

periodic and the spectra resemble those of a CDS which is dominated by the exterior κ -mechanism. A set of overtones is clearly apparent (cf. Fig. 7.2 lower panels). The dominant mode has changed to the slightly off-tuned first overtone of the eigenfrequency $2f_\kappa \approx 0.24 \cdot 10^{-3} \text{ d}^{-1} \approx (4100 \text{ d})^{-1}$.

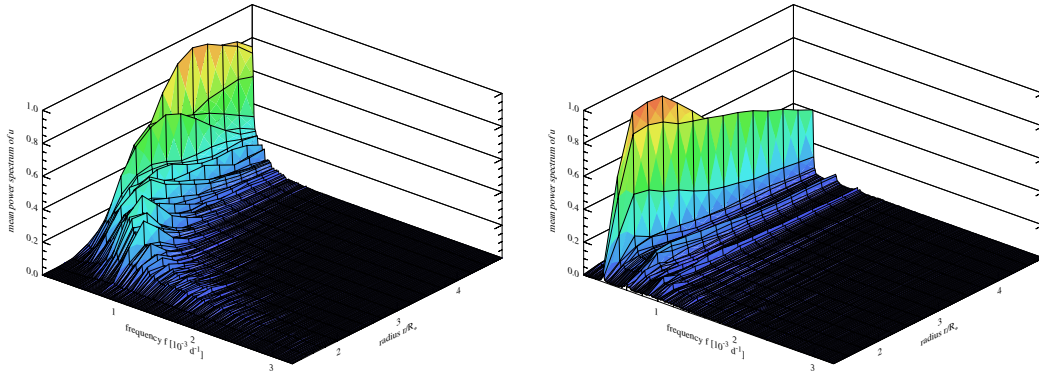


Figure 7.1: Normalised mean power spectra of the radial gas velocity u of the IRC +10216 model caused by stochastic excitation of strength $\sigma = 0.5 \text{ km s}^{-1}$ (left) and $\sigma = 2.0 \text{ km s}^{-1}$ (right).

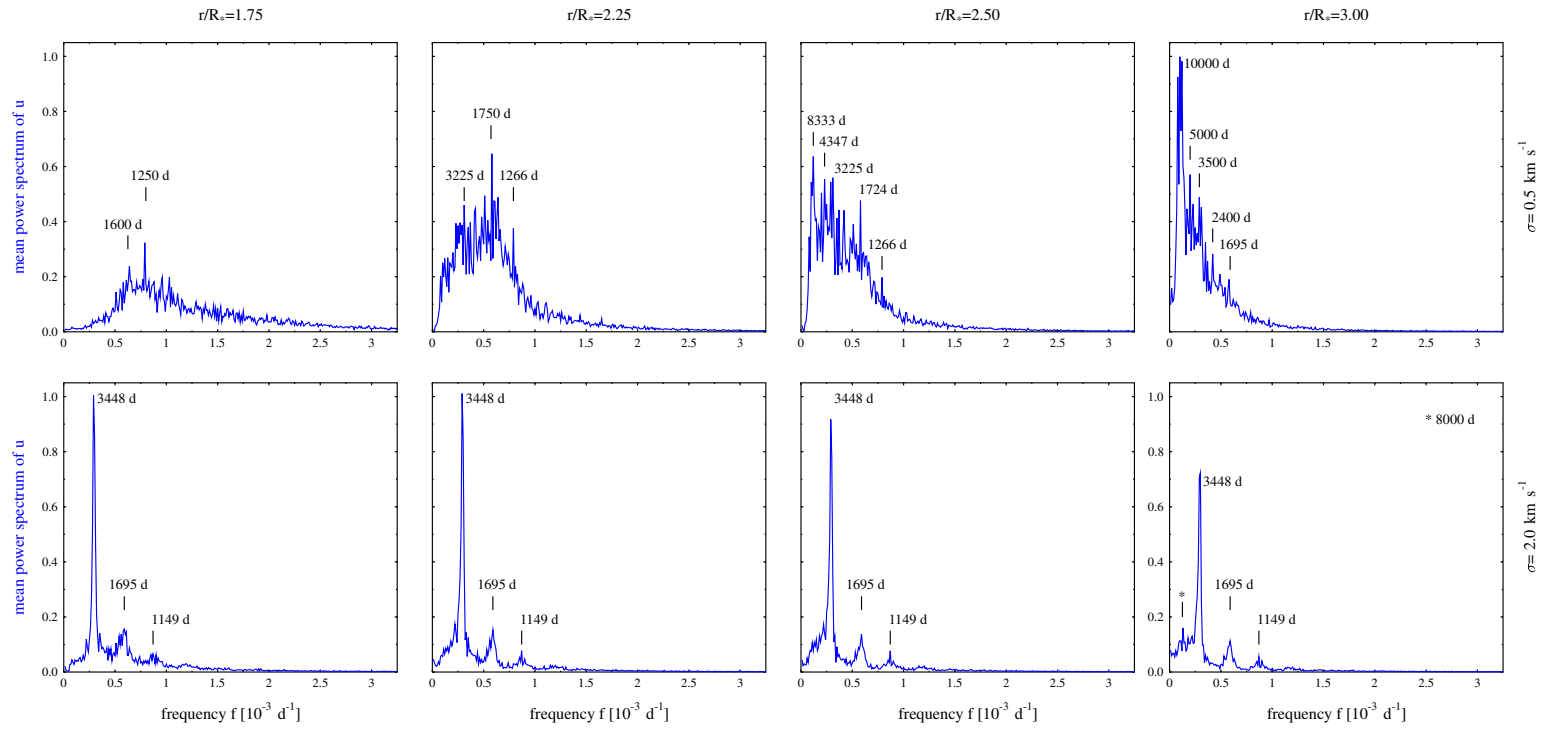


Figure 7.2: Selected mean power spectrum profiles of the gas velocity u at various radii for noise intensities $\sigma = 0.5 \text{ km s}^{-1}$ (upper panels), and $\sigma = 2.0 \text{ km s}^{-1}$ (lower panels) respectively.

7.2 Monoperiodic excitation

Observations of IRC +10216 imply a well defined pulsation period of approximately $P = 650$ d. Thus, the model was now excited monoperiodically.

As can be seen in the power spectrum in Fig. 7.3 left the CDS dynamics is composed of different oscillations. The stellar pulsation frequency $f_p = 1.54 \cdot 10^{-3} \text{ d}^{-1} \approx (650 \text{ d})^{-1}$ and its first harmonic $f_p = 3.08 \cdot 10^{-3} \text{ d}^{-1} \approx (325 \text{ d})^{-1}$ are recognisable at the inner part of the CDS. They are only able to dominate the CDS dynamics close to the star up to $r \lesssim 2 R_*$. Shortly thereafter, the frequencies rapidly diminish and disappear at $r \approx 3 R_*$, where dust formation occurs. Simultaneously the frequency $f_{\text{CDS}} = 0.26 \cdot 10^{-3} \text{ d}^{-1} \approx (3900 \text{ d})^{-1}$ controlled by the time scale of the dust formation process gains strength. Its minimum indicates the dust nucleation zone at $r \approx 3 R_*$. Further noticeable frequencies are the overtones $f_{\text{CDS}} = 0.52 \cdot 10^{-3} \text{ d}^{-1} \approx (1900 \text{ d})^{-1}$, $f_{\text{CDS}} = 0.78 \cdot 10^{-3} \text{ d}^{-1} \approx (1300 \text{ d})^{-1}$ although these are smaller in magnitude.

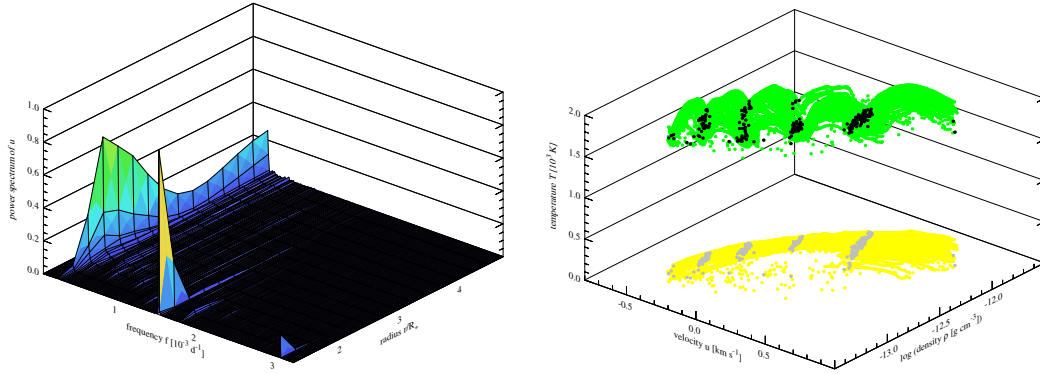


Figure 7.3: Normalised power spectrum of velocity u (left) and maps of the (u, ρ, T) -phase space (right) of the periodically excited IRC +10216 model.

The corresponding Poincaré map (Fig. 7.3 right) shows four clearly distinct stripes (black). A resonance such as in the case of the previously studied models A and B could not be found (cf. Sect 4.3.1 and Sect. 5.2.1). Further results of the analysis suggest:

$$\begin{aligned} \langle \dot{M} \rangle &= 1.3 \cdot 10^{-4} M_{\odot} \text{ yr}^{-1} \\ \langle u_{\infty} \rangle &= 12.4 \text{ km s}^{-1} \\ \langle \rho_d / \rho_g \rangle &= 8.2 \cdot 10^{-4} \end{aligned}$$

The above suggests that the mass loss rate, the final outflow velocity as well as the

dust-to-gas mass ratio are in good agreement with the observed properties of IRC +10216 (cf. p. 89).

7.3 Spectra & lightcurves

Figure 7.4 compares the SED resulting from the model calculations (solid line) and specific observed photometric data of IRC +10216 (symbols) in the infrared range of $(1 - 800) \mu\text{m}$ at the maximum phase of luminosity. The corresponding observation data were obtained by Le Bertre (1987), Campbell et al. (1976), Sahai et al. (1989), Sopka et al. (1985), and Walmsley et al. (1991). The synthetic emergent spectrum was attained from an envelope extended up to a distance of $60 R_* = 3.4 \cdot 10^{15} \text{ cm}$ from the central star.

The stellar luminosity L_* , which is an input parameter of the model, can be used to estimate the distance to IRC +10216. Since this star is located outside the galactical plane in a region clear of gas and dust, the distance can be reasonably estimated by neglecting the interstellar extinction (Le Bertre et al. (1995)) i.e. assuming only geometrical dilution of the radiation energy:

$$d = R_{\text{out}} \left(\frac{F_{\nu, \text{calc}}(R_{\text{out}})}{F_{\nu, \text{obs}}(d)} \right)^{1/2} \quad (7.1)$$

This yields a distance of $d \approx 100 \text{ pc}$, which is in satisfying agreement with observations (cf. p. 89).

Figure 7.4 suggests that whereas the near infrared regime (NIR) $\lambda = (1 - 5) \mu\text{m}$ and the mid infrared regime (MIR) $\lambda = (5 - 25) \mu\text{m}$ are well reproduced, the theoretical SED of the IRC model somewhat under-estimates the flux at the far infrared regime (FIR) $\lambda \geq 25 \mu\text{m}$. This is probably due to the location of the outer boundary at only $60 R_* = 3.4 \cdot 10^{15} \text{ cm}$ away from the star. An increase of the shell extension leads to an increase of the FIR flux of the calculated spectrum, because thermal emission of cool dust located at larger distance from the central star contributes significantly to the emergent flux at FIR wavelengths (cf. Winters et al. (1994)). A better reproduction of the FIR spectrum of IRC +10216 would be obtained for an outer boundary shell radius of approximately $3 \cdot 10^{17} \text{ cm}$. This corresponds to a source diameter of $6'$ at a distance of 110 pc (Menten et al. (2006)). Such a value, however is beyond the CPU-requirements of the current model.

Also notable in Fig. 7.4 is the oversteep decrease of the synthetic spectrum at wavelengths $\lambda \leq 1 \mu\text{m}$ compared to the observations. IRC +10216 is known to have an asymmetric, clumpy dust shell structure probably caused by variations

in mass loss (see e.g. Weigelt et al. (1998), Osterbart et al. (2000)). Changes in the optical depth result in an enhanced escape of stellar radiation, which could be the reason for the large observed flux in this regime. Fitting a Planck shaped curve to the right flank suggests that the temperature of the hottest grains is around $T_d \approx 850$ K.

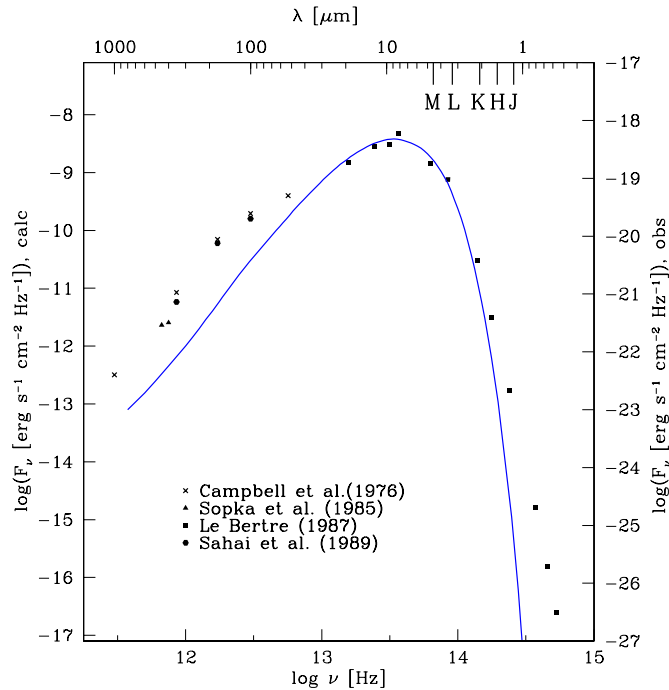


Figure 7.4: Comparison between calculated (solid line) and observed (symbols) SED of IRC +10216 at the maximum phase of the luminosity

Figure 7.5 shows the calculated temporal variation of the stellar luminosity in the uppermost panel and the comparison between specific observations in various photometric NIR standard bands such as J($\lambda_{\text{eff}} = 1.24 \mu\text{m}$), H($\lambda_{\text{eff}} = 1.63 \mu\text{m}$), K($\lambda_{\text{eff}} = 2.19 \mu\text{m}$), L($\lambda_{\text{eff}} = 3.79 \mu\text{m}$), and M($\lambda_{\text{eff}} = 4.64 \mu\text{m}$) (points) and corresponding synthetic lightcurves (solid lines) of IRC +10216. The observed data were taken from monitoring in the range of $1 - 20 \mu\text{m}$ based on Le Bertre (1992). One sees a good comparison between model (lines) and observed data (points) at the lower wavelengths correspond to the hot innermost CDS edge (e.g. consider second from top figure at $\lambda = 1.21 \mu\text{m}$) with regard to the magnitude. However, on moving to higher wavelengths, the model increasingly underestimates the data. This probably arose, because of the location of the outer model boundary. Regarding the CDS-dynamics, the stellar pulsation period $P = 650$ d can be decisively seen in all photometric bands. An additional cycle of 6 times the stellar

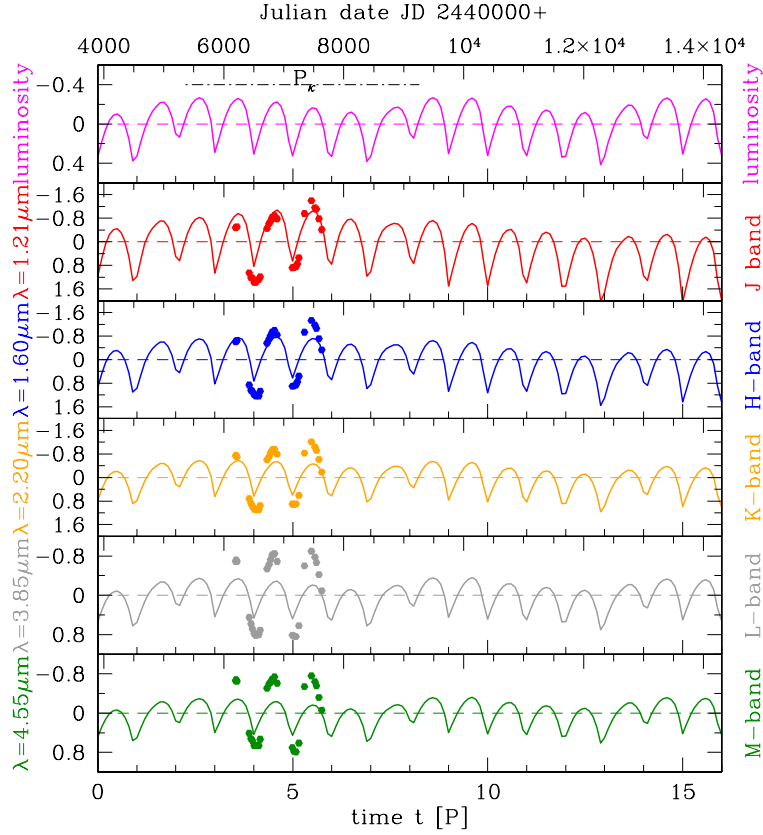


Figure 7.5: Synthetic lightcurves of the dust shell model (solid lines) at different wavelengths over a time interval of 16 pulsation periods and observed lightcurves of IRC +10216 (points) by Le Bertre (1992). The lightcurves are plotted in magnitudes related to the mean magnitude. Note the different scaling of the ordinate at different wavelengths. The CDS-eigenperiod P_{κ} is marked with a dashed-dotted line.

pulsation period is also visible (dashed-dotted line). This is the dust-determined eigenperiod of the CDS $P_{\kappa} \approx 3900$ d. The observation data well reproduce the short hydrodynamic period determined by the stellar pulsation, but cannot reproduce the long envelope period. This is due to the short observation period of $t \approx 1400$ d. Nevertheless, one sees a continuous upward trend of the observation data in the J, H and K-band (see Fig. 7.5 second to fourth panel). This can be regarded as hint for the underlying shell-determined period. For a confirmation, long term observations are necessary.

Chapter 8

Summary & outlook

This work has investigated the dynamics of carbon-rich circumstellar dust shells (CDSs) surrounding low and intermediate mass stars in their late evolutionary state. The main focus lies on the interplay between the stellar radiation and the dust complex and their influence on the resulting shell dynamics. For that purpose CDSs were considered as oscillatory systems, whose dynamics are influenced by the presence of dust. A quantitative analysis of the structure and the dynamical behaviour of CDSs both in frequency and in phase space has been presented.

It was found that there exist basically two different classes of CDS with respect to the dynamic behaviour:

- CDSs around high luminous stars are able to build up a self-induced and sustaining oscillation due an effect called the exterior κ -mechanism. The dynamics of the shell are dominated by its eigenmode, which is given by the characteristic dynamical time scales of the dust formation.
- In the case of lower stellar luminosities the system generates no self-induced shocks by the exterior κ -mechanism. Therefore, the eigenmodes of the system cannot be determined directly. In order to determine the eigendynamics the system has to be supplied by additional energy and momentum. This was achieved by introducing a force which is regarded to be stochastic such as e.g. produced by convective red giant atmospheres. The purpose is to supply enough energy to initiate a CDS generating mass loss, i.e. stellar wind but also to prevent or to minimise the influence on the CDS's eigendynamics.

In addition to this a parameter study investigated the dependence of the exterior κ -mechanism determined CDS-eigenperiod on stellar parameters. The decisive influence of the carbon-to-oxygen ratio C/O on the eigenmode was thus

highlighted. With an increasing ratio the eigenfrequency becomes larger.

Once a set of eigenmodes has been determined, the interaction between these normal modes and a monoprotic, sinusoidal perturbation provided by stellar pulsation via the so-called interior κ -mechanism has been investigated. When externally excited, the response of the envelope depends strongly on the period P of the excitation. The CDSs show distinct dynamics regimes:

- Eigenmode dominated regime:
is connected to short and intermediate perturbation periods, i.e. periods which are typical pulsation periods for a Miras type star ($100 \text{ d} \leq P \leq 1000 \text{ d}$). The prominent modes are the CDS-eigenmodes and its harmonics, which become somewhat detuned with increasing perturbation period. The inertial envelope is not able to follow the perturbation period.
- Irregular regime:
also covers the range of short and intermediate periods. It is dominated by eigen- and perturbation modes as well as modes associated to neither of the above.
- Pulsation dominated regime:
appears for large pulsation periods in the range of the dust formation time scale of several 1000 days. The regime is dominated by stellar pulsation modes and its harmonics.

Whereas in the case of CDSs around high luminous LPVs, all three dynamical regimes were evident, in the case of lower luminosities an eigenmode dominated regime does not exist. This is due to the fact that the input of energy and momentum is necessary for the evolution of a CDS .

For both classes of CDSs it is possible to apply a resonance condition. This means that the ratio of the stellar pulsation period to the CDS's eigenperiod is given as a ratio of two integers.

In order to provide the link between numerical results and observations, frequency-dependent radiative transfer calculations have been performed on the basis of the previously obtained synthetic envelope structure. The resulting lightcurves underline the assumption that CDS dynamics can be conceived as superpositions of various oscillations originating from distinct processes having different time scales, namely the pulsation of the star determining the short hydrodynamics time scale and the process of the dust formation determining the longer time scale.

Finally, the analysis procedure was applied to a parameter set reproducing observations of the individual object IRC +10216. The synthetic lightcurves could reproduce the observed short-term behaviour induced by the stellar pulsation, but predict also a larger underlying period maybe associated with the dust formation time scale. But, this needs to be confirmed by long-term observations.

A possible extension of this work could be with regard to the influence of the gas opacity. In this work it was chosen a constant and small-valued gas opacity in order to stress the interaction between dust and stellar radiation. The assumption of a more realistic, variable gas opacity introduces additional timescales which imply a more complex shell dynamics. Observations clearly indicate that the dust distribution around late type AGB stars derivates from spherical symmetry. Moreover it is generally clumpy. This would require the development of a multi-dimensional program code.

Appendix A

FFT for the case $N = 8$

The easiest way to visualise the FFT procedure is perhaps via the Fourier matrix

$$\mathbf{X} = W_N^{nk} \mathbf{x}. \quad (\text{A.1})$$

This expression can be rewritten in the form of a matrix multiplication:

$$\begin{pmatrix} X_0 \\ X_1 \\ X_2 \\ \vdots \\ X_{N-1} \end{pmatrix} = \begin{pmatrix} 1 & 1 & 1 & \dots & 1 \\ 1 & W_N^{1 \cdot 1} & W_N^{1 \cdot 2} & \dots & W_N^{1 \cdot (N-1)} \\ 1 & W_N^{2 \cdot 1} & W_N^{2 \cdot 2} & \dots & W_N^{2 \cdot (N-1)} \\ \vdots & \vdots & \vdots & \dots & \vdots \\ 1 & W_N^{(N-1) \cdot 1} & W_N^{(N-1) \cdot 2} & \dots & W_N^{(N-1) \cdot (N-1)} \end{pmatrix} \begin{pmatrix} x_0 \\ x_1 \\ x_2 \\ \vdots \\ x_{N-1} \end{pmatrix} \quad (\text{A.2})$$

Direct computation of the DFT is basically inefficient primarily because it does not exploit the periodicity and symmetry properties of the phase factor W_N . In particular, these two properties are:

$$\begin{aligned} \text{Periodicity property :} & \quad W_N^{n+N} = W_N^n \\ \text{Symmetry property :} & \quad W_N^{n+N/2} = -W_N^n \end{aligned} \quad (\text{A.3})$$

$W_N^n = e^{-2\pi in/N}$ is periodic in n and the period is N . This means, it is not strictly necessary to evaluate all powers between $W^{1 \cdot 1}$ and $W^{(N-1) \cdot (N-1)}$ because they will repeat. In order to evaluate a DFT all that is needed is to consider $W_N^1 \dots W_N^{N-1}$.

The Fourier transform matrix in Eq. (A.2) has the following terms:

$$\Lambda^8 = \begin{pmatrix} 1 & 1 & 1 & 1 & 1 & 1 & 1 & 1 \\ 1 & W_8^1 & W_8^2 & W_8^3 & W_8^4 & W_8^5 & W_8^6 & W_8^7 \\ 1 & W_8^2 & W_8^4 & W_8^6 & 1 & W_8^2 & W_8^4 & W_8^6 \\ 1 & W_8^3 & W_8^6 & W_8^1 & W_8^4 & W_8^7 & W_8^2 & W_8^5 \\ 1 & W_8^4 & 1 & W_8^4 & 1 & W_8^4 & 1 & W_8^4 \\ 1 & W_8^5 & W_8^2 & W_8^7 & W_8^4 & W_8^1 & W_8^6 & W_8^3 \\ 1 & W_8^6 & W_8^4 & W_8^2 & 1 & W_8^6 & W_8^4 & W_8^2 \\ 1 & W_8^7 & W_8^6 & W_8^5 & W_8^4 & W_8^3 & W_8^2 & W_8^1 \end{pmatrix} \quad (\text{A.4})$$

Bitreversing

On rearrangement of the columns of the matrix and the entries of the corresponding vector x_k in the following way: $[0, 1, 2, 3, 4, 5, 6, 7] \longrightarrow [0, 2, 4, 6, 1, 3, 5, 7]$, i.e. all the odd columns followed by the even ones, Eq. (A.2) becomes:

$$\begin{pmatrix} {}^8X_0 \\ {}^8X_1 \\ {}^8X_2 \\ {}^8X_3 \\ {}^8X_4 \\ {}^8X_5 \\ {}^8X_6 \\ {}^8X_7 \end{pmatrix} = \begin{pmatrix} 1 & 1 & 1 & 1 & | & 1 & 1 & 1 & 1 \\ 1 & W_8^2 & W_8^4 & W_8^6 & | & W_8^1 & W_8^3 & W_8^5 & W_8^7 \\ 1 & W_8^4 & 1 & W_8^4 & | & W_8^2 & W_8^6 & W_8^2 & W_8^6 \\ 1 & W_8^6 & W_8^4 & W_8^2 & | & W_8^3 & W_8^1 & W_8^7 & W_8^5 \\ \hline 1 & 1 & 1 & 1 & | & W_8^4 & W_8^4 & W_8^4 & W_8^4 \\ 1 & W_8^2 & W_8^4 & W_8^6 & | & W_8^5 & W_8^7 & W_8^1 & W_8^3 \\ 1 & W_8^4 & 1 & W_8^4 & | & W_8^6 & W_8^2 & W_8^6 & W_8^2 \\ 1 & W_8^6 & W_8^4 & W_8^2 & | & W_8^7 & W_8^5 & W_8^3 & W_8^1 \end{pmatrix} \begin{pmatrix} x_0 \\ x_2 \\ x_4 \\ x_6 \\ x_1 \\ x_3 \\ x_5 \\ x_7 \end{pmatrix} \quad (\text{A.5})$$

First Step

Matrix Λ_8 is represented by 4 quadratic submatrices of the order 4×4 .

- First, observe the upper right submatrix:

$$\begin{aligned} (1 \quad 1 \quad 1 \quad 1) &= W_8^0 \cdot (1 \quad 1 \quad 1 \quad 1) \\ (W_8^1 \quad W_8^3 \quad W_8^5 \quad W_8^7) &= W_8^1 \cdot (1 \quad W_8^2 \quad W_8^4 \quad W_8^6) \\ (W_8^2 \quad W_8^6 \quad W_8^2 \quad W_8^6) &= W_8^2 \cdot (1 \quad W_8^4 \quad 1 \quad W_8^4) \\ (W_8^3 \quad W_8^1 \quad W_8^7 \quad W_8^5) &= W_8^3 \cdot (1 \quad W_8^6 \quad W_8^4 \quad W_8^2) \end{aligned} \quad (\text{A.6})$$

and that

$$\Lambda_4 = \begin{pmatrix} 1 & 1 & 1 & 1 \\ 1 & W_8^2 & W_8^4 & W_8^6 \\ 1 & W_8^4 & 1 & W_8^4 \\ 1 & W_8^6 & W_8^4 & W_8^2 \end{pmatrix} = \begin{pmatrix} 1 & 1 & 1 & 1 \\ 1 & W_4^1 & W_4^2 & W_4^3 \\ 1 & W_4^2 & 1 & W_4^2 \\ 1 & W_4^3 & W_4^2 & W_4^1 \end{pmatrix} \quad (\text{A.7})$$

is a matrix for the 4-point discrete Fourier transform. The multiplication in Eq. (A.6) can be expressed as

$$\begin{pmatrix} 1 & 0 & 0 & 0 \\ 0 & W_8^1 & 0 & 0 \\ 0 & 0 & W_8^2 & 0 \\ 0 & 0 & 0 & W_8^3 \end{pmatrix} \cdot \Lambda^4 =: {}^8\text{Diag}_4 \cdot \Lambda^4 \quad (\text{A.8})$$

with ${}^8\text{Diag}_4$ representing a 4×4 which defines 8-point transform.

- Now, observe that the lower right corner of ${}^8\Lambda_{[0:7]}$ is simply $-{}^8\text{Diag}_4 \cdot \Lambda_4$ because

$$\begin{pmatrix} W_8^4 & W_8^4 & W_8^4 & W_8^4 \\ W_8^5 & W_8^7 & W_8^1 & W_8^3 \\ W_8^6 & W_8^2 & W_8^6 & W_8^2 \\ W_8^7 & W_8^5 & W_8^3 & W_8^1 \end{pmatrix} = W_8^4 \underbrace{\begin{pmatrix} 1 & 1 & 1 & 1 \\ W_8^1 & W_8^3 & W_8^5 & W_8^7 \\ W_8^2 & W_8^6 & W_8^2 & W_8^6 \\ W_8^3 & W_8^1 & W_8^7 & W_8^5 \end{pmatrix}}_{= \text{upper right} = {}^8\text{Diag}_4 \cdot \Lambda_4} \quad (\text{A.9})$$

and $W_8^4 = e^{-2\pi i \frac{4}{8}} = e^{-i\pi} = -1$.

- Lastly, the upper left corner and the lower left corner submatrices are identical and are simply matrices for the 4-point discrete Fourier transform Λ_4 .

In summary Eq. (A.5) can be rewritten as follows.

$$\begin{aligned} {}^8X(x_{[0:7]}) &= \begin{pmatrix} \Lambda^4 & {}^8\text{Diag}_4 \cdot \Lambda^4 \\ \Lambda^4 & -{}^8\text{Diag}_4 \cdot \Lambda^4 \end{pmatrix} \begin{pmatrix} x_{[0:7:2]} \\ x_{[1:7:2]} \end{pmatrix} = \\ &= \begin{pmatrix} 1 & {}^8\text{Diag}_4 \\ 1 & -{}^8\text{Diag}_4 \end{pmatrix} \begin{pmatrix} \Lambda^4 \cdot x_{[0:7:2]} \\ \Lambda^4 \cdot x_{[1:7:2]} \end{pmatrix} \end{aligned} \quad (\text{A.10})$$

In this way, the 8-point transform ${}^8X(x)$ is described in a more compact way (where the index $[a : b : c]$ stands for the order of the vector elements, using integers from a through b with a step of c).

However, note that the last vector is the Fourier transform for 4 points i.e. for the even and for the odd numbers. The 8-point transform is attributed to two 4-point transforms. This is nothing other than the Danielson-Lanczos Lemma (see Sect. 3.1.1).

$$\begin{pmatrix} \Lambda^4 \cdot x_{[0:7:2]} \\ \Lambda^4 \cdot x_{[1:7:2]} \end{pmatrix} = \begin{pmatrix} {}^4X(x_{[0:7:2]}) \\ {}^4X(x_{[1:7:2]}) \end{pmatrix} \quad (\text{A.11})$$

Second step

Applying the same reasoning to ${}^4X(x_{[0:7:2]})$ and to ${}^4X(x_{[1:7:2]})$ one can write:

$$\begin{aligned} {}^4X(x_{[0:7:2]}) &= \begin{pmatrix} 1 & {}^4\text{Diag}_2 \\ 1 & -{}^4\text{Diag}_2 \end{pmatrix} = \begin{pmatrix} {}^2X(x_{[0:7:4]}) \\ {}^2X(x_{[2:7:4]}) \end{pmatrix} \\ {}^4X(x_{[1:7:2]}) &= \begin{pmatrix} 1 & {}^4\text{Diag}_2 \\ 1 & -{}^4\text{Diag}_2 \end{pmatrix} = \begin{pmatrix} {}^2X(x_{[1:7:4]}) \\ {}^2X(x_{[3:7:4]}) \end{pmatrix} \end{aligned} \quad (\text{A.12})$$

Third step

A repetition leads to:

$$\begin{aligned} {}^2X(x_{[0:7:4]}) &= \begin{pmatrix} 1 & {}^2\text{Diag}_1 \\ 1 & -{}^2\text{Diag}_1 \end{pmatrix} \begin{pmatrix} {}^1X(x_0) \\ {}^1X(x_4) \end{pmatrix} = \begin{pmatrix} 1 & {}^2\text{Diag}_1 \\ 1 & -{}^2\text{Diag}_1 \end{pmatrix} \begin{pmatrix} x_0 \\ x_4 \end{pmatrix} \\ {}^2X(x_{[2:7:4]}) &= \begin{pmatrix} 1 & {}^2\text{Diag}_1 \\ 1 & -{}^2\text{Diag}_1 \end{pmatrix} \begin{pmatrix} {}^1X(x_2) \\ {}^1X(x_6) \end{pmatrix} = \begin{pmatrix} 1 & {}^2\text{Diag}_1 \\ 1 & -{}^2\text{Diag}_1 \end{pmatrix} \begin{pmatrix} x_2 \\ x_6 \end{pmatrix} \end{aligned} \quad (\text{A.13})$$

$$\begin{aligned} {}^2X(x_{[1:7:4]}) &= \begin{pmatrix} 1 & {}^2\text{Diag}_1 \\ 1 & -{}^2\text{Diag}_1 \end{pmatrix} \begin{pmatrix} {}^1X(x_1) \\ {}^1X(x_5) \end{pmatrix} = \begin{pmatrix} 1 & {}^2\text{Diag}_1 \\ 1 & -{}^2\text{Diag}_1 \end{pmatrix} \begin{pmatrix} x_1 \\ x_5 \end{pmatrix} \\ {}^2X(x_{[3:7:4]}) &= \begin{pmatrix} 1 & {}^2\text{Diag}_1 \\ 1 & -{}^2\text{Diag}_1 \end{pmatrix} \begin{pmatrix} {}^1X(x_3) \\ {}^1X(x_7) \end{pmatrix} = \begin{pmatrix} 1 & {}^2\text{Diag}_1 \\ 1 & -{}^2\text{Diag}_1 \end{pmatrix} \begin{pmatrix} x_3 \\ x_7 \end{pmatrix} \end{aligned}$$

Thereby, the fact that ${}^1X(x_k)$ is a single-point transform was used, i.e. the identity:

$${}^1X(x_k) = W_1^{0 \cdot 0} x_k = x_k \quad (\text{A.14})$$

All in all, one 8-point transform is converted into eight 1-point transforms in 3 steps. During this process, the order of the samples were changed from $[0, 1, 2, 3, 4, 5, 6, 7]$ to $[0, 4, 2, 6, 1, 5, 3, 7]$.

Bibliography

- Alexander D. R., Johnson H. R., Rypma R. L.: 1983, *ApJ* 272, 773
- Allen C. W.: 1973, *Astrophysical Quantities* (London: The Athlone Press)
- Becklin E.E, Frogel J.A., Hyland A.R., Kristian J., Neugebauer G.: 1969, *ApJ* 158, 133
- Bowen G.H.: 1988, *AJ* 329, 299
- Bowen G.H., Willson L.A.: 1991, *ApJ* 375, L53
- Brigham E.O.: 1989, *FFT Schnelle Fourier-Transformation*, R. Oldenbourg Verlag GmbH, München
- Campbell M.F., Gezari D.Y., harvey P.M., Hoffmann W.F., Hudson H.S., Neugebauer G., Soifer B.T., Werner W., Westbrook W.E.: 1976, *ApJ* 208,396
- Cooley J. W., Tukey J.W.: 1965, *Math. Comput.* 19, 297
- Cox J.P.: 1983, *Theory of stellar pulsation*, Princeton University Press
- Crosas M., Menten K.: 1997, *ApJ*, 483, 913
- Dominik C., Gail H.-P., Sedlmayr E., Winters J.M.: 1990, *A&A*, 240, 365
- Dorfi E.A., Höfner S.: 1998, *RvMA* 11, 174
- Dyck H.M., Benson J.A., Howell R.R., Joyce R.R. Leinert C.: 1991, *AJ* 102, 200
- Eddington A.S., Plakidis L.: 1929, *MNRAS*, 90, 65
- Feuchtinger M. U., Dorfi E. A., Höfner S., 1993, *A&A*, 273, 513
- Fleischer A.J., Gauger A., Sedlmayr E.: 1992, *A&A*, 266, 321
- Fleischer A.J.: 1994, *Hydrodynamics and Dust Formation in the Circumstellar Shells of Miras and Long-Period Variables*, PhD thesis

- Fleischer A.J., Gauger A., Sedlmayr E.: 1995, A&A, 297, 543
- Gail H.-P., Keller R., Sedlmayr E.: 1984, A&A 133, 320
- Gail H.-P., Sedlmayr E.: 1987, A&A 177, 186
- Gail H.-P., Sedlmayr E.: 1988, A&A 206, 153
- Gauger A., Gail H.-P., Sedlmayr E.: 1990, A&A 235, 345
- Groenewegen M.A.T., van der Veen W.E.C.J., Matthews H.E.: 1998, A&A 338, 491
- Habing H.J., Tognon J., Tielens A.G.G.M.: 1994, A&A 286, 523
- Helling C., Winters J.M., Sedlmayr E.: 2000, A&A 358, 651
- Höfner S., Feuchtinger M. U., Dorfi E. A.: 1995, A&A 297, 815
- Hoffmeister C., Richter G., and Wenzel W.: 1990, *Veränderliche Sterne*, 3rd ed., Johann Ambrosius Barth, Leipzig
- Holzer, T.E.: 1987, *Theory of winds from cool stars*, in Appenzeller, I. and Jodan C., ed., *Circumstellar matter*, Proceedings of the IAU Symposium, Heidelberg, Reidel Dordrecht Publishing Co., p. 289-305.
- Icke V., Frank A., Heske A., 1992, A&A 258, 341
- Knapp G.R.: 1985, ApJ 293, 273
- Le Bertre T.: 1987, A&A 176, 107
- Le Bertre T.: 1988, A&A 203, 85
- Le Bertre T.: 1992, A&AS 94, 377
- Le Bertre T., Gougeon S., Le Sidaner P.: 1995, A&A 299, 791
- Loup C., Forveille T., Omont A., Paul J. F.: 1993, A&AS 99,291
- Lucy L.B.: 1971, ApJ 163, 95
- Lucy L.B.: 1976, ApJ 205, 482
- Maron M.: 1990, Ap&SS 172, 21
- Meier S.: 2000, *Staubhüllen pulsierender Roter Riesen als dynamische Systeme*, Diplomarbeit

- Menten K.M., Reid M.J., Krügel E., Claussen M.J., Sahai R.: 2006, A&A 453, 301
- Men'shchikov A.B., Balega Y., Blöcker T., Osterbart R., Weigelt G.: 2001, A&A 368, 497
- Olofsson H., Johansson L. E. B.; Hjalmarsen A.; Nguyen-Quang-Rieu: 1982, A&A 107, 128
- Olofsson H., Eriksson K., Gustafsson B., Carlström U.: 1993, ApJS 87, 267
- Osterbart R., Balega Y. Y., Blöcker T., Men'shchikov A. B., Weigelt G.: 2000, A&A, 357, 169
- Ott E.: 2002, *Chaos in Dynamical systems*, 2nd ed., Cambridge University Press
- Percy J.R., Colivas T.: 1999, PASP 111, 94
- Preibisch Th., Ossenkopf V., Yorke H.W., Henning Th.: 1993, A&A 279, 577
- Press W.H., Teukolsy S.A., Vetterling W.T., Flannery B.P.: 1992, *Numerical Recipes in FORTRAN*
- Richtmyer R.D., Morton K.W.: 1967, *Difference Methods for Initial-Value Problems*, 2nd ed., John Wiley & Sons, New York
- Ridgway S.T., Keady J.J.: 1988, ApJ 326, 843
- Sahai R., Claussen M.J., Masson C.R.: 1989, A&A 220, 92
- Sandin C.: 2008, MNRAS 385, 215
- Schirmacher V.: 2003, A&A, 404
- Schirmacher V.: 2007, *The influence of Temperature Fluctuations on Dust Formation in Dust Driven Winds of Asymptotic Giant Branch Stars*, PhD thesis
- Schuster H.G., Just W.: 2005 *Deterministic Chaos*, Wiley-VCH Verlag Weinheim, 4. edition
- Sedlmayr E., Winters J.M.: 1996, *Cool star winds and mass loss: Theory*, IX-th. EADN Summer School on "Stellar atmospheres: Theory and observations", Lecture Notes in Physics, De Greve, J.P., Blomme, R., Hensberge, H. (Eds.), Springer, 1997
- Sopka R.J., Hildebrand R., Jaffe D.T., Gatley I., Roelling T., Werner M., Jura M., Zuckerman B.: 1985, ApJ 294, 242

- Stoer J., Bulirsch R.: 1980 *Introduction to Numerical Analysis*, Springer-Verlag
- Tscharnutter W.M., Winkler K.-H.: 1979, *Comp. Phys. Comm.* 18, 171
- Unno W., Kondo M.: 1976, *PASJ* 28, 347
- Walmsley C.M., Chini R., Kreysa E., Steppe H., Forveille T., Omont A.: 1991, *A&A* 248, 555
- Weigelt G., Balega Y., Bloecker T., Fleischer A. J., Osterbart R., Winters J. M.: 1998, *A&A* 333, 51
- Whitelock P.A., Feast M.W., Catchpole R.M.: 1991, *MNRAS* 248, 276
- Winters J.M.: 2004, *Internal Structure and Optical Appearance of Circumstellar Dust Shells around Cool Carbon Giants*, PhD thesis
- Winters J.M., Fleischer A. J., Sedlmayr E., Gauger A. H.: 1996, *IAUS* 170, 146
- Winters J.M., Fleischer A.J., Le Bertre T., Sedlmayr E.: 1997, *A&A* 326, 305
- Winters J.M., Le Bertre T., Jeong K.S., Helling Ch., Sedlmayr E.: 2000, *A&A* 361, 641
- Witteborn F.C., Strecker D.W., Erickson E.F. Smith S.M., Goebel J.H., Taylor B.J.: 1980, *ApJ* 238, 577
- Woitke P.: 1997, *Radiative Heating and Cooling in Circumstellar Envelopes*, PhD thesis
- Wood P.R.: 1979, *ApJ* 227, 220
- Wood P.R.: 1995, *ASP Conf. Ser.*, Vol. 83
- Wood P.R.: Alcock C., Allsman R.A., et al.: 1999, in *Asymptotic Giant Branch Stars*, ed. T. Le Bertre, A. Lebre, & C. Waelkens, *IAU Symp.*, 191, 151

Danksagung

An dieser Stelle möchte ich mich bei all denen bedanken die mich auf vielfältige Weise bei meiner Arbeit unterstützt haben.

Allen voran gilt mein Dank dem Doktorvater dieser Dissertation, Prof. Sedlmayr der mir die Freiheit bei der Ausgestaltung der Arbeit gab. Frau Prof. Rauer bin ich dankbar für die Erstellung des Zweitgutachtens und für die Übernahme des Prüfungsvorsitzes danke ich Herrn Prof. Brandes. Herrn Prof. Kegel danke ich für seine stete Diskussionsbereitschaft.

Mein besonderer Dank gilt Dr. Michael Hegmann der in intensiven Diskussionen und Disputen Anregungen gab und somit wesentlich zum Gelingen dieser Arbeit beigetragen hat. Ein großes Dankeschön auch an Dr. Beate Patzer für ihre Ratschläge und Motivation über all die Jahre. Ihr und Dr. Lee Grenfell danke ich insbesondere für das Korrekturlesen dieser Arbeit. Dr. Ewert gilt mein Dank für das Erleben einer praktische Anwendung der Fourier Analyse.

Bedanken möchte ich mich bei Uwe Bolick, der mir unzählige Tipps und Antworten rund um Rechner und Software Problemen gab. Nicht nur für ihre sportliche Unterstützung danke ich Mareike Godolt.

Nicht versäumen möchte ich, mich bei allen derzeitigen und ehemaligen Mitgliedern des Zentrums für Astronomie und Astrophysik zu bedanken. Dies sind insbesondere Jan Bolte, Daniel Kitzmann, Karen Lingnau, Sime Pervan, Vasco Schirmacher, Astrid Wachter und Matthias Wendt. Danke für eine kollegiale Atmosphäre.

Ganz besonders danke ich Anne und Hans für ihr Verständnis und Rückhalt während dieser Jahre. Ich bedanke mich bei André Reimann der meiner Arbeit viel Verständnis und Geduld entgegenbrachte. Zum Schluß möchte ich mich bei meinen Eltern und all meinen Freunde bedanken ohne deren Unterstützung das gesamte Studium nicht möglich gewesen wäre.